

Investigation of tropospheric arctic aerosol and mixed-phase clouds using airborne lidar technique

Dissertation

zur Erlangung des akademischen Grades
Doktor der Naturwissenschaften (Dr. rer. nat.)
in der Wissenschaftsdisziplin Physik der Atmosphäre

eingereicht an der
Mathematisch-Naturwissenschaftlichen Fakultät
der Universität Potsdam

von
Iwona Sylwia Stachlewska

Stiftung Alfred-Wegener-Institut für Polar- und Meeresforschung
Forschungsstelle Potsdam, Telegrafenberg 43A, 14473 Potsdam

Potsdam, November 2005

I dedicate this piece of work to my beloved parents and siblings...

My mother, Teresa, who taught me to fence through my life, win, lose but never give up. My father, Henryk, who taught me a hard brave work as a way to exceed limits of impossible. My sisters, Ola, Gosia and Agata, and brothers, Piotr, Michał and Arek, who taught me that self-realisation comes through sharing and giving.

Contents

1	Introduction	3
1.1	Importance of aerosols and clouds	3
1.2	Aerosols and clouds in the Arctic	5
1.3	Measurement techniques of aerosols and clouds	7
1.3.1	Lidar as a vital tool for atmospheric studies	8
1.3.2	Optical and microphysical parameter retrieval from lidar signals	8
2	Arctic field campaigns	10
2.1	Scientific activities during ASTAR 2004	11
2.1.1	Airborne activities	12
2.1.2	Ground based, satellite and modelling activities	15
2.2	Scientific activities during SVALEX 2005	19
3	AWI lidars for measurements during Arctic field campaigns	20
3.1	The stationary Koldewey Aerosol Raman Lidar KARL	20
3.2	The new Airborne Mobile Aerosol Lidar AMALi	20
3.2.1	Optical assembly	21
3.2.2	Transmitting system	22
3.2.3	Receiving and detecting system	23
3.2.4	Data acquisition system	24
3.2.5	AMALi end-products and their applications	25
4	Data evaluation schemes and error sources discussion	27
4.1	Backscatter lidar techniques	28
4.2	Backscatter lidar equation	29
4.3	Diverse approaches for the elastic backscatter lidar retrieval	30
4.3.1	Solution for an aerosol rich homogeneous atmosphere (slope method approach)	30
4.3.2	Solution for aerosol rich heterogenous atmosphere (Klett approach)	31
4.3.3	Solution for a heterogenous atmosphere with aerosol rich and aerosol free layers (Klett-Fernald approach)	31
4.4	Ansmann approach for inelastic backscatter lidar retrieval	33
4.5	Two-stream approach for elastic backscatter lidar retrieval and estimation of lidar instrumental constants	34
4.5.1	Retrieval of extinction, backscatter and lidar ratio profiles	34
4.5.2	Estimation of lidar instrumental constants	36
4.6	Iterative Klett approach for airborne elastic backscatter lidar retrieval	37
4.7	Direct retrieval of aerosol microphysical parameters	38
5	Lidar data analysis and applications	39
5.1	Meteorological situation during the ASTAR 2004 and SVALEX 2005 campaigns	39
5.1.1	MODIS imagery	39
5.1.2	ECMWF operational analysis	40
5.1.3	Radiosonde observations	42
5.1.4	NOAA HYSPLIT trajectories	43
5.1.5	FLEXPART long-range pollution transport	44
5.1.6	ECMWF operational analysis for 19 May 2004	48
5.1.7	The mixed-phase cloud study of ASTAR 2004	50

5.2	Intercomparison of AMALi and KARL lidars operated in the zenith-aiming ground based configuration	50
5.3	Variability of the particle extinction coefficient over the Kongsfjord obtained from the horizontally-aiming ground based AMALi measurements	52
5.4	The two-stream inversion of the airborne nadir-aiming AMALi and zenith-aiming ground based KARL data	53
5.4.1	Estimation of the AMALi and KARL instrumental constants	53
5.4.2	Calculation constrains and errors of the two-stream AMALi and KARL retrievals	54
5.4.3	Comparison of the two-stream AMALi and KARL retrieval to the Raman KARL retrieval	55
5.5	The iterative Klett backward algorithm for inversion of the nadir-aiming airborne AMALi lidar data	56
5.5.1	The discussion of the uncertainties of the iterative airborne inversion	57
5.5.2	The application of the iterative airborne inversion for the calibrated 'along-flight' backscatter coefficient calculation	57
5.6	Clean and polluted Arctic air and their characteristic properties	60
5.6.1	General situation during ASTAR 2004 and SVALEX 2005	60
5.6.2	Background aerosol load at ASTAR campaign	62
5.6.3	Increased aerosol load at SVALEX campaign	63
5.7	Estimation of the temporal progress of the Arctic Haze event during SVALEX campaign	65
5.8	Investigation of the occurence of the humid layers over Ny-Ålesund	68
5.9	Aerosol variability in the Foehn-like gap area during ASTAR campaign	70
5.9.1	The categorisation of the lidar backscatter ratio profiles	70
5.9.2	Comparison of the lidar backscatter profiles with output of a local scale dispersion model EULAG	72
5.10	Observations of mixed-phase clouds with alternated AMALi and in-situ instrumentation	74
5.10.1	New aerosol-cloud investigations aspects during ASTAR 2004	75
5.10.2	The in-situ instrumentation	75
5.10.3	The observations of could system in Storfjorden	76
5.10.4	The remote sampling with AMALi	77
5.10.5	The in-situ sampling with cloud microphysics instrumentation	79
5.10.6	The comparison of the remote and in-situ particle backscatter and extinction retrievals	81
6	Conclusions and Outlook	83
6.1	Comments on the aerosol and clouds studies described in the frame of this work	83
6.2	Recommendations for further research	88
7	Acknowledgements	89

1 Introduction

1.1 Importance of aerosols and clouds

Aerosols

Any non-molecular atmospheric constituent floating in the atmosphere, i.e. dust, water droplets, ice crystals, smoke and related to the immission and emission small particles released into the atmosphere are defined as aerosol (Friedlander [1], Seinfeld [2]). For the minimum stability of the atmosphere of one hour the size of the aerosol particles is limited roughly to $10^{-3} - 10^2 \mu$. Particles below that size are defined as clusters or small ions, and beyond as coarse dust and precipitation elements (rain, snow, hail).

The aerosol particles are generated through physical, chemical and biological processes in the atmosphere with three different source types: the Bulk-to-Particle-Conversion BPC (liquid or solid material division into particles - mineral dust, sea salt, plant debris, pollen), the Gas-to-Particle-Conversion GPC (condensable vapours leading to a new particle nucleation or condensation growth of existing particles), and the combination of these types by the high temperature combustion processes (soot, supersaturated vapours).

The physical and chemical characteristics of aerosols with respect to their number concentrations depend on the aerosol type and varies from $10^5 - 10^6 \text{ cm}^{-3}$ for urban, $10^3 - 10^4 \text{ cm}^{-3}$ non-urban continental, $10^2 - 5 \cdot 10^2 \text{ cm}^{-3}$ remote marine, $10^2 - 10^4 \text{ cm}^{-3}$ Arctic winter, and $10^0 - 10^3 \text{ cm}^{-3}$ Arctic summer aerosol.

The multimodal size distribution of aerosols depend on the existence of the small Aitken particles of the nucleation mode of $0.001 - 0.1 \mu$ diameter (nucleation and condensation from gaseous phase fast depleted by Brownian diffusion), the accumulation mode particles of $0.1 - 1 \mu$ (removal-resistant congregation due to inefficiency of atmospheric cleansing processes) and the coarse mode particles of a size larger than 1μ (largest particles fast depleted preferentially by initial impaction on obstacles or gravitational sedimentation).

The shape and the chemical composition of aerosol types is strongly dependent on the particle sources, the physical processes (coagulation, hygroscopic growth, supersaturation) and the chemical transformations (oxidation of trace gases, surface/particle material, dissolved gases and particulate matter).

Main particle sink processes are due to dry deposition (gravitational sedimentation, Brownian thermal diffusion), wet deposition (in-cloud scavenging due to nucleation, Brownian diffusion and coalescence or sub-cloud scavenging due to Brownian diffusion and coalescence), and cloud deposition (interception of cloud/fog droplets with surface structure).

The aerosol global vertical and horizontal distribution is very inhomogeneous and strongly dependent on meteorological conditions and orography. The horizontal distribution in the lower troposphere reflects, mainly due to the relatively short aerosol lifetimes from few days to a week, the geographical locations of sources and sink processes. The vertical distribution is characterised by strong variations in the first 2-3 kilometers in the lower troposphere. Above, homogenous distribution with a gradual decrease in concentration towards the tropopause of aloft of BPC-sources and rather constant concentrations of GPC-sources in upper troposphere can be expected.

Clouds

The cloudy atmosphere constitutes a multicomplex multiphase atmospheric system, as gaseous species, atmospheric particulate and liquid droplets coexist at one time.

The spatial and temporal scale involved in clouds multiphase physical processes leading to the mass exchange between different phases (emission, dry/wet decomposition, gas-to-particle conversion, nucleation, condensation, evaporation, dissolution, aerosol capture by falling droplets, precipitation formation) varies from molecular processes (few Ångström / microsecond) to synoptic meteorology (tousands of kilometers / days).

Clouds form mainly by homogenous nucleation (condensation of liquid droplets from water vapour molecules at the supersaturation levels over 100 %), by heterogenous nucleation (condensation of water vapour onto atmospheric aerosol particles - Clouds Nucleation Centres CCN, at the supersaturation levels attained in the atmosphere of less than 1 %), and by convective uplift of moist air accompanied by adiabatic expansion and cooling.

The chemical composition of clouds depends on the gaseous species and aerosols incorporated into cloud droplets by the mentioned nucleation scavenging (most efficient), by other aerosol particle scavenging mechanisms (attachment to clouds droplets by Brownian motion, phoretic effects, collisional capture), by the scavenging of the gaseous species in cloud droplets, by the dissolution of the trace gases in cloud water (mainly oxidation reactions of sulfur compounds in water cloud by H_2O_2 , O_2 , O_3 and nitrogen by OH), and by the gas phase reactions between interstitial air and the droplets.

All these physical processes and chemical transformations might occur independently or simultaneously (Liou [3], Young [4]).

Additionally, at the temperatures below the freezing point of water supercooled droplets occur, as at $-10^\circ C$ ($\approx 200\text{ cm}^{-3}$) only one droplet in a million is normally frozen. However, the ice particles are initially generated by freezing of these supercooled droplets or by condensation of water vapour on the nuclei directly from the gas phase (less efficient). The probability of the generation of the ice particles within clouds increases with the further decrease of their temperature, so that at $-40^\circ C$ the clouds consists practically entirely of ice particles. The mixed-phase clouds consisting of both ice particles and supercooled droplets are highly unstable due to the air slightly undersaturated with respect to water and the air slightly oversaturated with respect to ice. This results in an ice crystal grow by sublimation at the expense of the liquid phase.

For the warm liquid-phase precipitation the condensation process alone is too slow (the growth rate of cloud droplet by molecular diffusion of water vapour is inversly proportional to the size of the water droplet) to enable production of large enough droplets which could eventually precipitate. However, the collisions and coalescence of particles (usually grown on the largest CCN's) produce largest droplets with a settling velocity counterbalancing the uprising motion within the cloud, what makes them fall and, by coliding with smaller droplets on their path, form the rain droplets.

The cold ice-phase cloud precipitation (Wegener-Bergeron-Findeisen process) starts with the ice particle growth by water deposition, then an increase of the particle size increases riming (collisions with supercooled droplets which freeze onto them) and aggregation (collisions of ice particles with each other) until the particles start to fall through the cloud, where further growth results only from collisions. The falling ice particles produce a solid precipitation of the hail and snow or a precipitation of the rain droplets (fall through warm layers were ice crystals can melt).

Finally, the water with its gaseous and particulate trace compounds are removed from the atmosphere due to the precipitation by in-cloud scavenging of gas and particles and their deposition in precipitation elements or by below-cloud scavenging occuring by the incorporation of gases and aerosol particles in the volumne of the air swept by falling precipitation elements.

Aerosols and clouds effects on climate - modelling aspects

Since in the atmosphere both aerosol and clouds particles can scatter and absorb the long and short range radiation, and emit the long range radiation, it is well recognised, that they can have great influence on weather and climate (Hobbs [5], Kondratyev [6]).

Clouds have a major influence on the entire atmosphere by their effect on the hydrological cylce by scattering of incoming solar radiation (albedo effect) and absorbing outgoing infrared radiation (greenhouse effect), as well as by their effect on the atmospheric photochemistry (alterations of actinic flux relative to cloudless conditions).

Aerosols affect climate *directly* through sunlight attenuation, as they reflect it back into space, thus reducing the amount of energy reaching the surface, and through absorbing sunlight and infrared radiation, increasing local heating and effecting the way heat is radiated back into space, or/and *indirectly*, through influence on the cloud formation processes, as they act as condensation nuclei that form clouds and change their properties effecting clouds particulate morphology, diameter, size distribution and scattering characteristics, and through affecting precipitation efficiency of liquid-, ice- and mixed-phase clouds, as for example large concentrations of small droplets in aerosol contaminated warm clouds tend to make them more reflective, inhibit rainfall and prolong cloud lifetimes.

Already ten years ago, the Intergovernmental Panel on Climate Change II (IPCC 1995 [7]) identified the direct and indirect effects of tropospheric aerosols as a key uncertainties for the prediction of the future global climate, mainly due to not very well known extent of aerosols influence and relative contribution of manmade aerosols as compared to naturally occurring aerosols, as well as aerosol-cloud interaction processes.

In fact, the quantification of aerosol radiative forcing is complex enough, due to the relatively short atmospheric aerosol lifetime resulting in a high spatial and temporal variability of aerosol mass and particle number concentration. Even more, the quantification of aerosols indirect radiative forcing, as in addition also complicated aerosol influences on cloud processes (dependent on cloud-phase) must be accurately modelled. The lower troposphere with highly dynamic aerosol-cloud interaction processes results in a strong variability of the atmospheric states and makes the modelling of their radiative effects even more difficult. Hence, often simplifying (or not even including) of the aerosols and/or clouds parametrisation in climate models is foretaken, though an existence of a gap between observed global temperature changes and what models predict when aerosols are not included are known.

The Intergovernmental Panel on Climate Change III (IPCC 2001 [8]) reported on a considerable progress in understanding the effects of aerosols on radiative balances in the atmosphere, due to, mainly, an increase of a variety of aerosol/cloud related field studies at different locations all over the globe, a variety of aerosol networks and satellite observations over large regions or globally, an improved instrumentation for the chemical composition measurements, and an improvement of the models interpolating and extrapolating the available data on aerosol/clouds properties onto a regional and global scale.

At the same time IPCC 2001 stressed an urgent need for well resolved, both spatially and temporally and in all areas of the globe, information on the microphysical and optical properties of aerosols and clouds, whereby the most important are: the size distribution of particles with respect to shape and content (scattering function, asymmetry factor, and ice/water content in clouds), the size change with relative humidity, the complex refractive index, the particle solubility, the type of aerosols (natural/anthropogenic), and the mixing ratio of different types of particles.

1.2 Aerosols and clouds in the Arctic

Arctic contribution to climate change

The IPCC 2001 estimates for the future climate show further and largest warming over the Arctic. The Arctic Climate Impact Assessment (ACIA 2004 [9]) highlighted the observed climate warming trends: increase of annual temperatures of 1-3°C in the last 50 years, increased river discharge and earlier occurrence of spring peak of river flows, reduced salinity and density of North Atlantic Ocean, 10% decline of snow cover over the past 30 years, precipitation increase of 8% on average over the past century with more rain in autumn and winter, thawing permafrost in recent decades, later freeze-up and earlier break-up of ice covering lakes and rivers, reduced of 1-3 weeks ice season in North America and

western Eurasia, melting of Alaskan glaciers and Greenland ice sheet, retreat by 15-20% of sea-ice cover over last 30 years, and a sea level rise of 10-20 cm during the past century.

Overall, ACIA 2004 defined three major mechanisms by which the Arctic can contribute to additional Earth's climate change: alternations in surface reflectivity, changes of ocean circulation patterns and increase of greenhouse gas emissions. Although few times mentioned, there was no attempt to assess on the poorly understood aerosol effects on Arctic climate.

Generally, the role of the direct and indirect aerosol effects in the Arctic and Antarctic is often underestimated or even neglected, due to an assumption that they do not significantly influence the climate on a global scale, because of the low solar elevation at high latitudes and the fact that the polar regions represent a small part of the Earth's surface. However, significant regional radiative effects may occur as the polar regions represent a sensitive ecosystems, highly susceptible to even small changes in the local climate. Also the Arctic conditions of, usually, high surface albedo (snow/ice) and low solar elevations significantly alter interaction between solar radiation and aerosol/clouds with respect to the lower latitudes, for a given aerosol distribution, the specific optical properties may be enhanced in the polar regions.

Also studies of climate change due to clouds in climatically pivotal Arctic area to assess whether and how they do affect the global climate are necessary. Such studies require investigations on the cloud areal coverage, the changes of cloud radiative properties with altitude, the changes in area, type and phase of cloud, the indirect effect of aerosols on cloud formation and the influence of the clouds on the ice pack modification.

Climate impact of Arctic aerosol - Arctic Haze

The Arctic aerosol radiative properties and aerosol-cloud interactions with respect to natural and anthropogenic aerosol sources have been focused mainly on the Arctic Haze phenomenon (Barrie [10], Heintzenberg [11], Shaw [12]).

During the transition from winter and early spring season into summer the atmospheric transport pattern changes (i.e. the arctic front expanded strongly over a large fraction of Northern Hemisphere in winter weakens and moves towards polar latitudes) causing variations in the flux of trace gases and particles into the Arctic reservoirs. In summer the Arctic is practically free of anthropogenic aerosol since the atmospheric circulation patterns protect the high latitudes from long-range transport of air masses and, hence, magnitude of aerosol loads represent the natural background conditions typical for sea salt and biological aerosol.

The strong intrusions of polluted air masses from lower latitudes during Arctic Haze events occur mostly during late winter and spring. The haze aerosols are transported at different levels in the troposphere to the high Arctic latitudes from industrial areas in Europe, Siberia and North America. Due to the stable atmospheric conditions, low cloud cover and low precipitation during late winter and early spring in the Arctic this aerosol can be trapped in the troposphere even for a month, while during the summertime the strongest build up due to the highest pollution removal-rate occurs (Bodhaine and Dutton [13]).

The Arctic Haze particles can be characterised as a submicron size (power-law relationship with exponent about 1.5), well-aged (dominating strong, well-defined accumulation mode of removal-resistant aerosols with the absence of the smallest and largest particles), with substantial fraction due to sulfate (cooling effect) and soot (locally warming effect) (Jaeschke et al. [14], Charlson and Wigley [15]).

The strong interaction of Arctic Haze pollution with the sunlight (similar size of haze particles and wavelength of major radiant energy around 500 nm), as well as the strong absorption of the Sun's shortwave radiation by the soot particles enhances the potential of haze to alter the radiation budget by cooling or warming of the atmosphere depending

on the altitude of such aerosol intrusions (Penner et al. [16]).

Additionally, the existence of the Arctic Haze particles in the atmosphere can influence the nucleation processes (Aalto et al. [17]) and the mixed-phase clouds properties and even the precipitation.

Difficulties of characterisation of the Arctic aerosols and clouds

The characteristic for the Arctic atmospheric dynamics almost laboratory-like polluted-to-clean aerosol transition during Springtime makes it particularly interesting and useful for the aerosol and cloud investigations and modelling of themselves or their interaction. However, difficulties occur due to extremely scant, restricted to the boundary layer at a few locations, information on the Arctic aerosols and clouds properties needed for their characterisation.

The full assessment can be accomplished only by collaborative studies on Arctic aerosol-cloud-climate interactions by combining the experimental data on aerosols/clouds properties obtained from the local stations, field campaigns, satellite measurements (Treffeisen et al. [18], Yamanouchi et al. [19]) applied together with a sophisticated, especially designed for the Arctic purpose models (Dethloff et al. [20], Rinke et al. [21]), with improved for the polar conditions parametrisation of both aerosols and clouds processes (temperature, humidity).

1.3 Measurement techniques of aerosols and clouds

The actual, both in time and space, highly variable properties of clouds and aerosol particles, i.e. the number density (the amount of particles per volume), the microphysical properties (size distribution, refractive index and shape) and the height distribution are difficult to measure directly but they can be principally derived from aerosol optical properties measurements. Additionally, creation, advection and distribution of aerosols/pollutants are highly dynamic and conventional monitoring methods, even if performed at all stations in the Arctic, are not able to satisfy the needs providing rather sparse data on the spatial and temporal aerosol distribution.

In-situ measurements as point monitors at the ground level give only locally representative information on the aerosol and yield no information about the vertical distribution of aerosols such as differences between the boundary layer and the free troposphere. The airborne in-situ measurements cannot sample all interesting layers simultaneously. Balloon-borne sensors give a vertical profile but provide only poor temporal and spatial resolution of the measurements.

Remote sensing instrumentation can be used for obtaining measurements in hazardous or difficult to reach regions without disturbing the measured atmospheric states and, thus provide a fast and inexpensive probing of large volumes and hence a large volume averages robust to local fluctuations (Jensen [22]).

However, the passive remote sensing data obtained using Sun or Star photometers for the aerosols optical depth measurements does not provide the vertical resolution either and additionally makes the measurements strongly dependent on natural light sources and time of day. Also satellite passive remote sensors have poor vertical resolution and though covering most parts of the Earth they are often of high uncertainty over land (where the main aerosol sources are) and over poles (due to albedo problems).

In both cases cloud cover can prevent aerosol observations resulting in a strong good weather bias for the photometer measurements performed for cloud-free atmosphere only and high uncertainty of satellite measurements due to the clouds interpolation for the daily, weekly averages. Additionally, the Arctic applications of satellite retrievals for the aerosol optical thickness require the improvement of present algorithms (von Hoyningen-Huene et al. [23]) for high latitudes and low sun elevations.

The combination of satellite, balloon-borne and ground based in-situ and remote passive observations allows, to some degree, a determination of the spatial extension of the aerosol states. However, to complement these observations vertically resolved aerosol data are needed. Therefore, the applications of one of the active remote sensing techniques for the studies of the atmospheric properties, namely the use of the lidar technique (Collis [24]) to measure aerosols concentration in different parts of the atmosphere is widely used (Bösenberg and Matthias et al. [25]). The remote vertically and horizontally resolved lidar data can successfully complement other ground based or airborne in-situ measurements and validate remote satellite based observations and remote active and passive ground based observations.

1.3.1 Lidar as a vital tool for atmospheric studies

The active laser remote sensing, independent of natural light sources and time of day, allows to measure atmospheric contaminations spatially resolved over distances and altitudes of several kilometres.

The lidar (an acronym from LIght Detection and Ranging) uses the same principle as radar but it is based on scattering phenomenon of light (Measures [26]). Change of the first two letters in the name of radar results in the shift from the radio waves to the visible region waves, decreasing by many orders of magnitude the wavelength of electromagnetic radiation and, at the same time, increasing by the same rate the resolution of the system enabling detection of objects as small as molecules of gaseous species present in the atmosphere. Use of a pulsed laser as a light source enables an increase in both the sensitivity, due to the high energy of emitted pulses, and spatial resolution, due to very short time of their duration, so that the measurements of very low aerosol concentrations and the determination of a range from the lidar instrument to a target aerosol in different parts of the atmosphere are possible. The time for the light to travel out to the target and back to the lidar is thereby used to determine the range to the target.

Hence, the lidars can provide high resolution information on existence, reflectance, range, direction, and depolarisation of the target aerosols in the atmosphere in form of a line integral, average and profile data, as well as 2/3-dim coverage and spectrum data all as a function of time. High quality aerosol lidar data are characterised by reduced sensitivity to background light, high intensity (high signal-to-noise ratio), control, knowledge and small dynamic range of the stimulating target atmosphere signal. Improvement of the quality and reliability of the systems can be characterised by many parameters, like sensitivity, resolution, range and dimensions.

Lidars, installed on the ground, ship, car, aircraft or even satellite platforms, are used for tracking variety of aerosol particles as well as to investigate and map industrial smoke, dust, rain and clouds, trace gases and are applied also for temperature, wind, and turbulence measurements.

The most common and the simplest backscattering lidar system uses a non-tunable laser, considerably simplifying its construction and operation, a telescope mirror, and a detector. The lidar signal is due to extinction of the lidar beam in the atmosphere and the Lorentz-Mie (mainly) scattering on particles, such as aerosols and dust. Relatively high cross-section value for this type of scattering allows easy signal detection and makes the simple backscattering lidars very valuable tools for aerosol distribution observations.

1.3.2 Optical and microphysical parameter retrieval from lidar signals

The aerosol microphysical parameters (particle index of refraction and size distribution), can be obtained, by solving a mathematically ill-posed inversion problem (Böckmann [27]),

from the optical parameters (extinction and backscatter coefficients) derived from lidar measurements.

Any simple elastic backscatter lidar signal gives a qualitative impression about the vertical distribution of aerosol in the atmosphere but independent retrieval of both optical parameters from the recorded signals is not possible.

The standard calculations (Klett [28] and Klett [29]) depend on two guessed values; the calibration reference value and the ratio of particle extinction and backscatter coefficients (lidar ratio). The guess of the latter one, usually a not well known property of the atmosphere varying greatly with aerosol size and its chemical composition, is especially problematic.

Hence, the additional independent information on the extinction coefficient has to be provided to improve the calculations, usually, done by inclusion of an inelastic Raman-shifted detection line in the lidar system (Ansmann et al. [30]). The two-stream inversion approach, requiring usage of two elastic backscatter lidars aiming into opposite directions provides it either (Kunz [31], Hughes and Paulson [32], Stachlewska et al. [33]). This method seems suitable also for the spaceborne lidar data evaluation and validation (Cuesta and Flamant [34]).

The determination, of lidar instrumental constant in case when one of the lidars observes an aerosol poor layer (Stachlewska and Ritter [35]) opens new aspects for lidar data evaluation, as it allows the microphysical parameters inversion by direct implementation of the lidar signals without necessity of extinction and backscatter retrieval.

The airborne nadir aiming lidar evaluation schemes suffer from difficulty to provide the calibration value during the flight, as the wind-generated aerosol particles near-sea/land surface are usually highly variable. The calibration of retrieved results can be done only if calibration instrumentation is available onboard. With known lidar constant the airborne retrieval at any point of flight duration is possible by using pure lidar signals only (Stachlewska et al. [36])

Estimation of atmospheric aerosols and mixed-phase clouds effects on climate using lidar technique alone does not help. The models need an information on many parameters, some not provided by lidar measurements at all, as for example the absorption coefficient. Hence, only combining comprehensive in-situ and remote, ground based, airborne and satellite observations can extend the output of the experiments to a required accuracy by the regional model large temporal and spatial scale (Fortmann [37], Rinke et al. [21], Treffeisen et al. [38]).

2 Arctic field campaigns

To reduce the uncertainties for the prediction of the future global climate a considerable progress in understanding the direct and indirect effects of aerosols and clouds on radiative balances in the atmosphere has been made due to a variety of international field campaigns, providing a process-level understanding and a descriptive understanding of the aerosols and clouds of various types at different conditions and regions.

During the Aerosol Characteristic Experiments the remote oceanic conditions (ACE 1) Bates et.al [39], the intermittently polluted marine environments (ACE 2) Raes et al. [40], the continental conditions over Lindenberg Aerosol Characteristic Experiment (LACE) Ansmann et al. [41], and the highly polluted conditions during the Indian Ocean Experiment (INDOEX) Ramanathan et al. [42] were investigated. The tropospheric aerosol properties characteristic was obtained during the Interhemispheric Differences in Cirrus Properties from Anthropogenic Emissions campaign (INCA) Minikin et al. [43]. During the same campaign the cirrus clouds properties and aerosol-cirrus interaction were studied Gayet et al. [44], Immler and Schrems [45], Kärcher and Ström [46], Seifert et al. [47]. The tropical cirrus clouds were investigated during the Cirrus Regional Study of Tropical Anvils and Cirrus Layers - Florida Area Cirrus Experiment (CRYSTAL-FACE) McGill et al. [48] The microphysical and radiative properties of stratocumulus clouds were investigated during the European Cloud and Radiation Experiment (EUCREX 1989-1996) Raschke et al. [49], Pawlowska et al. [50] and during the ACE 2 Cloudy Column closure experiment Brenguier et al. [51], Menon et al. [52]. The mixed-phase tropospheric clouds in western part of north Pacific region during the Japanese Cloud and Climate Study (JACCS 1991-1999) Hayasaka et al. [53], Gayet et al. [54], Asano et al. [55].

Lately, it is recognised that there may be significant regional radiative effects of aerosols and clouds in the polar regions, due to their great susceptibility to even small changes in the local, regional and global climate (ACIA 2004 [9]). Hence, the results from field experiments carried out at low latitudes are difficult to transfer to polar regions and there is an urgent need to conduct specific measurement programs in the polar regions.

The studies of the Arctic aerosol radiative properties and aerosol-cloud interactions with respect to natural and anthropogenic aerosol sources focused mainly on the optical properties of the Arctic Haze phenomenon studied within projects such as the Arctic Gas Aerosol Sampling Program (AGASP) Schnell [56] and the Arctic Study of Tropospheric Aerosols (ASTAR 2000) (Yamanouchi [19], Treffeisen et al. [18] and Treffeisen et al. [38]), The International Arctic Ocean Expedition (IAOE) using the Swedish icebreaker *ODIN* (Leck et al. [57]) and the few of the Arctic Experiments (AREX) using the Polish research ship *OCEANIA* (Zieliński and Patelski [58]) provided detailed information on the boundary layer aerosols in the central European Arctic during summer. The Arctic Airborne Measurement Program (AAMP) focused on the spatial distribution of trace gases and aerosols related to stratospheric-tropospheric exchange and the polar vortex (Yamanouchi [59]).

The investigations of the Arctic clouds and their effect on the Arctic climate by providing the characterisation of the microphysics of mixed-phase, pure liquid and ice crystals clouds was in the focus of the Mixed-Phase Arctic Cloud Experiment (M-PACE) Verlinde [60], Aramov et al. [61], Yannuzzi [62]. The same issues together with an additional focus on study of the aerosol-cloud interactions and their influence on the cloud-radiation interaction were one of the goals of the Arctic Study of Tropospheric Aerosols Clouds and Radiation campaign (ASTAR 2004).

However, only few of these experiments had the capability to provide a set of observations of aerosol and clouds radiative properties needed to assess the present and the future impact on the Arctic climate by changes in aerosol and clouds properties.

2.1 Scientific activities during ASTAR 2004

The main focus of the international Arctic Study of Tropospheric Aerosols, Clouds and Radiation (ASTAR, see <http://www.awi-potsdam.de/www-pot/astar/>) projects is the assessment of the direct and indirect impact of Arctic aerosol on climate by providing an observational over-determined data set of physical, chemical and optical properties of tropospheric aerosol and the cloud microphysical properties necessary to improve the assessment of the aerosol effects on the Arctic radiative balance by utilizing unique aircraft instrumental payloads, addressing both aerosol and cloud measurements, combined with ground based and satellite observations and by using appropriate modeling tools. Such coordinated research activities in polar regions are essential to extend the experimental observations to a larger temporal and spatial scale and thereby to provide data sets of variable necessary for the employment in the regional atmospheric climate modeling.

The ASTAR projects were initialised by the Alfred Wegener Institute for Polar and Marine Research (AWI, Bremerhaven, Germany) together with the National Institute of Polar Research (NIPR, Tokyo, Japan). The research aircrafts Polar 2 and Polar 4 were provided by AWI, the flight hours were covered from AWI and NIPR resources and funding provided by national agencies covered costs associated with ground based and satellite measurements and model activities. The ASTAR airborne missions conducted from aircraft base in Longyearbyen on Svalbard (c.fig. 1) were set for three time periods; March/April 2000, May/June 2004, and April 2005 (postponed to 2007).

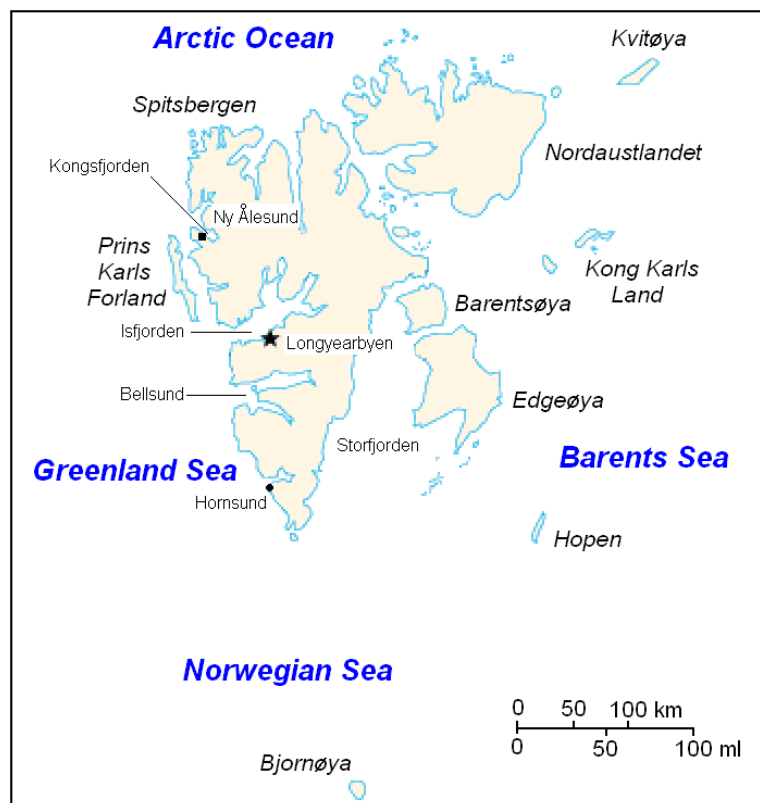


Figure 1: *The Svalbard Archipelago map. The AWI airborne Arctic missions are usually conducted from the Longyearbyen airport. The ground based measurements are taken at Ny-Ålesund and Hornsund.*

The ASTAR 2000 campaign

The main goals of the ASTAR 2000 were the airborne measurements of the aerosol parameters of climate relevance (extinction coefficient, absorption coefficients, and scattering phase function) and creation of the Arctic Aerosol Data Set (AADS) for future application for climate impact studies by using the AWI regional climate model HIRHAM (Dethloff et al. [20]), as well as the comparison of these results with the ground based Raman lidar and the SAGE II satellite instrumentation (Treffeisen et al. [63]). The Polar 4 aircraft measurements were performed from Longyearbyen, while the simultaneous ground based measurements in Ny-Ålesund.

During the campaign new systems were used, like the ground based Raman lidar (Schumacher [64]), the star photometer (Herber et al. [65]), the tethered balloon, and an onboard absorption photometer. For the Arctic spring, 18 extinction profiles covering background and various Arctic Haze conditions were collected with the Polar 4 and 12 extinction profiles were obtained close to Ny-Ålesund with additional ground based measurements. Based on these measurements the tropospheric Arctic aerosols and their climate impact was analysed with the HIRHAM model (Rinke et al. [21]).

The ASTAR 2004 and 2005 campaigns

For both ASTAR 2004 and 2005 campaigns, 160-200 flight hours were allocated to be shared by both involved aircrafts Polar 2 and Polar 4. However, due to an accident of the Polar 4 aircraft during hard landing at the British Rothera Base at the Antarctic Peninsula in January 2005, the last campaign was postponed until April 2007.

During both missions three major issues are approached. Firstly, in May/June 2004 typical clean Arctic summer conditions with characteristic sea salt and mineral aerosol loads protected from long range transport of polluted air. Secondly, in April 2007 typical Arctic Haze event of strong intrusion of an anthropogenic origin polluted air mass from lower latitudes during winter conditions and a transition into the clean Arctic summer. Thirdly, the combination of results from both measurement periods for the determination of an anthropogenic influence on the radiative balance including the cloud formation processes.

The list of participating institutes separated according to the type of activities during ASTAR 2004 campaign is presented in figure 2.

In the frame of both of these campaigns the Lidar Group of AWI Potsdam contributes high quality measurements of tropospheric aerosols, using an especially for this purpose designed Airborne Mobile Aerosol Lidar (AMALi) integrated on board of the Polar 2 research aircraft (Stachlewska et al. [66]), providing information on the existence, backscatter and depolarisation of the vertical and horizontal extent of Arctic aerosols and/or mixed-phase clouds of low optical densities.

2.1.1 Airborne activities

The Polar 2 and Polar 4 airborne operations were carried out from Longyearbyen starting on 7 May 2004. The scientific routine flight operation with both aircrafts started on May 18 and finished on June 10. All flights were carried out without any unusual occurrences providing 120 h 20 min of measurement data.

The scientific equipment installed onboard was certified, according to the German regulations for aircraft operation, by DLR officials after approval of documents describing the scientific aim, measuring principle and technical description including the instrument scheme with a list of all devices where their size, weight, centre of gravity and required power consumption were specified. Also the calculations for the stability proof, the location plan of all components and cables inside the aircraft's cabin and wings, the block diagram

ASTAR 2004 ACTIVITIES			
Airborne	Ground based	Satellite	Modeling
AWI Bremerhaven / Potsdam, Germany	Koldewey station AWI Bremerhaven / Potsdam, Germany	AWI Bremerhaven / Potsdam, Germany	AWI Bremerhaven / Potsdam, Germany
NIPR Tokyo, Japan	Rabben station NIPR Tokyo, Japan	NIPR Tokyo, Japan	KNMI de Bilt, The Netherlands
ITM/MISU Stockholm, Sweden	Zeppelin Mountain ITM Stockholm, Sweden	NASA LaRC Hampton, USA	IUP Bremen, Germany
LaMP Clermont- Ferrand, France	Hornsund station IOPAN Sopot, Poland	NOAA Boulder, USA	NILU Oslo, Norway
DLR-IPA Oberpfaffenhofen, Germany	Norsk Polarinstittutt Longyearbyen, Norway		DLR-IPA Oberpfaffenhofen, Germany
Hokkaido University, Sapporo, Japan			
Nagoya University, Japan			

Figure 2: *Institutions involved in the international ASTAR 2004 project*

including ID-code of all electronic components, cables and plugs with scheme of their circuit breaker, as well as the plan of the gas pipes specifying its type, diameter, valves and inlet/outlet were prepared and certified. Afterwards the stability tests of each system and each rack, the gas operation test and the EMC ground test of electromagnetic compatibility with aircraft avionics for start-up, normal and emergency operation modes were performed closing the certification procedures (Wehrle et al. [67]).

The central data acquisition system called MEDUSA-P provided by OPTIMARE and used originally for maritime surveillance and pollution control over North and Baltic Seas (Zielinski [68]), was adapted to the operational conditions in the polar environment. The system measured, digitised and temporarily stored the data of most scientific instruments installed onboard both aircrafts (Garbrecht et al.[69]). It worked fine also for extreme conditions (temperatures below $-40^{\circ}C$ and flight altitudes up to $24.000\ ft$) during polar missions. The very high sampling rate varying between $20 - 100\ MHz$ and exact synchronisation of all measurements using the GPS time stamp distributed to all instruments through optical fibres was acquired for measurements in a highly turbulent atmosphere. The data acquired by MEDUSA-P were transferred to the scientific groups regularly after each flight within $2 - 3$ hours after a landing.

Scientific instrumentation onboard Polar 2 aircraft

The Polar 2 airplane was deployed to investigate cloud microphysical properties and to perform lidar measurements of vertical variation of the optical properties of aerosol in the lower troposphere. The measurements were done in one of the two configuration modes the 'clear-sky' mode (the AMALi lidar of the AWI-Potsdam) and the 'cloud' mode (the in-situ instrumentation of the Laboratoire de Météorologie Physique (LaMP), Clermont-Ferrand, France). However, a subsequent change between both modes during single flight mission was possible. During such alternated flights, usually, the cloud cover was first examined with the lidar before the in-situ measurements in clouds were made (c.cpt. 5.10).

The Polar 2 performed 13 lidar flights and 11 cloud physics flights, with 6 of them alternated, and 3 of them with the Polar 4 operating in the same region. Due to the different scientific requirements for both types of measurements the aircraft carried one operator for each scientific group allowing flight durations longer than $4\ h$ (possible only

for the Arctic configuration with wheel operation) at the maximum flight altitude set to 3 km (10.000 ft) due to lack of oxygen breathing system onboard.

Three racks installed perpendicularly to the axis of the aircraft were employed, with the first two reserved for the LaMP instrumentation and the AMALi lidar, while the third one contained the AWI meteorological and radiation sensors and the MEDUSA-P acquisition unit. The *CO*-analyser was installed next to the lidar Optical Assembly mounted at the opening in the front section of the cabin. The lidar operational range was limited to 2.5 km with respect to eye-safety of observers on the ground (c.cpt. 3). Other security features as a laser emergency switch, a labelling of the laser, a key off-switch, and screws secured with safety wires had to be employed. The lidar was connected to the aircraft power distribution by 5 plugs ($3 \times 220\text{ V}$, $2 \times 28\text{ V}$) compatible with the aircraft's standard provided by OPTIMARE. The data acquisition and storage was done with a lidar notebook. The lidar data backup by MEDUSA-P was not provided, however, the time stamp (RS 232 with 1 Hz), the online GPS data and (after each flight) an ASCII-data file of navigation and basic meteorology were provided. An overview of the instrumentation onboard the Polar 2 aircraft is presented in figure 3.

POLAR 2 / ASTAR 2004		
Measured property	Instrumentation	Institute
Backscatter coefficient at 532 nm and 1064 nm wavelength Depolarisation ratio at 532 nm	Mobile aerosol lidar AMALi	AWI
Short wave and long wave radiation	Spectral albedometer & UV spectrometer	AWI
Cloud ice crystal number concentration and size distribution	2D-C and FSSP-100	LaMP
Morphology of cloud ice crystals	Cloud Particle Imager	LaMP
Air mass tracers: carbon monoxide	CO monitors	AWI
In-situ ice water content	Nevzorov and FSSP-100	LaMP/AWI
Optical information of cloud particles (scattering phase function)	Polar Nephelometer	LaMP
Temperature, pressure etc.	Aircraft standard equipment	AWI / Optimare

Figure 3: *Instrumentation onboard Polar 2 during ASTAR 2004 campaign*

The AWI's AMALi lidar (c.cpt. 3), was operated without any problems during all 13 flight delivering about 25 h of lidar measurements. The extended observations taken at different days covered: the aerosol boundary layer and clouds over Isfjorden, Kongsfjorden, Advantdalen, and Storfjorden, few cross-sections over sea along NW-SE off the Svalbard coast line with wave-driven aerosol structures and aerosol gradients between different air masses, different aerosol content over ice and open water and the local dust plume over Adventdalen and Isfjorden. During two flights over Kongsfjorden and Storfjorden lidar measurements were partly combined with in-situ aerosol profile measurements taken by Polar 4 aircraft. One flight, partly combined with measurements at the Polish research station in Hornsund, was dedicated to investigations of air masses along the west and east coast offshore Sorkapland. Additionally, several combined measurements between the AMALi lidar and the stationary KARL lidar over Koldewey station in Ny-Ålesund were performed. The detailed information on each of the ASTAR 2004 AMALi flights can be found in Stachlewska and Neuber [70].

The LaMP's in-situ instrumentations (c.cpt. 5.10.2) used for the measurements of the microphysical and optical properties of cloud particles provided characterisation of the

mixed-phase of the Arctic clouds, with special focus on the investigation of the different ice crystal shape confined to distinct zones of the cloud systems. The cloud instrumentation worked fine during all flights except for May 29, when heavy icing of the Polar Nephelometer occurred while measuring in a supercooled stratocumulus deck. Several alternated measurements with AMALi dedicated to investigations of clouds structures offshore the west coast of Prins Karls Forland, Albertland and in the Storfjorden allowed for the feasibility study of the depolarisation effects in lidar signals due to presence of the ice crystals in the sampled cloud areas (c.pt. 5.10). One of the alternated AMALi/LaMP flights combined with an aerosol in-situ measurement from Polar 4 was dedicated to the study of the activation of aerosol particles to cloud droplets and ice crystals.

Scientific instrumentation onboard Polar 4 aircraft

The scientific equipment of the Polar 4 aircraft was used to investigate the physical, chemical and optical properties of aerosol throughout the whole troposphere under clear sky conditions. Polar 4 performed 25 aerosol flights carrying equipment of three different scientific groups onboard, each with an operator, which restricted flight duration to a maximum of $2\text{ h }45\text{ min}$. The operation up to 8 km (24.000 ft) with the oxygen breathing system onboard was possible.

The instrumentation onboard Polar 4 aircraft consisted of aerosol remote and in-situ instrumentation, and a standard meteorological and radiation instrumentation (c.fig. 4). Four racks were employed: the first one, installed parallel to the axis of the aircraft, was reserved for the DLR-IPA instrumentation, while the next three, installed perpendicularly to the axis of the aircraft, were reserved each for the ITM/MISU, the NIPR, and the MEDUSA-P with the AWI radiation units, respectively. The sunphotometer and the CO_2 -system were installed in the front part of the cabin. In order to reduce the power consumption onboard, the DLR-IPA and ITM/MISU instruments shared one pump for their inlets (the DLR-IPA FSSP-100 probe was kept as a backup system only), and the flow rate required by the NIPR inlet was reduced to 10 l min^{-1} , values comparable with ITM/MISU and DLR-IPA inlets. The MEDUSA-P online meteorological data (especially an on-line true air speed indicator) were required by all systems, while the time stamp was not.

Both of the AWI instruments (sunphotometer and ozone analyzer), and the NIPR payloads worked without trouble, with exception of the latter one during the icing event on May 29. The ITM/MISU and the DLR-IPA payloads worked fine, except on May 24 when two of four CPSA channels failed due to the Butanol flooding of the optics. Some marginal data loss of both the DLR-IPA and the ITM/MISU payloads occurred during three flights due to hard disk problems.

The aerosol measurements onboard Polar 4 covered mainly the vicinity of Isfjorden and the area over the sea west of Prins Karls Forland. Several flights were devoted to measure aerosol vertical profiles in Kongsfjorden and just offshore its mouth from the flight level of 60 m in the marine boundary layer up to 7 km in the free troposphere. Generally, during the whole campaign typical background conditions with low values of aerosol concentrations and extinctions and low variability were found throughout the troposphere during most of the flights (c.pt. 5.6.1).

2.1.2 Ground based, satellite and modelling activities

Ground based activities

The coordinated ground based activities took place in vicinity of Ny-Ålesund, namely at the AWI Koldewey Station, the Japanese Rabben Station and the Swedish Zeppelin Mountain Station, as well as at the Polish Research Station in Hornsund on the west coast of Sorekapland (c.fig. 1).

POLAR 4 / ASTAR 2004		
Measured property	Instrumentation	Institute
Size distribution of Aitken mode particles in 10-200 nm range	Differential Mobility Particle Sizer (DMPS) + CPC	ITM/MISU
Total aerosol number density	Condensation Particle Counter CPC	ITM/MISU
Aerosol size distribution	Optical particle counter 1	ITM/MISU
Aerosol light absorption	Particle soot absorption photometer 1 (PSAP)	ITM/MISU
Size distribution of volatile, semi-volatile and refractory Aitken mode particles	Volatility Differential Mobility Particle Sizer (V - DMPS) / Volatility Tandem Differential Mobility Analyzer (V-TDMA)	ITM/MISU
Aerosol size distribution	PCASP-100X and FSSP-300 Aerosol Spectrometer Probes	DLR-IPA
Aerosol size distribution	Wing mounted particle spectrometers (PCASP-100X, FSSP-300, FSSP-100, MASP)	DLR-IPA
Aerosol size distribution	Optical particle counter 2	Hokkaido Univ.
Ultrafine and Aitken particles, thermal stability	Condensation Particle Size Analyzer (CPSA) + thermodenuder	DLR-IPA
Particle scattering coefficient	Integrating nephelometer	Hokkaido Univ.
Particle absorption coefficient	Particle soot absorption photometer 2 (PSAP)	Hokkaido Univ.
Spectral extinction coefficient for wavelengths 350-1050 nm	Sun photometer	AWI
Chemical composition	Aerosol sampling with one-stage impactor and filters	NIPR
Ionic aerosol components	Filter Sampling	Hokkaido Univ.
Short wave and long wave radiation	Spectral albedometer & UV spectrometer	AWI
Air mass tracer: ozone	Ozone monitor	AWI
Water vapour	CR-2 hygrometer	NIPR
Temperature, pressure, humidity etc.	Aircraft standard equipment	AWI / Optinare

Figure 4: *Instrumentation onboard Polar 4 during ASTAR 2004 campaign*

All of these research stations provided the meteorological parameters wind, pressure, humidity and temperature and the measurements of optical and microphysical atmospheric properties (Herber et al. [65]). An overview of the measurements performed at the stations in Ny-Ålesund and Hornsund are given in figures 5 and 6, respectively.

The in-situ and remote ground based measurements generally confirmed the airborne observations. The clean conditions manifested in the low amounts of light absorbing particles (soot), very low concentrations of large particles, the low aerosol optical depth obtained from the sunphotometer and background values of backscatter and extinction coefficients. Generally, very low volume depolarisation recorded by KARL lidar justified the existence of only spherical particles (c.cpt. 5.6.1).

Satellite activities

The satellite observations (ATSR-2, ENVISAT/SCIAMACHY, ILAS II, MERIS, MODIS, OMI, SAGE III, SeaWiFS) with their high speed and global range complete the local measurements of the polar aircrafts and hence link local, regional and global processes. During the field campaigns their imagery is used on a daily basis for the general weather situation assessment and for pre-defining the areas where clear-sky and cloud measurements can be

Koldewey Station (Ny-Ålesund) / ASTAR 2004		
Measured property	Instrumentation	Institute
spectral aerosol optical depth	Full-Automatic Sun Photometer (SPIA)	AWI
backscatter and extinction coefficients profiles	Koldewey Aeerosol Raman Lidar (KARL)	AWI
chemical component of aerosols	Low- and High-Volume Aerosol Samplers	AWI
precipitation sampling	Wet only precipitation sampler	AWI
dry and wet deposition	Total deposition sampler	AWI
Rabben Station (Ny-Ålesund) / ASTAR 2004		
Measured property	Instrumentation	Institute
columnar spectral aerosol properties	I-Skyradiometer (ISKY)	NIPR
aerosol optical thickness	Grating Sunphotometer (GSUN)	NIPR
vertical aerosol concentration	Micro Pulse Lidar (MPL)	NIPR
monitoring sky condition	Sky Camera (SCAM)	NIPR
aerosol scattering	Integrating Nephelometer (IN)	NIPR
aerosol size distribution	Optical Particle Counter (OPC)	NIPR
aerosol absorption coefficient	Particle Soot/Absorption Photometer	Hokkaido Univ. NIPR
Zeppelin Mountain Station (Ny-Ålesund) / ASTAR 2004		
Measured property	Instrumentation	Institute
size distribution of Aitken mode particles in 10-200 nm range	Differential Mobility Particle Sizer (DMPS) + CPC	ITM/MISU
total aerosol number density	Condensation Particle Counter (CPC)	ITM/MISU
aerosol size distribution	Optical particle counter (OPC)	ITM/MISU
aerosol light absorption	Particle soot absorption photometer (PSAP)	ITM/MISU
size distribution of volatile, semi-volatile and refractory Aitken mode particles	Volatility Differential Mobility Particle Sizer (V - DMPS) Volatility Tandem Differential Mobility Analyzer (V-TDMA)	ITM/MISU

Figure 5: *Instrumentation in vicinity of Ny-Ålesund during ASTAR 2004 campaign*

carried out.

With respect to aerosol investigations, the validation of the satellite aerosol optical depth by the direct comparison with the airborne measurements (Treffeisen et al. [63]) allows for improvement of present algorithms of satellite retrievals for the aerosol optical thickness for high latitudes and low sun elevations in the Arctic (von Hoyningen-Huene et al. [23], Kokhanovsky et al. [71]). Hence, the regional extension of Arctic aerosol properties, necessary for the future modelling will be determined.

Modelling activities during the campaign

During the campaign, mainly the results of the European Centre for Medium-Range Weather Forecasts model (ECMWF, <http://www.ecmwf.int/>) were used for prediction of the synoptic scale and medium range weather forecasted for 726 h on a 6 h scale. The prediction was provided in terms of the dynamics charts with respect to the potential vorticity and sea level pressure; the clouds charts for low (below 800 hPa), mid (between 400 – 800 hPa), and high (above 400 hPa) cloud altitude, as well as the cloud partitioning with respect to the ice and water content. Finally, the meteorological charts included relative humidity, temperature, geopotential and wind. Additionally, forecast meteograms

Hornsund Station (Sorekapland) / ASTAR 2004		
Measured property	Instrumentation	Institute
aerosol concentration and aerosol size distribution	Classical Scattering Aerosol Spectrometer Probe (CSASP-100-HV-SP)	IPAS
ozone content aerosol optical thickness at 1020 nm	Microtops II Ozonometer	IPAS
aerosol size distribution	Airnet 310 Aerosol Particle Counter	IPAS
aerosol size distribution	Handilaz Aerosol Particle Counter	IPAS
surface albedo	NET Radiometer (CNR)	IPAS
spectral solar radiation	Precision Spectral Pyranometer (PSP)	IPAS
spectral extinction coefficient for wavelengths 350-1050 nm	Sun photometer	AWI

Figure 6: *Instrumentation of the Hornsund station during ASTAR 2004 campaign*

of total cloud cover, total precipitation, wind speed and temperature were provided for three locations; Ny-Ålesund, Longyearbyen and just offshore Hornsund.

The combination of the ECMWF forecast (provided by A. Dörnbrack, DLR-IPA, Germany), the forecasted 3-dim backward trajectories (provided by P. van Velthoven, KNMI, The Netherlands), the aerosol optical depth MATCH CTM model forecast (provided by P. Rash, NCAR, USA), the satellite imagery by MODIS, NOAA, combined with the daily flight-weather briefing (presented by L. Bergstadt, AVINOR, Svalbard) was used for the scientific decision-making concerning the flight activities.

On the other hand to explain the weather situation and the processes occurring in the atmosphere for particularly interesting weather events the results of the ECMWF operational analysis were used (c.cpt. 5.1).

The origin of the measured aerosol load with respect to its long-range transport was determined using the two trajectories models NOAA HYSPLIT (Draxler and Rolph [72]) and a particle dispersion model FLEXPART (Stohl et al. [73]).

The interpretation of the aerosol load with respect to its local origin was provided using the small-scale range dispersive EULAG model (Prusa and Smolarkiewicz [74], and Smolarkiewicz and Prusa [75]).

The regional atmospheric climate model HIRHAM

Three main issues are of concern for the post-campaign modelling. Firstly, an estimation of the climate effect caused by antropogenic aerosol (Arctic Haze) versus background conditions calculated for solar and terrestrial radiative balance modelled with different complexity. Secondly, the studies of the relevance of aerosol properties in arctic climate models by comparison of the aerosol effect to other forcing mechanisms to see its relative impact. Thirdly, the development of parameterisations of aerosol and cloud processes based on provided remote or in-situ observations.

The high resolution 3-dim regional atmospheric climate model HIRHAM (HIRHAM, <http://www.awi-potsdam.de/www-pot/hirham>), see: Dethloff et al. [20], Dethloff et al. [76], Rinke and Dethloff [77]) with the incorporated Global Aerosol Data Set (GADS) and the Arctic Aerosol Data Set (AADS) developed at ASTAR 2000 campaign used over an area covering the whole Arctic north of 65°N and integrated over a spring season of typical Arctic Haze reveal the realistic estimation on the direct effect of Arctic Haze on climate (Fortmann [37]). Moreover, the indirect influence on the large-scale and the meso-scale atmospheric circulation due to the aerosol-radiation-circulation feedback, as for example the scattering and absorption of radiation by aerosol, can cause pressure pattern changes

potentially able to modify Arctic teleconnection patterns (Rinke et al. [21]).

Similar modelling will be performed in the future for the ASTAR 2004 and 2007 campaigns, including new informations obtained from the airborne AMALi aerosol and clouds measurements and the airborne in-situ clouds observations performed onboard the Polar 2 aircraft. The campaigns will provide detailed data sets of optical parameters of Arctic Haze and Arctic clouds which will be used for parameterisation of such aerosols and clouds in the HIRHAM model, for which both parametrisations are still in the development phase.

2.2 Scientific activities during SVALEX 2005

The airborne activities of the Svalbard Experiment (SVALEX) campaign utilising the AWI research aircraft Polar 2 and the DLR research aircraft D-CFFU were conducted from Longyearbyen on Spitsbergen between 5-22 April 2005.

The Polar 2 aircraft was deployed during almost 20 flight hours for measurements of the ice surface structure and atmospheric turbulence above the ice shield to provide a parametrisation of the turbulent transport of energy and momentum for climate and weather models (Garbrecht et al. [78]). These investigations were combined with the D-CFFU aircraft radar measurements of the thickness, structure and surface of sea and land ice with almost 33 hours of observations for this activity.

Additionally, the SVALEX campaign aimed to deal with the characteristics of an increased springtime tropospheric aerosol load typical for an Arctic Haze event and investigations of its effects on climate. The AMALi lidar onboard Polar 2 provided almost 20 hours of measurements allowing to determine the optical characteristics of such aerosol and its spatial (in)homogeneity and distribution. At the same time the aim of the ground based measurements was, similarly to the ASTAR 2004 campaign, to provide a comprehensive characterisation of the temporal and vertical distribution of Arctic Haze over Ny-Ålesund using the Koldewey Aerosol Raman Lidar (KARL), the sun photometer running in automatic mode and delivering the aerosol optical depth spectrum from UV to near IR.

The optical depth spectra were measured also with a sun photometer in Longyearbyen. Additionally, the radio/ozone soundings and the meteorological measurements were performed by the staff of the Koldewey Station. Furthermore, the chemical characterisation of low altitude aerosols using combined MicroPulse Lidar observations with the measurements of the chemical state of surface layer aerosol, and the investigations of precipitation were performed by NIPR instrumentation at the Koldewey and Rabben Stations.

The weather prediction for the next hours/days provided by AVINOR together with the MODIS and NOAA satellite imagery and predicted trajectories provided by KNMI allowed for the scientific planning of each flight mission. Afterwards the long-range transport analysis was made with help of the NOAA HYSPLIT backtrajectories, while for particular days also the FLEXPART calculations were performed (c.pt. 5.6)

Due to unfavourable weather conditions and according technical problems, the test flight operations started only on 8 April for Polar 2 and on 12 April for D-CFFU. Generally, weather conditions often limited aircraft activities due to cloud ceiling, visibility, cross wind, snowfall and snowstorms. However, the AMALi scientific operation was possible on 4 days of clear-sky conditions between 12-16 April.

In total 18 h 30 min flight observations were performed with 13 successful overflights over Ny-Ålesund in order to allow the combination of the KARL and AMALi data sets and the other supporting ground based measurements. During these 4 days, an Arctic Haze event was clearly seen from the measurements with both AMALi and KARL lidars, as well as with both sunphotometers in Longyearbyen and Ny-Ålesund (c.pt. 5.6 and 5.7. The detailed information on each of the AMALi flights can be found in Stachlewska [79].

3 AWI lidars for measurements during Arctic field campaigns

In the frame of the ASTAR 2004 and the SVALEX 2005 campaigns the Lidar Group of the AWI Potsdam Research Unit performed high quality measurements of the tropospheric aerosols, using two lidar systems, the stationary zenith-aiming Koldewey Aerosol Raman Lidar (KARL) and the nadir-aiming Airborne Mobile Aerosol Lidar (AMALi) integrated onboard the Polar2 research aircraft. In this chapter a short description of the KARL lidar (c.cpt. 3.1) and a detailed description of the AMALi lidar (c.cpt. 3.2) are given.

3.1 The stationary Koldewey Aerosol Raman Lidar KARL

The Koldewey Aerosol Raman Lidar (KARL) was developed in 1998 by the AWI-Potsdam Lidar Group (Schumacher [64]). It is a ground based system firmly integrated into the Koldewey station in Ny Ålesund, Spitsbergen ($78.9^\circ N$, $11.9^\circ E$) aiming at continuous regular detection of tropospheric aerosols and water vapour.

It consists of a Nd:Yag laser operating with 30 Hz repetition rate at 355 nm , linearly polarised 532 nm and 1064 nm with power around 2 W for each wavelength. The receiving system employs two mirrors; a small telescope mirror of 10.8 cm diameter and field of view of 2.25 $mrad$ for near range detection from 400 m to 6 km and a large telescope mirror of 30 cm diameter and field of view of 0.83 $mrad$ for far range measurements from 2 km to above the tropopause. Detection is provided for the three wavelengths together with depolarisation information for 532 nm . Moreover, the N_2 Raman-shifted wavelengths of 387 nm and 607 nm , as well as the water-vapour lines of 407 nm and 660 nm can be recorded. The elastic scattering profiles are typically provided with 60 m range resolution and integration times over 10 min when the standard automatised evaluation routine is applied. The backscatter profiles are ranging from geometrical compression at approximately 400 m up to 15 km during daylight and 18 km at night. The inelastic scattering profiles for the Raman channels are provided generally with weaker resolution, due to the much lower cross-section for Raman scattering in the atmosphere. Therefore a height resolution of 300 m for integration times over an hour is necessary. These profiles are ranging up to 4 km for the daytime and 8 km at nighttime measurements.

Since 1998 the system went through extended improvements towards development unto its present form, as for example the inclusion of water vapour and IR detection channels in 1999 and UV detection channel in 2001. The exchange of the Nd:Yag laser for a new generation one operating with 50 Hz repetition rate and emitting more powerful laser pulses of 1000 mJ at IR, 500 mJ at VIS, and 275 mJ UV is planned for April 2006. More information about KARL and its application is given in Ritter et al. [80] and Ritter and Neuber [81].

3.2 The new Airborne Mobile Aerosol Lidar AMALi

The Airborne Mobile Aerosol Lidar (AMALi) was developed in 2003 by the AWI-Potsdam Lidar Group (Stachlewska et al. [66]). This small robust easy to transport backscatter lidar (c.fig. 7) is used for remote simultaneous high resolution detection of vertical and horizontal extent of tropospheric aerosol load at 1064 nm and 532 nm wavelength with additional depolarisation measurements at the latter one. The lidar is mounted in two small, portable modules. An Optical Assembly (70×50×25 cm) comprises the laser head, directing and receiving optics, and electro-optical detectors. The laser control and cooling unit, the data acquisition system (laptop and transient recorders) and the safety breaker box are installed in a standard size rack (55×50×60 cm).

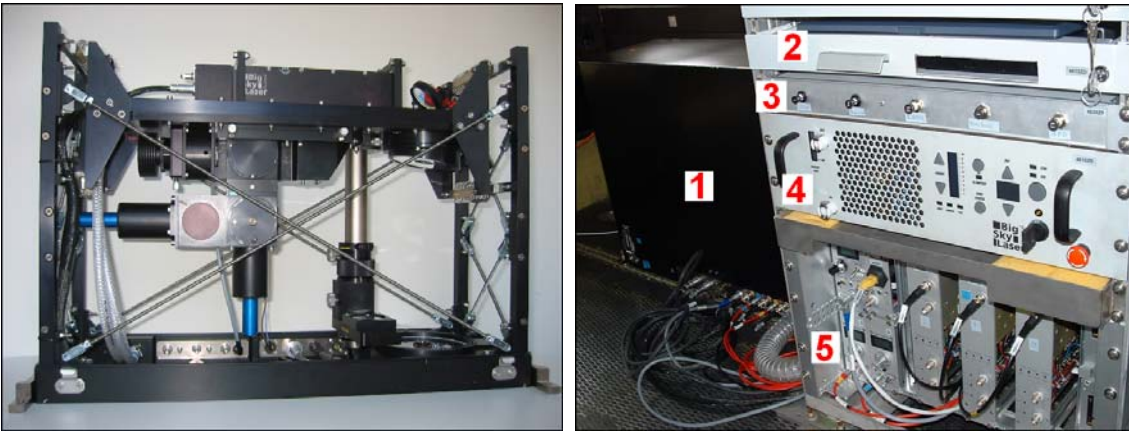


Figure 7: *The AMALi in nadir-airborne configuration onboard Polar 2 aircraft (right), inside of the optical assembly (left). The numbers indicate the main elements of the AMALi lidar; 1.optical assembly 2.laptop 3.safety breaker box 4.laser control and cooling unit 5.transient recorder.*

The design of AMALi allows downward measurements in vertical direction for the current configuration onboard AWI’s Polar/,2 aircraft. When the lidar is operated at the ground level or integrated in a car or a ship, measurements are usually taken vertically upward (system is turned upside-down), however, horizontal measurements are also possible (system lying on a side). It can be used also in a scanning mode, if set on a platform allowing movement of the whole system in vertical/horizontal direction. Despite its relatively small size AMALi in ground based configuration is powerful enough to cover the range up to the tropopause level. For airborne measurements its range is limited to the maximum flight altitude, the maximum nominal operation height for the laser and eye-safety constraints.

The rapid data acquisition system enables recording of lidar profiles with single-shot resolution providing high spatial and, hence, horizontal resolution information about the state of the atmosphere between the flight altitude and the ground/sea level during the measurement. The online, quick-look data evaluation software allows immediate, qualitative interpretation of the aerosol content during the flight, and thus guidance of a second research aircraft for in-situ measurements into particularly interesting areas.

3.2.1 Optical assembly

The transmitting and receiving systems are mounted inside an optical assembly designed by AWI-Potsdam Lidar Group and manufactured by Steingross Feinmechanik, Berlin. This small, light weight module ($70 \times 50 \times 25$ cm, 38 kg) called optical assembly (c.cpt. 7, left) was designed especially to fit a limited space available for the lidar instrument on board the Polar 2, the AWI research aircraft Dornier Do 228.

All vital lidar parts, i.e. Nd:Yag laser head, directing optics, receiving off-axis telescope mirror and detector block with its opto-electronical elements are mounted onto the same optical bench (c.cpt. 8). Such single-optical-bench design simplifies single-adjustment of all optical elements and ensures reliable and trouble-free utilisation during campaigns without need of re-adjustment. The optical bench itself hangs on anti-shock springs attached to four posts. The springs eliminate vibrations of the optical bench while operation on board of the aircraft. The weight and position of all elements (on the optical bench) are chosen in a way that the centre of gravity results in the middle of the optical assembly. The four posts together with a base plate form a massive construction providing mechanical

stability to the system. During measurements the optical assembly is covered with a sheet metal box capturing any scattered laser light and thereby ensuring the safety of pilots and operators, as well as protecting the detection system from stray light and background radiation.

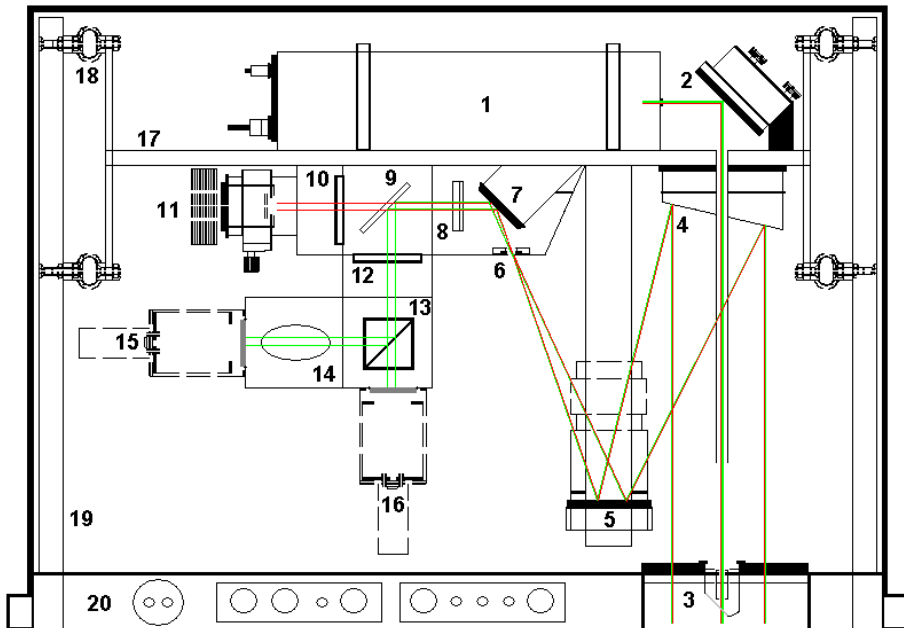


Figure 8: *The AMALi optical assembly with schematically drawn ray-tracking at 532 nm (green) and 1064 nm (red). The numbers indicate the main components in the assembly; 1.laser head 2.directing mirror in piezo motor 3.window with Brewsters angle 4.off-axis parabolic mirror 5.first folding mirror 6.pinhole 7.second folding mirror 8.achromatic lens 9.beam splitter 10.interference filter for 1064 nm channel 11.APD for 1064 nm detection 12.interference filter for 532 nm channel 13.polarising cube 14.thin film polarising filter 15.PMT for perpendicular 532 nm detection 16.PMT for parallel 532 nm detection 17.optical bench 18.springs 19.posts 20.base plate.*

3.2.2 Transmitting system

As a transmitter custom designed small rugged and easy to handle flashlamp pumped Nd:YAG pulsed laser (CRF-200, Big Sky Quantel, Montana, USA) is used. It is provided with portable power supply and cooling unit mounted in a single, low weight (3 kg) and space requirements (12×45×48 cm) unit. The laser, equipped with doubler crystal, emits simultaneously 1064 nm and linearly polarised 532 nm wavelengths as 11 ns short light pulses with energies of 60 mJ and 120 mJ, respectively, with the pulse repetition rate of 15 Hz.

The double wavelength backscatter lidar scheme was chosen for its conceptual simplicity (Shimoda [82]) ensuring an easy and trouble-free operation during field campaigns under tough conditions, as for example onboard of the AWI research aircraft Polar 2 during field campaigns in the Arctic. The laser is cooled with an ethylene glycol and water 1:1 solution to ensure that the liquid will not freeze while the laser is operating under arctic weather conditions and at high altitudes, whereby the maximum nominal operation height for the laser is set to 3 km.

The laser divergence δ , the telescope mirror diameter T and the pinhole diameter s together with the laser pulse power and repetition rate were chosen with the constrain to achieve the lowest possible geometric compression ξ with lowest integration times for the

weakest detection channel (532 nm perpendicular) during airborne nadir-looking operation. The second important constrain was the choice of the lidar components in a way to assure the lowest weight, space and energy consumption for airborne operation mode.

To ensure the eye-safety neither filters nor a beam expander were used. For a laser working with full energy and simultaneously emitting both wavelengths the large laser beam divergence δ of 2.6 mrad ensures that the laser light is eye-safe at distances greater than 2.5 km off the lidar system (Wehrle et al.[83]). The diameter of the laser beam at a laser head g_0 is 6 mm.

The detection range during the airborne measurements in nadir configuration is limited, on the one hand by the maximum of allowed flight altitude without using oxygen masks by the pilots and scientific crew, which is set to 3 km for the current installation in a Dornier Do288 aircraft, and on the other hand, by eye-safety constraints. Hence, operation of the AMALi during the airborne measurements is limited to altitudes between 2.5 – 3 km above ground/sea level.

A double plain mirror integrated in piezo stepper motor at an angle of approximately 45° redirects the laser beam into the opening in the optical bench on which the laser head is resting and sends it almost parallel to the optical axis of the receiving telescope mirror, while the distance between the telescope optical axis and the laser beam axis d_0 is set to 7.5 mm. Such construction allows fine adjustment of an overlap between a laser beam and a telescope mirror field of view φ of 3.1 mrad resulting in complete overlap at a full field of view ($\xi = \frac{2d_0 + T + g_0}{2\theta + \varphi - \delta}$ for small θ , φ and δ angles approximation) at a distance 235 m when the laser beam is not inclined ($\theta = 0$), and in a minimum complete overlap distance ξ_{min} of 155 m for the maximum applicable inclination angle ($\theta = \frac{\varphi - \delta}{2}$) of 0.27 mrad.

3.2.3 Receiving and detecting system

The optical layout of the receiver is composed with all signal collecting lidar parts attached to the bottom of the optical bench. An off-axis parabolic primary mirror is mounted in a way that the laser light is sent through its central perforation of 3.1 cm diameter, a plain secondary mirror is mounted on a rod attached to the optical bench, and a detector block with its opto-electronical elements mounted in box-moduls (c.ept. 8).

Since in this lidar system it is not necessary to use an aperture that is completely rotationally symmetric the off-axis optics can be used to minimise the system size, weight and costs, while at the same time maximise its efficiency. The use of the off-axis configuration frees the system from astigmatism, while the use of the aspherical, parabolic mirror frees the system from spherical aberrations (Luneburg [84]).

The backscattered light is collected by an off-axis parabolic mirror coated with protected silver coating (OAP 18-05-04Q, Space Optics Research Labs, USA) with diameter of 10.2 cm and a clear aperture of 9.9 cm. The focal length is 48.0 cm, while the off-axis distance is 12,7 cm. The mirror surface accuracy is high with figure (defines mirror roughness) of $\lambda/10$ wave peak to valley at 632.8 nm over 99% of the clear aperture and slope (defines mirror shape) of $\lambda/8$ waves per inch at 90%.

The high reflective (near-UV, VIS and near-IR spectra) silver coating is a soft chemical surface with low durability, damage threshold and oxidation tarnishing. Hence, the silver layer is additionally over-coated with a hard, single, dielectric layer of half-wavelength optical thickness at 550 nm. This protective film arrests oxidation, helps maintain high reflectance, improves the minor abrasions and tarnish resistance, while only marginally affecting the optical properties.

The light collected with the off-axis mirror is redirected by the first folding mirror onto a 1.5 mm pinhole on the detector block. Such a choice of pinhole size together with the parameters of the primary mirror results in 3.1 mrad field of view, necessary for the detection of the complete return signal of the strongly divergent laser beam. After passing

the pinhole the light is redirected using the second plane folding mirror to an achromatic lens used to produce parallel rays while avoiding chromatic aberration (Luneburg [84]).

The signals of both frequencies are separated into two different detection channels using a dichroic mirror inclined at 45° which transmits the 1064 nm and reflects the 532 nm signal. The last wavelength is additionally separated into its parallel and perpendicular component using a polarising cube beam splitter. In front of the photo-detectors interference filters are placed to reduce the background daylight radiation. For the IR channel a 1.0 nm wide interference filter centred around 1064 nm is used, and for both VIS channels a 0.15 nm wide interference filter centred around 532 nm . Due to the limited range of the airborne signals a strong peak of the ground return occurs. However, the use of absorptive neutral density filters to reduce the intensity of the incoming light is not necessary. The less intense, perpendicular component of the 532 nm channel is additionally filtered for cross-talk using a thin film polarising filter at a 56° angle.

3.2.4 Data acquisition system

A single laptop computer (TOSHIBA, 2 GHz , CPU 30 GB , HD 256 MB RAM, USB-RS 232, Windows XP-Pro, OPS english) fully controls the laser, transient recorders, detectors, and data acquisition, storage, processing, quick-look evaluation and display programs utilising LabVIEW software. As data acquisition system a transient recorder (TR20-80, LICEL GbR, Berlin) combining an A/D converter (12 bit at 20 MHz) for analog detection with a 250 MHz fast photon counting system is used. An ethernet control module using a TPC/IP protocol allows remote control and data transfer for both photon counting and analog recorders. For the detection of the 1064 nm channel a Peltier cooled Si Avalanche Photo-Diode (APD) is used, and for the detection at both 532 nm channels two Hamamatsu R7400 photomultipliers (PMT).

Transient recorders register the pulses with a maximum sampling rate of 20 MHz corresponding to a height resolution of 7.5 m for one range bin. In a nadir-aiming airborne configuration typically each new lidar return signal from each of the three channels is appended and stored with a time resolution of 1 s in a block file of 2 min . However, a resolution as fine as a single-shot acquisition is also possible.

In a zenith-looking ground based configuration a standard LICEL software is employed. Here each new lidar return signal from each channel is stored separately at a time resolution of minimum 1 s and hence, a single-shot acquisition is not possible. With this standard software the profiles up to the tropopause level can be easily obtained.

For the nadir-airborne applications a custom designed LICEL software is employed. Here, the length of each collected signal is limited to 1000 range bins (7.5 km) to decrease the time needed for data transfer between transient recorder and the laptop (smaller size of data files). At the same time, it provides sufficient number of bins for the required range determined by the altitude of the flying aircraft for nadir-aiming configuration, i.e. maximum of 3 km above sea level. For this short distance (significantly shorter than the zenith-aiming ground based range), a strong received signal with sufficient signal-to-noise ratio is guaranteed, so that the photomultipliers can be operated in an analog mode only (Goodman [85]).

Additionally, the measurements in nadir airborne configuration generally provide a better signal-to-noise ratio at far distances from the aircraft, as the measured aerosol concentration and the air density increases towards the ground. On the other hand, for the airborne applications only short integration times are allowed in order to achieve an sufficient horizontal resolution. An acceptable signal-to-noise ratio is achieved for an integration time of 1 s corresponding to a horizontal resolution between 46 m and 77 m at a minimum of 166 km/h (90 kt) and maximum of 278 km/h (150 kt) aircraft cruising speed over ground, respectively.

The limited range of the recorded airborne signals results in a difficulty to obtain the background light intensity, which has to be subtracted for the evaluation of the lidar data. To overcome this problem, the data acquisition is started by an adjustable pretrigger to the laser Q-switch, designed by LICEL especially for the AMALi airborne applications. The timing of the pretrigger is usually chosen up to a value of $25 \mu\text{s}$ corresponding to 500 range bins (3750 m) of the signal (c.cpt. 9).

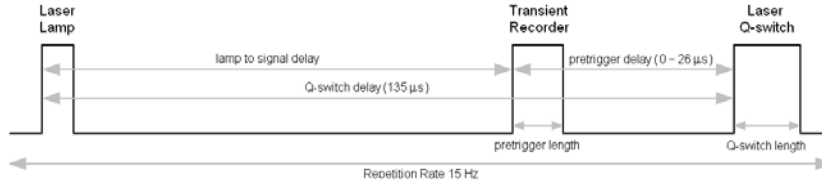


Figure 9: *The AMALi adjustable pretriggering scheme. The timing of the pretrigger can be chosen up to a maximum of $26 \mu\text{s}$.*

The lidar profiles are stored on the laptop and provide information about the state of the atmosphere between the full overlap and the ground or sea level during the flight. They can be viewed online during the flight using a special designed feature of so called quick-look evaluation screen in the data acquisition programmes. Each second one of the display screens provide all three currently measured raw signal profiles. Similarly, three other screens are frequently updated with background and range corrected signal profiles at both 1064 nm and parallel 532 nm channels, as well as with depolarisation ratio ($532 \text{ nm perp.}/532 \text{ nm par.}$) profiles, all averaged over 15 s .

This online quick-look data evaluation allows immediate 'first-guess' interpretation of the aerosol data during the flight providing also sufficient information for an onboard lidar operator to, for example, guide another research aircraft for specific in-situ measurements. During the ASTAR 2004 campaign the quick-look evaluation feature allowed also to guide alternated Polar 2 measurements, i.e. after identification by lidar measurements of particularly interesting regions of mixed-phase clouds (indication of height and relative concentration of water droplets and/or ice crystals areas) the aircraft descended into specified parts of these clouds for in-situ measurements of their microphysical and optical parameters (c.cpt. 5.10). An exemplary quick-look real-time evaluation displays obtained during this particular flight are shown in figure 10.

3.2.5 AMALi end-products and their applications

The AMALi lidar provides a high quality information on existence, altitude distribution, backscatter and depolarisation of the vertical and horizontal extent of tropospheric aerosols and low optical thickness clouds, by delivering profiles of the range and background corrected signals, the aerosol backscatter coefficients, the aerosol particles non-sphericity (depolarisation information) and, by the remedy of additional information or instrumentation, even the extinction coefficients.

As a first type end-product, for both nadir-looking airborne as well as zenith-looking ground based lidar configurations, profiles of background and range corrected signal for both 1064 nm and parallel 532 nm channels and profiles of depolarisation ratio at 532 nm are delivered. All these profiles are averaged over 1 s with range resolution of 7.5 m and horizontal resolution of 67 m for typical aircraft's cruising speed over ground of 130 kt . Typical length of airborne profiles vary between 2.5 - 2.7 km depending on flight altitude and taking into account the 155 - 235 m losses due to geometrical compression near the lidar. For the airborne measurements the background correction value for each profile is obtained from the pretrigger part of the signal and extracted from each profile separately.

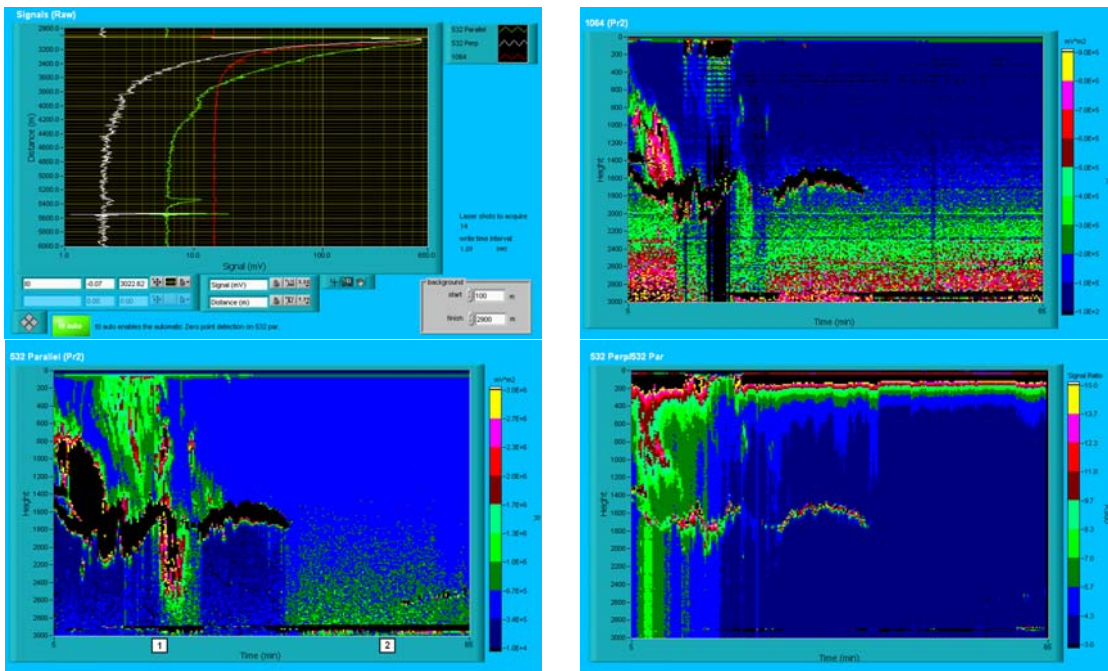


Figure 10: *The quick-look displays of the AMALi on-line software: the raw signals at 532nm, 532nm perp. and 1064nm (left top), the range and background corrected signals at 532nm (left bottom) and 1064nm (right top), and the depolarisation ratio at 532nm (right bottom) providing the signal evolution in a real-time during the flight.*

In a zenith-looking ground based configuration profiles obtained with the same temporal and range resolution easily reach the tropopause level. Cirrus cloud detection can be achieved with only a few pulses. Background correction, i.e. background light elimination from the lidar signals, for the ground based measurements is done in a standard way using Rayleigh atmosphere approximation (c.cpt. 4.3.3).

A second type end-product, i.e. the backscatter and extinction coefficients, are also calculated differently depending on lidar configuration mode. For the airborne data evaluation the standard Klett approach cannot be used due to the limited signal range resulting in a signal calibration problem. Hence, a new improved iterative Klett's approach for the evaluation of airborne lidar data, independent of the existence of aerosol free layers or in-situ calibration measurement, was developed (c.cpt. 4.6 and 5.5). The application of this new approach allows to provide calibrated backscatter ratios at any time during the whole flight (c.cpt. 22). The typical backscatter coefficient profile at 532nm is averaged over 15s with 7.5m range resolution and 1km horizontal resolution for 130kt aircraft's cruising speed over ground. The extinction coefficient profiles can be calculated from this profiles in a standard Klett way by the appropriate lidar ratio assumption. Additionally, for each of the time periods when the AMALi overflies the KARL lidar the direct calculation of the extinction and backscatter coefficient profiles with 8-10min temporal resolution and 60m horizontal resolution is performed using the two-stream approach (c.cpt. 4.5 and 5.4). The range of these profiles is strongly determined by the altitudes where the method is applicable, (both lidars must sample into the same atmosphere).

For ground based AMALi configuration the standard Klett's backward approach with assumption of altitude dependent lidar ratio and data calibration in aerosol free tropopause level is used (c.cpt. 4.3.3) providing the profiles with 1min temporal and 7.5m range resolution.

4 Data evaluation schemes and error sources discussion

Obtaining information on optical properties of aerosol particles in the atmosphere, i.e. obtaining extinction α^{part} and backscatter β^{part} coefficients profiles independently from each other without an assumption of lidar ratio $B = \frac{\alpha^{part}}{\beta^{part}}$, signifies a great step forward into interpretation of lidar data. The aerosol particle microphysical parameters, i.e. the particle index of refraction m and the size distribution function σ , can be derived from a set of α^{part} and β^{part} profiles obtained for different wavelengths (Müller et al. [86], Böckmann [87], Veselovskii et al. [88]) with the help of the generalized Lorenz-Mie theory (GLMT) of an arbitrary shaped beam of light scattered by homogeneous isotropic spheres derived by Lorenz and, independently, Love [89], Mie [90], and Debye [91]. Gouesbet and Grehan [92] propose a similar theory built by the synthesis of the GLMT and the interaction theory between a plane wave and assemblies of spheres and/or aggregates. The theory on electromagnetic radiation interaction with arbitrarily shaped and oriented small particles was recently revised by Mishchenko et al. [93]).

Such calculation, however, consists of a mathematically ill-posed inversion problem (Bronsztejn and Siemiendiajew [94]). The emergent Lorenz-Mie efficiencies act differently for extinction and backscatter, hence, any inversion of microphysical parameters feeded with both coefficients calculated independently can be performed more precisely, especially for the determination of the particle size distribution (Böckmann [87], Böckmann et al. [27]). Unfortunately, an elastic backscatter lidar alone cannot provide complete information for such an inversion, due to the existence of two unknowns, the α and β coefficients, in only one equation describing the lidar return signal (c.eq. 5). The traditional Klett approach for the evaluation of elastic backscatter lidar data requires knowledge or assumption of the lidar ratio and an extinction or backscatter coefficient calibration value (Klett [28], [29]). For the numerically stable backward Klett-Fernald solution (c.cpt. 4.3.3) the appropriate choice of a height and wavelength dependent lidar ratio $B(h, \lambda)$ is crucial to provide accurate α^{part} and β^{part} profiles. Such proper choice is difficult since the actual lidar ratio of aerosol is usually not very well known in the troposphere and varies greatly with aerosol size and its chemical composition. Generally, it is larger for intrinsic dark particles, as soot, and for particles small in comparison to the employed wavelength (Ackermann [95]).

The inclusion of a Raman-shifted detection line in the lidar instrument provides the needed independent information (c.cpt. 4.4) and allows the direct retrieval of extinction and backscatter (Ansmann et al. [96]). However, the cross-section for the Raman-shifted inelastic scattering, so called Raman scattering (Demtröder [97]) of laser light by matter, is almost three orders of magnitude lower than the cross-section for the elastic interaction, i.e. the Lorenz-Mie scattering or the Rayleigh scattering (Rayleigh [98], Young [99]), which results in significantly more noise polluted signals.

Another approach providing such an independent information, the two-stream inversion (c.cpt. 4.5), also referred to as bipath or double-ended lidar method, requires the usage of two elastic backscatter lidar systems looking into opposite directions. The method, introduced by Kunz [31] and recently revised by Cuesta and Flamant [34], is considered to be applicable not only to the airborne lidar data evaluation but also for future evaluation and validation of satellite lidar data. Though the method was already applied to opposite looking lidars by Hughes and Paulson [32] and Jørgensen et al. [100], only very recently the first application of this approach to real airborne and ground based lidar data by Stachlewska et al. [33] demonstrated its feasibility. The two-stream approach allows the direct retrieval of the height dependent extinction coefficient without any a priori assumptions, normalisation or calibration. The only prerequisite to calculate the backscatter coefficient is knowledge of, usually unknown, lidar constants C of the employed instruments or a backscatter value β_{ref} at any given height in the measured interval (c.cpt. 4.5).

The instrumental constants of both a ground based C_K and an airborne C_A lidar, which usually are difficult to obtain, can be easily estimated within a few percent uncertainty, in the case that one of the lidars observes any aerosol poor layer, as for example in the tropopause. Finally, with knowledge of the calibration constant of the airborne lidar C_A it is possible to retrieve the calibrated airborne lidar backscatter coefficient profiles for measurements taken during the whole flight, even in case when backscatter calibration instrumentation and/or laser beam scanning facilities are not available onboard (Stachlewska et al. [36]).

4.1 Backscatter lidar techniques

Lidar techniques belong to the remote systems based on emission and detection of waves (light, radio, sound or ultrasound) using the instrument itself for transmitting and receiving backward reflected waves (Measures [26], Andrews [101], Jensen [22]). In case of lidar laser light pulses, consisting of one or more wavelengths, are transmitted into the atmosphere vertically or at a particular angle θ . They interact with and are changed by atmospheric molecules and particles causing alterations in the light intensity and wavelength according to the strength of optical interaction and the concentration of the interacting species in the atmosphere. Some of the light is scattered back from the target to the lidar instrument where the return signal is collected using a telescope mirror. The change in the properties of the light enables some information of the target and, consequently, characteristic attributes of the composition and physical state of the atmosphere can be deduced from the lidar data.

Backscattering and extinction are the only optical processes measured by the system.

The signals are mainly due to the elastic scattering ($\lambda_{em} = \lambda_{det}$) on any air molecules and tiny particles for which the particle size a is much smaller than the emitted wavelength $a < 0.1 \lambda_{em}$ in case of the Rayleigh scattering, and on particles, such as aerosols and dust, for which $a \cong \lambda_{em}$ in case of the Lorenz-Mie scattering. The relatively high cross-section for these types of scattering makes the signal detection easy and suites the elastic scattering lidars as very valuable for observations of the aerosol vertical distribution, since already simple backscatter signals at almost any lidar wavelength give a qualitative impression about the vertical distribution of the scatterers.

Apart from mentioned elastic lidars, for which emission and detection are done for the same laser wavelengths, inelastic (Raman) lidars are widely used in the European lidar community (Matthias et al. [102], Bösenberg and Matthias et al. [25]). The Raman aerosol lidar uses the inelastic scattering principle with $\lambda_{em} \neq \lambda_{det}$, for which an additional detection is done for the backscattered signal at a Raman-shifted wavelength of a particular molecule (Goldsmith et al. [103]). Due to the very weak cross-section for Raman scattering ($10^{-32} - 10^{-35} \text{ cm}^2$) usually the inelastic interaction of laser pulses with O_2 and/or N_2 molecules is used, taking the advantage of their high concentrations and large percentage in the air in comparison with other gaseous species, i.e. 21% and 78%, respectively. In these systems the energy shift towards the red or blue spectral range of Raman scattering depends on the incoming frequency of the photon and the molecule type. Usually, the detection is done for the wavelength of the strongest shifted return, i.e. for a N_2 molecule illuminated by 532 nm light, the strongest lines occur at a shift of 75 nm and for O_2 of 48 nm, both towards red light (Stokes shift).

The analysis of registered lidar signals allows the retrieval of α and β , and the determination of the concentration and type of aerosol. In the case of measurements with a set of wavelengths it is also possible to determine the size distribution of particles (Rajeev and Parameswaran [104]). Additionally, the detection of depolarisation of the backscattered light, i.e. detection of height dependent depolarisation ratio profiles, allows an estimation of the state of the particles interacting with light. The depolarisation ratio is defined

as the ratio between the reflectivity received at vertically polarised wavelength λ_{\perp} , but transmitted with horizontally polarised wavelength λ_{\parallel} , and the reflectivity at horizontal polarisation, i.e. $D(h) = \frac{\lambda_{\perp}}{\lambda_{\parallel}}$. The depolarisation of the horizontally polarised pulse is caused by non-spherical particles not aligned horizontally. The wet spherical particles do not change the polarisation of backscattered laser light $D < 1.4\%$ (normally very small for rain around $-40dB$), while the continental aerosol particles of rather nonspherical shape or the ice crystals depolarise strongly D up to 50% (for melting snow, water coated hail or graupel it varies between $-20dB$ up to $-10dB$). If non-spherical particles align with spherical-like symmetry of crystal shape the depolarisation information might be lost.

The transmission of the laser pulse instead of a continuous wave into the atmosphere at an angle θ allows the determination of the range to the target h from the duration time t the laser pulse travels to the target and back with the velocity of light c from $h = \frac{ct}{2} \cdot \cos\theta$ (where only single scattering is considered).

4.2 Backscatter lidar equation

The lidar equation describes the received signal as a function of the atmospheric and system parameters, whereby assumptions of quasi-monochromatic, coherent emitted laser light and instantaneous elastic or inelastic scattering are taken into account, while processes of multiple scattering of light are being neglected (Shimoda [82]). The lidar equation is usually written in the following form

$$P(h, \lambda) = P(h_0, \lambda)\xi(\lambda)\xi(h)\Delta h \frac{A}{h^2}\beta(h, \lambda)T^2(h, \lambda) \quad (1)$$

where λ denotes the emitted wavelength, h the distance between the lidar and the target particle or molecule. $P(h_0, \lambda)$ is the mean number of photons in the emitted laser pulse, i.e. the intensity of the wavelength dependent laser pulse emitted at a time $t_0 = 2h_0/c$, while $P(h, \lambda)$ is the mean number of photons detected with the photodetector, i.e. the intensity of the detected wavelength dependent backscattered signal at a time $t = 2h/c$. The spectral efficiency of the detection system $\xi(\lambda)$ depends on spectral efficiency of the photo-detector and the spectral transmittance of the optical elements. $\xi(h)$ is the geometrical efficiency of the detection system dependent on geometrical compression (called also overlap function between the emitted laser beam and the field of view of the telescope). A/h^2 is the angle of signal collection with the effective telescope surface of A , and Δh describes the spatial resolution of the system, which is by definition determined by the laser pulse duration τ but in reality determined by the slowest component of the system (photonmultiplier or transient recorder) and hence $\Delta h \gg c\tau/2$.

The last term of the lidar equation $T(h, \lambda)$ describes, according to the Lambert-Bouguer-Beer's law (Andrews [101]), the transmission of the laser energy through the atmosphere, which yields, for a vertically aiming lidar, in an exponential attenuation of the laser radiation due to the optical mass and optical depth $\tau_{tot}(\lambda)$ of all molecules and particles present in the atmosphere on the way of the laser beam. Hence, $T(h, \lambda)$ depends on the extinction of the signal due to scattering and absorption on the way from the source of lidar radiation to the range h and back.

$$T(h, \lambda) = \exp\left(-\int_{h_0}^h \alpha(\tilde{h}, \lambda)d\tilde{h}\right) \quad (2)$$

The $\beta(h, \lambda)$ and $\alpha(h, \lambda)$ denote the total backscatter and the total extinction coefficients depending on the total number of molecules and particles scattering and/or absorbing the laser light at the height h above ground.

$$\beta(h, \lambda) = \beta^{mol}(h, \lambda) + \beta^{part}(h, \lambda) \quad (3)$$

$$\alpha(h, \lambda) = \alpha_{scat}^{mol}(h, \lambda) + \alpha_{scat}^{part}(h, \lambda) + \alpha_{abs}^{mol}(h, \lambda) + \alpha_{abs}^{part}(h, \lambda) \quad (4)$$

Depending on the type of lidar (aerosol backscatter, Raman, differential absorption), and hence the type of light interaction with matter used as its functioning principle (Rayleigh, Lorenz-Mie, Raman scattering, absorption) different terms in the definition of α and β coefficients are considered.

Often the lidar equation is used in form of the range corrected signal, obtained by multiplication of the detected signal with the squared range vector, where all terms describing range independent parameters of the lidar system appear in the definition of the lidar instrumental constant $C = P(h_0, \lambda)\xi(\lambda)\Delta hA$, which, at least theoretically, can be calculated for any individual lidar.

$$S(h, \lambda) = P(h, \lambda)h^2 = C\xi(h)\beta(h, \lambda)T^2(h, \lambda) \quad (5)$$

The range dependent term describing the geometrical compression of the system vanishes if the solution of the lidar equation is found for $h \geq h_{min}$, where h_{min} denotes the range after which the recorded signals are free of the geometrical compression and, hence, $\xi(h) = 1$.

The major problem of the inversion of the registered lidar signals is caused by the existence of two unknown (α and β) in one lidar equation, so that no unique solution can be found. The assumptions and estimations made to find the appropriate solution result in an introduction of different types of errors.

4.3 Diverse approaches for the elastic backscatter lidar retrieval

The lidar signal for the aerosol measurements done with detection in the spectral range of the emitted laser wavelength λ can be described with the range corrected backscattered signal mentioned above. By clever choice of the emitted laser wavelength, so that most of the atmospheric constituents do not absorb it and hence the favourable signal strength is obtained even at high altitudes, the term in the molecular extinction coefficient definition due to absorption $\alpha_{abs}^{mol}(h, \lambda) \approx 0$ can be neglected (c.eq. 5). Hence, the backscatter and extinction coefficients split to only two scattering dependent terms; the molecular terms $\beta^{mol}(h, \lambda)$ and $\alpha^{mol}(h, \lambda)$ due to the existence of the gaseous constituents of the atmosphere (Rayleigh scattering) and the particle terms $\beta^{part}(h, \lambda)$ and $\alpha^{part}(h, \lambda)$ due to the existence of aerosols in atmosphere (Lorenz-Mie scattering).

4.3.1 Solution for an aerosol rich homogeneous atmosphere (slope method approach)

In case the atmosphere is rich in aerosol, as for example in the planetary boundary layer (PBL), the contribution of aerosol particles to the measured backscatter and extinction coefficients strongly exceeds the molecular contribution, i.e. $\beta^{mol}(h, \lambda) \ll \beta^{part}(h, \lambda)$ and $\alpha^{mol}(h, \lambda) \ll \alpha^{part}(h, \lambda)$.

By defining the natural logarithm of the range corrected lidar signal as $S(h) = \ln(S(h, \lambda))$ and neglecting the molecular terms in α and β the lidar equation can be rewritten as

$$\frac{d}{dh}S(h) = \frac{1}{\beta^{part}(h)} \frac{d\beta^{part}(h)}{dh} - 2\alpha^{part}(h) \quad (6)$$

An unique solution to this equation does not exist since it suffers still from two unknowns, $\beta^{part}(h, \lambda)$ and $\alpha^{part}(h, \lambda)$. The slope method approach, however, provides a solution based on the assumption that the emitted laser light propagates in the homogeneous atmosphere. In this case changes of the backscatter coefficient in interval dh are negligible ($\frac{d}{dh}\beta^{part}(h) = 0$) and the aerosol extinction coefficient can be calculated.

$$\alpha^{part}(h) = -\frac{1}{2} \frac{d}{dh} S(h) \quad (7)$$

4.3.2 Solution for aerosol rich heterogenous atmosphere (Klett approach)

In heterogenous atmospheres strong gradients of backscatter $\frac{d}{dh}\beta^{part}(h) \neq 0$ can exist. In this case inversion of the lidar equation requires an assumption of a relation between particle extinction and backscatter coefficients, the so called lidar ratio. The lidar ratio function is usually guessed or modelled from the size distribution and chemical composition of particles in the atmosphere.

Generally, it can be provided much easier for a homogeneous air mass with stable aerosol concentrations in a well mixed layer. In such case it can be described by a height independent empirical relation obtained from measurements of backscatter light intensity for different wavelengths at different meteorological visibility conditions $(\alpha^{part}(\lambda))^k = B\beta^{part}(\lambda)$, where size parameter k varies between $0.67 \leq k \leq 1$. For heterogenous atmospheres the propagation of the laser light at different heights strongly depends on the size and type of atmospheric particles and hence both the size parameter and the lidar ratio vary additionally with height. Especially, the application of the vector of height dependent lidar ratio $(\alpha^{part}(\lambda))^k = B(h)\beta^{part}(\lambda)$, even with $k = 1$ provides more accurate retrievals of optical properties.

The natural logarithm of the range corrected lidar signal with assumed constant lidar ratio relation ($B(h) = const$) can be rewritten as follows.

$$\frac{d}{dh} S(h) = \frac{k}{\alpha^{part}(h)} \frac{d\alpha^{part}(h)}{dh} - 2\alpha^{part}(h) \quad (8)$$

The stable solution to this equation can be found only for the backward inversion with assumption of the calibration value far from the lidar. For the range corrected signal at an initial point far from the lidar ($h_m > h$, $S_m = S(h_m)$) the solution can be found in the following form.

$$\alpha^{part}(h) = \frac{\exp(\frac{S(h)-S_m}{k})}{\frac{1}{\alpha^{part}(h_m)} + \frac{2}{k} \int_h^{h_m} \exp(\frac{S(\tilde{h})-S_m}{k}) d\tilde{h}} \quad (9)$$

The stability of the solution is due to the *plus* sign in the denominator in the solution equation (division of terms of values growing with range). Even if an error in the estimation of the calibration value is as large as $\pm 50\%$ after some hundred meters in aerosol rich atmosphere the solution converges to the correct one. For the forward calculation, when the calibration value is chosen near the lidar ($h_0 < h, S_0 = S(h_0)$) the solution becomes numerically unstable due to the *minus* sign in the denominator (division of terms of values decaying with range). The overestimation of the calibration value of only 3% for the unstable solution results in divergence towards infinity, while an underestimation results in convergence to 0. For the retrieval of the zenith aiming ground based lidar, the S_m is usually chosen in the aerosol free tropopause altitude, where the calibration value (integration constant) is mainly due to the well known molecular contribution, what additionally reduces the solution error.

4.3.3 Solution for a heterogenous atmosphere with aerosol rich and aerosol free layers (Klett-Fernald approach)

When the lidar retrieval is done not only in the planetary boundary layer (PBL) but also extended to the free troposphere both particle and molecular terms in the definitions of backscatter and extinction coefficients can be in the same order of magnitude

($\beta^{mol}(h, \lambda) \leq \beta^{part}(h, \lambda)$ and $\alpha^{mol}(h, \lambda) \leq \alpha^{part}(h, \lambda)$) and have to be considered in the lidar equation. For the aerosol free atmosphere during very good visibility conditions, the relationship between molecular extinction and backscatter coefficients can be described as $\alpha^{mol}(h, \lambda) = (8\pi/3)\beta^{mol}(h, \lambda)$. The Rayleigh atmosphere profiles are calculated from height dependent temperature and pressure profiles of the standard atmosphere or provided from nearby performed radiosonde measurements. For aerosol layers the height and wavelength dependent lidar ratio relation $\alpha^{part}(h, \lambda) = B(h, \lambda)\beta^{part}(h, \lambda)$ is used.

The natural logarithm of the range corrected lidar signal states as follows

$$S(h) = \ln C + \ln[\beta^{mol}(h, \lambda) + \beta^{part}(h, \lambda)] - 2 \int_{h_0}^h [\alpha^{mol}(\tilde{h}) + \alpha^{part}(\tilde{h})] d\tilde{h} \quad (10)$$

If $G(h)$ defines the backscatter ratio function, depending on both unknown parameters α^{part} and β^{part} , the last equation can be rewritten accordingly.

$$G(h) = \frac{\beta^{mol}(h) + \beta^{part}(h)}{\beta^{mol}(h)} = 1 + \frac{8\pi\alpha^{part}(h)}{3B(h)\alpha^{mol}(h)} \quad (11)$$

$$S(h) = \ln C + \ln G(h) + \ln \beta^{mol}(h) - 2 \int_{h_0}^h [B(h)\beta^{mol}(h)(G(h) - 1) + (\frac{8\pi}{3}\beta^{mol}(h))] d\tilde{h} \quad (12)$$

By defining functions $F(h)$ and $F(h, \lambda)$ all known and unknown parameters in the equation can be separated respectively

$$F(h) = S(h) - \ln \beta^{mol}(h) - 2 \int_{h_0}^h [B(h)\beta^{mol}(h) - \frac{8\pi}{3}\beta^{mol}(h)] d\tilde{h} \quad (13)$$

$$F(h, \lambda) = \ln C + \ln G(h) - 2 \int_{h_0}^h [B(h)\beta^{mol}(h, \lambda)G(h)] d\tilde{h} \quad (14)$$

Hence, the last equation has an analytical, numerically stable solution for the backward inversion starting at an initial point F_m far from the lidar ($h_m > h$) with the integration constant $\frac{1}{G(h_m)}$ calculated from the backscatter ratio equation in free troposphere.

$$G(h) = \frac{\exp(F(h) - F_m)}{\frac{1}{G(h_m)} + 2 \int_h^{h_m} B(h)\beta^{mol}(h)\exp(F(h) - F_m) d\tilde{h}} \quad (15)$$

$$\alpha^{part}(h_m) = -\frac{1}{2} \left(\frac{dS(h_m)}{dh} - \frac{1}{\beta^{mol}(h_m)} \frac{d\beta^{mol}(h_m)}{dh} \right) - \alpha^{mol}(h_m) \quad (16)$$

Comments on all backscatter lidar solutions discussed above

The slope method can be used only for homogeneously distributed aerosol in the atmosphere, a condition difficult to meet in reality.

The Klett-Fernald solution requires a calibration value (an absolute value of backscatter ratio at the selected calibration range), and is unstable for integrations beyond this calibration range. It requires an input of the lidar ratio (usually not sufficiently known aerosol property) and hence it is not quantitative, especially for the retrieval of the extinction coefficient in a turbid atmosphere. However, since the backward solution is numerically stable and signals are strong, the retrieval is not too sensitive to the noise of the signal. In addition, retrieved backscatter profiles depend only weakly on the assumed lidar ratio. The retrieval errors are depending on the range of the calculated signals, i.e. the longer the integration path, the larger the difference between the assumed and the real lidar ratio (Fernald [105]).

The Klett method is widely used in the lidar community, since single wavelength backscatter lidars are the easiest systems and their data are at least the by-product of any lidar measurement. The approach is especially useful for the calculation of backscatter profiles in relatively clear areas of the atmosphere, as for example in the upper troposphere and stratosphere. Generally, in all of the Klett retrievals, the estimation of pressure and density profiles and the multiple scattering problems add to the systematic error. However, due to very high numbers of molecules in the troposphere their relative fluctuation is very small and hence the influence of wrong pressure and density on retrievals is only small. High optical densities of the aerosols or cloud layers where multiple scattering occurs disables the retrieval.

In contrast to backscatter profiles the extinction coefficient profiles can be provided only as accurate as the lidar ratio was guessed/estimated. The standard lidar evaluation scheme used for all AWI lidars (except the high frequency MALi lidar described by Kaiser [106]) is also partly based on the Klett-Fernald approach. To improve the quality of the retrieval, an additional and independent information on the extinction coefficient is provided with one of described below evaluation schemes, i.e. the Ansmann approach for Raman lidar (Ansmann et al. [96]) or the two-stream evaluation approach for the aerosol backscatter lidar (Kunz [31], Hughes and Paulson [32]).

4.4 Ansmann approach for inelastic backscatter lidar retrieval

In case of Raman measurements, where an inelastic interaction of light and matter is considered, the detection of lidar signals occurs also in a spectral range different from the emitted laser wavelength λ . The inelastic lidar equation for the range corrected backscatter signal can be written as

$$S_R(h, \lambda, \lambda_R) = P(h, \lambda, \lambda_R)h^2 = C_R\beta_R(h, \lambda_R)T_R(h, \lambda, \lambda_R) \quad (17)$$

where λ denotes the emitted wavelength, λ_R the detected Raman wavelength, and $P(h, \lambda, \lambda_R)$ the intensity of the detected Raman signal at a time $t = 2h/c$. The lidar instrumental constant C_R is defined as before but with $\xi_R(\lambda_R)$ as the detector efficiency for the detected Raman wavelength λ_R . The term $\beta_R(h, \lambda_R)$ describes the Raman backscatter coefficient at wavelength λ_R due to air molecules of the well known height dependent atmospheric density function. It is proportional to the cross-section of Raman scattering at 180° on the concentration of N_2 and/or O_2 molecules, i.e. $\beta_R(h, \lambda_R) = \sigma_R^\pi N(h)$. Hence, the only unknown in the Raman lidar equation is the extinction coefficient in the atmospheric transmittance $T_R(h, \lambda, \lambda_R)$ between the lidar and height h .

$$T_R(h, \lambda, \lambda_R) = \exp\left(-\int_{h_0}^h (\alpha(\tilde{h}, \lambda) + \alpha_R(\tilde{h}, \lambda_R)) d\tilde{h}\right) \quad (18)$$

where $\alpha(h, \lambda)$ is the total extinction coefficient due to molecules and particles present at the height h above ground for emitted laser wavelength λ , and $\alpha_R(h, \lambda_R)$, the same for detected Raman wavelength λ_R , which also splits to its molecular and particle terms. Corrections for ozone absorption in the UV spectral range can be made if information on the ozone concentration is provided, for example by ozone sondes. The relationship between particle extinction coefficients at both emitted and detected wavelengths describes the Ångström law, where the Ångström parameter κ is calculated from the model size distribution function. For $\kappa = 4$ this relation describes the relationship between molecular extinction coefficients at both emitted and detected wavelengths according to the Rayleigh law.

$$\alpha^{part}(h, \lambda_R) = \left(\frac{\lambda_R}{\lambda}\right)^{-\kappa} \alpha^{part}(h, \lambda) \quad (19)$$

Due to the existence of only one unknown, the Raman lidar equation can be solved analytically

$$S(h) = -C\sigma_R^\pi N(h) \int_{h_0}^h \left[\left(1 + \left(\frac{\lambda_R}{\lambda}\right)^{-4}\right) \alpha_{mol}(h, \lambda) + \left(1 + \left(\frac{\lambda_R}{\lambda}\right)^{-\kappa}\right) \alpha_{part}(h, \lambda) \right] d\tilde{h} \quad (20)$$

$$\alpha_{part}(h, \lambda) = \left[\frac{d}{dh} (\ln N(h) - \ln S(h)) - \left(1 + \left(\frac{\lambda}{\lambda_R}\right)^4\right) \alpha_{mol}(h, \lambda) \right] \cdot \left[1 + \left(\frac{\lambda}{\lambda_R}\right)^\kappa\right]^{-1} \quad (21)$$

Comments of sources of errors for Raman retrieval

The main source of error in the aerosol extinction coefficient profiles retrieved by Raman method is the signal detection problem and an error introduced by operational procedure (division by noisy profile), i.e. to provide sufficient signal to noise ratio, a long temporal signal averaging during varying atmospheric conditions has to be applied. Additionally, minor systematic errors occur due to an estimation of a wavelength dependent Ångström parameter κ and, for calculations in the UV spectral range, error due to the estimation of the ozone profile.

As for the Klett retrievals, the estimation of pressure and density profiles and multiple scattering add to the systematic error. Still, Raman channels provide independent information on aerosol extinction profiles which can be further used to calculate backscatter profiles without assuming a lidar ratio function. This backscatter profiles can be calculated in two ways, by forcing the ratio of elastic and Raman backscatter signal and calibrating it at a height h_0 for example in tropopause, or by solving directly the backscatter lidar equation for aerosol backscatter with known aerosol extinction from the Raman evaluation and by eliminating the system constant by choosing a calibration value at any height.

The solution, unlike for the Klett inversion, depends only on this estimation/guess, whereby the wrong guess shifts the whole profiles by a constant factor (Ansmann [30]). The standard evaluation scheme of the AWI's KARL lidar applies the Ansmann direct approach and uses the standard Klett-Fernald backward retrieval as a double-check of the results.

4.5 Two-stream approach for elastic backscatter lidar retrieval and estimation of lidar instrumental constants

The two-stream lidar evaluation approach allows retrieval of the extinction and backscatter coefficients for two elastic backscatter lidars sampling simultaneously the same atmosphere in opposite directions (Kunz [31], Hughes and Paulson [32], Cuesta and Flamant [34], Stachlewska et al. [33]). The measuring scheme consists of a ground based lidar measuring in zenith configuration and an nadir aiming airborne/spaceborne lidar overflying it at a height h_f , denoted with K and A, respectively. Assuming that the same air is probed when the airborne lidar overflies the ground based lidar, both systems perceive this same air differently; the ground based system with density decreasing with height and vice versa for the airborne instrument. This ensures mathematically independent information content in both equations.

4.5.1 Retrieval of extinction, backscatter and lidar ratio profiles

In the two-stream approach, besides the two unknown lidar instrumental constants (C_K and C_A), the two lidar equations with two unknowns (α and β) are available.

$$S_K(h) = P_K(h)h^2 = C_K\beta(h)T_{[0,h]}^2(h) \quad (22)$$

$$S_A(h) = P_A(h)(h_f - h)^2 = C_A\beta(h)T_{[h_f,h]}^2(h) \quad (23)$$

By dividing the two last equations, the backscatter coefficients terms are eliminated and an expression for the height dependent extinction coefficient, that does not require any a priori assumption or further calibration and normalisation, can be obtained.

$$\alpha(h) = \frac{1}{4} \cdot \frac{d}{dh} \left(\ln \left(\frac{S_A(h)}{S_K(h)} \right) \right) \quad (24)$$

By dividing the range corrected signals of each equation by itself calculated at a given reference altitude h_{ref} , the following equations are obtained.

$$S_K(h) |_{h_{ref}} = \frac{\beta(h)}{\beta(h_{ref})} \frac{T_{[0,h]}^2(h)}{T_{[0,h_{ref}]}^2(h)} = \frac{\beta(h)}{\beta(h_{ref})} T_{[h_{ref},h]}^2(h) \quad (25)$$

$$S_A(h) |_{h_{ref}} = \frac{\beta(h)}{\beta(h_{ref})} \frac{T_{[h_f,h]}^2(h)}{T_{[h_f,h_{ref}]}^2(h)} = \frac{\beta(h)}{\beta(h_{ref})} T_{[h_{ref},h]}^{-2}(h) \quad (26)$$

The multiplication of these two last equations results in compensation of the transmission terms and provides an expression for the height dependent backscatter coefficient, which does require the knowledge of the value of the backscatter at a reference altitude h_{ref} , that can be obtained from following expression.

$$\beta(h) = \beta(h_{ref}) \sqrt{S_K(h) |_{h_{ref}} S_A(h) |_{h_{ref}}} \quad (27)$$

The expression for $\beta(h_{ref})$ can be obtained by multiplying equation 22 and equation 23 calculated at a given reference altitude h_{ref} .

$$\beta(h_{ref}) = \sqrt{\frac{S_K(h_{ref})S_A(h_{ref})}{C_K C_A T_{[0,h_f]}^2(h)}} \quad (28)$$

To provide backscatter profiles, an estimation of both lidar constants C_K and C_A has to be made. If the constants are not known it is enough if the $\beta(h_{ref})$ is obtained simply as the value of the backscatter coefficient at any reference altitude h_{ref} within the range of the two-stream application. Otherwise, the choice of h_{ref} is free and depends only on the availability of backscatter coefficient values provided by any alternative source of information within this range.

Additionally, if the $\beta^{mol}(h)$ and $\alpha^{mol}(h)$ profiles are obtained by nearby launched radiosonde or theoretically calculated for the standard atmosphere conditions the lidar ratio function can be calculated as a function of altitude.

$$B(h) = \frac{\alpha(h) - \alpha^{mol}(h)}{\beta(h) - \beta^{mol}(h)} \quad (29)$$

In some cases, as for nadir aiming airborne lidars sampling the lowest part of troposphere, it is difficult to provide any β_{ref} value (c.pt. 4.6). In such cases another approach is needed to provide the backscatter profiles from the two-stream method. Assuming that exactly the same air parcels are probed by both lidars when the airborne lidar overflies the ground based lidar implies that there exists only one representative profile of $\alpha(h)$ and $\beta(h)$ for this sampled air. Since the extinction profile can be directly calculated from equation 24, the knowledge of any of the lidar instrumental constants C_K or C_A allows the direct calculation of the backscatter profile from one of the lidar equations 22 or 23, and hence, with known $\alpha(h)$ and $\beta(h)$, the calculation of the remaining lidar constant.

4.5.2 Estimation of lidar instrumental constants

Usually, the lidar constants are not known precisely since their explicit calculation is difficult and suffers from considerable error contributions mainly due to instabilities of the emitted laser energy and transmission of the optical elements, as well as the efficiency of the detection (temperature changes, oscillation of applied voltage).

However, the instrumental constant of the ground based lidar C_K can be accurately estimated by calculating its mean value in the tropopause for various standard Klett inversions performed with several height dependent lidar ratio profiles and several boundary condition values set in the aerosol free tropopause. The parameters for each of the performed standard Klett inversions need to be constrained due to, firstly, the total optical depth $\tau_{layer}(\lambda)$ and $\tau_{layer}^{part}(\lambda)$ the particle optical depth of the layer for which the two-stream total and particle extinctions profiles were obtained; secondly, $\tau_{sun}(\lambda)$ the particle optical depth of the troposphere estimated from simultaneous sunphotometer measurements; and thirdly, by setting $B_{Ci} \approx 12$ the lidar ratio of cirrus clouds (Ansmann et al. [96]) if such cirrus clouds appeared in free troposphere above the layer where the two-stream method was applied. Each of the corresponding β and α profiles obtained with the standard Klett procedure should match to all of constraints mentioned above. In such a way the minimal and maximal realistic values of the lidar ratio in the layer where the two-stream method was applied, the lidar ratio in the free troposphere, as well as the boundary condition β_{ref} in tropopause can be determined. Such set of Klett's β and α solutions determines C_K according to the following expression

$$C_K = \left\langle \left\langle \frac{S_K(i)}{\beta(i) T_{[0,i]}^2} \right\rangle_{(i)} \right\rangle_{(j)} \quad (30)$$

The brackets indicate the mean value, i the height positions in the reference altitude range and j the index of the different Klett solutions. The precise knowledge of $\tau_{layer}(\lambda)$ integrated from the two-stream $\alpha(h)$ profiles improves greatly the precision of this calculations. Of course the calculation can be performed not only in an aerosol free troposphere but in any atmospheric layer which is poor in aerosol particles.

With C_K obtained in this way and with the knowledge of the two-stream α solution also the two-stream β profile can be derived directly from the ground based lidar equation (s.eq. 22). Then the airborne lidar constant C_A can be obtained from the airborne lidar equation (s.eq. 23). The knowledge of the lidar constants allows evaluation of the lidar data, even when a boundary condition β_{ref} cannot be set in an aerosol-free layer or obtained from in-situ measurements.

Comments on retrieval of α and β using two-stream approach

By means of the two-stream algorithm, the availability of two uncalibrated backscatter lidar signals, a reference backscatter coefficient value at any arbitrary altitude and profiles of molecular extinction and backscatter are enough to retrieve $\alpha^{part}(h)$, $\beta^{part}(h)$ and $B(h)$ without ambiguity. Unlike for the Klett inversion, an error of $\beta(h_{ref})$, i.e. the value of the scattering ratio at the reference altitude h_{ref} , causes only a bias on the retrieved backscatter profile. In the case when $\beta(h_{ref})$ is not available, the $\beta(h)$ solution can be calculated directly from the lidar equation if at least one of the lidar instrumental constants C is estimated in any aerosol-free layer.

Errors of the solutions are mainly due to the assumption that both lidars are sampling exactly the same atmosphere, since in reality the retrieval is possible only if the stability of the measured atmospheric layers was greater than the time resolution of the airborne lidar sampling. The error due to noise of the signal for measurements in the lower troposphere with the two-stream method is comparable with the Raman lidar method applied to the

same data. However, half shorter time integrals can be applied to the two-stream retrieval resulting in better representativity of the method (c.cpt. 5.4.3).

4.6 Iterative Klett approach for airborne elastic backscatter lidar retrieval

The main problem of using the standard backward Klett evaluation scheme applied to data obtained with any nadir aiming airborne lidar measuring alone in the lower troposphere arises from the difficulty of providing a calibration values for each of the profiles. For the lowest part of the troposphere, usually rich in turbulent aerosol particles generated by surface winds, the backscatter coefficient is highly variable during the flight and hence very difficult to guess, since the phase function dependence with height has to be accounted for. Similarly difficult is to provide any reference backscatter values in the low troposphere due to the lack of aerosol free layers between the flight altitude and ground/sea level.

One of the ways to provide β_{ref} could be the installation of an in-situ calibration instrumentation onboard the aircraft and the assumption that the measured β_{ref} values are representative for the whole range between the flight altitude h_f and the complete overlap of the lidar. In such case at some points during the flight even measurements of extinction coefficient profiles and humidity profiles are possible if aircraft's descents are performed. However, also in such cases the lidar remote measurements and the in-situ measured profiles do not cover the same area. Furthermore, the aircraft itself greatly disturbs the measured atmosphere.

Another, more intricate way to provide the calibration value can be achieved by the construction of a lidar with scanning laser beam option. In this way not only measurements in a nadir configuration but also in zenith or horizontal configuration can be performed. If a flip of the laser beam between the measurements in a nadir and a zenith configuration are possible, the calibration value can be set in the aerosol free tropopause and both lidar signals can be glued at the flight altitude. However, such combination of the profiles would result in some problems with the overlap range of the lidar, which in such case would be twice as large. If the horizontal scan is available, the calibration value can be obtained using the slope method approach in cases when the atmospheric homogeneity assumption for the layer of air at the flight altitude can be made. Such calibration would have to be made only once during each flight since it would allow direct calculation of the C_A . Still, realisation of these options can be tricky in a real life, i.e. costly (additional in-situ instrumentation, installation of the laser beam flipper on a side of the aircraft) and time consuming procedure (limitation of the space and energy consumption in the aircraft, aircraft authorities certification). Hence, an alternative approach is needed.

The knowledge of the airborne lidar constant C_A greatly improves data evaluation for nadir looking airborne lidar operating alone, as for example at any time before and after overflights above the ground based lidar (c.cpt. 5.10 and 5.9.1). If h_f denotes the flight altitude and h_{gc} the altitude directly below the geometrical compression of the airborne lidar, and in case that the geometrical compression is completed after the first few hundred meters from the lidar, the attenuation of the emitted laser light along this path is negligible:

$$T_{[h_f, h_{gc}]} \approx 1 - (h_f - h_{gc}) \cdot \alpha(h_f) \lesssim 1 \quad (31)$$

By neglecting the transmittance term the backscatter at the altitude h_{gc} can be estimated for each time step during the flight as follows

$$\beta(h_{gc}) \gtrsim \frac{S_A(h_{gc})}{C_A} \quad (32)$$

The knowledge of $\beta(h_{gc})$ for all times during the flight allows application of the standard backward Klett procedure with following constraint: the backscatter coefficient calibration value chosen near the ground β_{ref} must be set in a way, that the β coefficient at the height h_{gc} calculated with the Klett inversion matches the estimated value of $\beta(h_{gc})$. Such calculations can be done with an iterative approach. The clearer the atmosphere and the better α^{mol} is known, the better the transmittance of the layer $[h_f, h_{gc}]$ can be estimated and the error of $\beta(h_{gc})$ decreases. Hence, such an iterative approach provides β profiles which are calibrated during the whole flight and α profiles calculated as precise as the choice of the lidar ratio $B(h)$ (c.cpt. 5.5).

4.7 Direct retrieval of aerosol microphysical parameters

In the traditional elastic lidar evaluation schemes according to Klett [28] and Klett [29] and the inelastic lidar schemes according to Ansmann et al. [96] the lidar constants are redundant due to derivation with respect to height and, hence, their knowledge is not required for the data evaluation. However, the knowledge of the lidar constant opens a new field towards lidar data retrieval, as for example a direct determination of the microphysical properties of aerosol particles from the range corrected lidar signal.

Usually the microphysical aerosol parameter codes require a set of wavelength dependent particle extinction coefficients, particle backscatter coefficients, and depolarisation ratio derived from multiwavelength Raman aerosol lidar and representative for layers where the aerosol microphysics is going to be retrieved (Müller et al. [86], Böckmann [87], Veselovskii et al. [88]). The mathematical model relating the optical and physical particle parameters consists of two Fredholm system of integral equation of the first kind for the backscatter and extinction coefficients (Böckmann et al. [27])

$$\beta(h, \lambda) = \int_{r_a}^{r_b} K_{back}^n(r, \lambda, m, s)n(r, h)dr \quad (33)$$

$$\alpha(h, \lambda) = \int_{r_a}^{r_b} K_{ext}^n(r, \lambda, m, s)n(r, h)dr \quad (34)$$

where r denotes the particle radius, m the complex refractive index, s the shape of the particles, $[r_a, r_b]$ is the range of realistic particle radii, $n(r, h)$ is the particle number distribution, and $K_{back}^n(r, \lambda, m, s)$ and $K_{ext}^n(r, \lambda, m, s)$ are the backscatter and extinction number kernels reflecting shape, size and material composition of particles. Since the inversion of the microphysical parameters is mathematically an ill-posed problem (Bronsztejn and Siemiendiajew [94]), due to the unstability of the retrieved solution, its solution greatly depends on accuracy of input parameters and the various regularisation technique for noise filtering has to be applied.

To calculate the microphysical parameters characteristic for a particular aerosol layer usually the set of three β , two α obtained from the multiwavelength lidar and depolarisation information are applied into both equations 33 and 34 (Böckmann et al. [107]). Such profiles derived from lidar signals suffer from the error related to the noise of the measured signals and the error of the methodology applied for the particle backscatter and extinction retrieval (statistical errors due to the procedure itself and systematic errors due to subjective analysis of the evaluator). This last error source can be principally avoided, i.e. if the lidar constant C is known, the direct application of the equations 33 and 34 into the range corrected lidar signal equation 1 can be performed. Hence, the error of the aerosol microphysics retrieval with this way will be mainly due to the noise of the measured lidar signals, the precision of the lidar instrumental constant and the application of the particular regularisation scheme.

5 Lidar data analysis and applications

This chapter presents the main results of the analysis methodology in sections 5.2 to 5.5 and the application of the lidar data obtained during the ASTAR 2004 and SVALEX 2005 campaigns in the concluding sections.

As an introduction, however, the section 5.1 overviews the meteorological situations during the airborne observations by means of ECMWF operational analyses, satellite imagery and long-range air mass transport.

The results of an intercomparison study between the ground-based AMALi and KARL lidars are presented in chapter 5.2. This study assesses the ability of both systems to obtain the same results. In chapter 5.3 a new methodology to improve the standard evaluation scheme of the KARL's retrieval at the lower altitude is discussed. The feasibility study of the two-stream evaluation method applied to the combination of the airborne AMALi and the ground-based KARL measurements is presented in chapter 5.4. Here, the α^{part} , β^{part} and $B(h)$ retrievals are compared with the corresponding KARL's Raman retrievals. Chapter 5.5 presents and discusses an improved iterative Klett's backward inversion method for the airborne lidar applications in terms of the ability to provide calibrated backscatter ratio profiles during the whole flight in case when the calibration value cannot be provided.

The application of the two latter methods greatly contributed to the realisation of the scientific goals of both campaigns. Additionally, the meteorological events of similar characteristics allowed clear-sky observations under clean and polluted (Arctic Haze) conditions during ASTAR 2004 and SVALEX 2005, respectively. During both campaigns periods of steady east or south-eastwinds passing over Svalbards mountains generated a Foehn-like cloud gap allowing the lidar observations on the leeward side. The comparison of the observations during both episodes is presented in chapter 5.6. The results of the temporal evolution of Arctic Haze during one airborne lidar measurements during SVALEX 2005 is provided in chapter 5.7. The discussion of the origin of the humid layers occurring over Ny-Ålesund during both campaigns is given in chapter 5.8. The temporal and spatial variability of the marine boundary layer during the Foehn-like event of ASTAR 2004 and its interpretation in terms of the aerosol load origin simulated with a numerical model is presented in chapter 5.9. Finally, a study of microphysical and optical properties of the mixed-phase clouds obtained with the alternated airborne in-situ and remote-sensing measurements is presented in chapter 5.10.

5.1 Meteorological situation during the ASTAR 2004 and SVALEX 2005 campaigns

The measurements during ASTAR 2004 and SVALEX 2005 were taken under similar clear-sky weather conditions during distinct meteorological events lasting from 18-23 May 2004 and from 12-16 April 2005, respectively. These distinct meteorological episodes can be denoted as Foehn-like events (Weischet [108]). Prevailing, nearly stationary easterly or south-easterly tropospheric winds past Svalbard formed a cloud-free area due to the adiabatic warming of the descending air parcels on the leeward side of the mountains. Furthermore, and in contrast to the Alpine Foehn events, the flow around the Svalbard archipelago formed so-called corner-winds at the northern and southern tip of the islands.

5.1.1 MODIS imagery

MODIS satellite imagery, as shown in figure 11, illustrates the similarity and differences of both events clearly: west of Svalbard the cloud-free gaps with increased Land Surface Temperature (LST) extend about half of the width of Svalbard ($\approx 250 \text{ km}$) downstream

during both campaigns. Whereas during ASTAR 2004 a corner-wind at the northern tip (see the downstream propagation of the warm anomaly) developed, the SVALEX 2005 event was characterized by an additional broad cloud-free area between the northern tip of Svalbard and the ice edge.

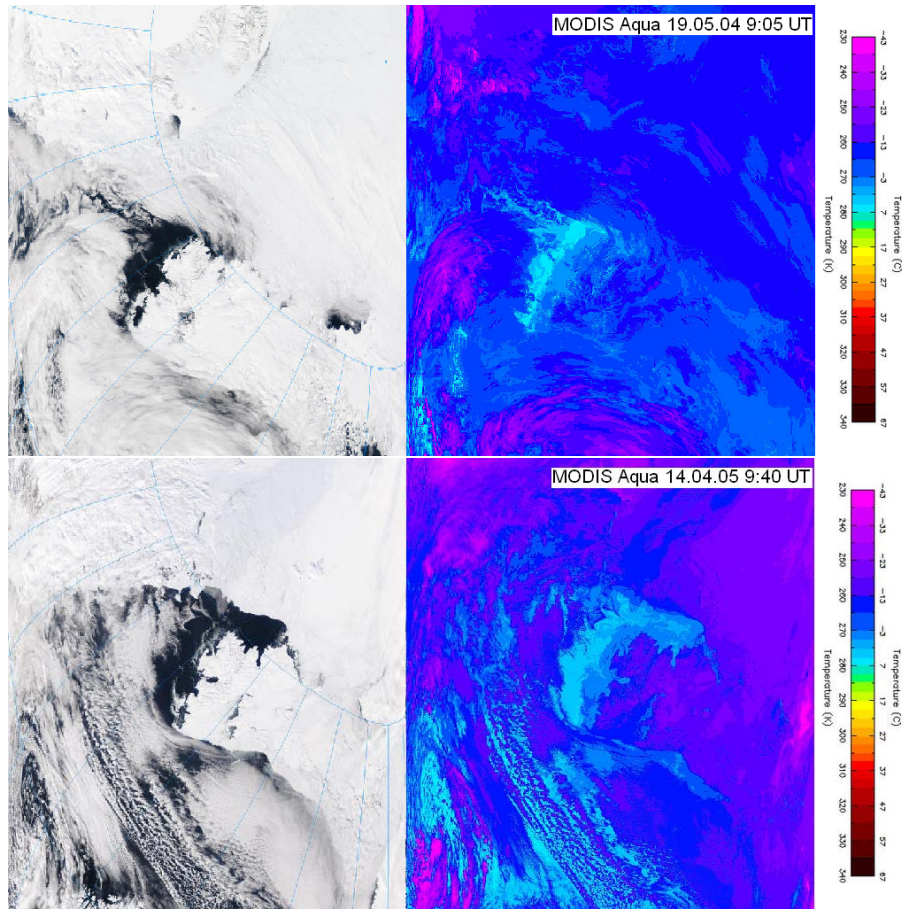


Figure 11: *MODIS satellite imagery of the 1-4-3 bands (true color, left panel) and the LST channels (land surface temperature, right panel) valid on 19.05.2004 at 9:05 UTC and on 14 April 2005 at 9:40 UTC. The characteristic temperature differences between the warm cloud gap area varying from -3°C to -7°C and the cold surrounding varying from -45°C to -10°C . Source: <http://rapidfire.sci.gsfc.nasa.gov>*

5.1.2 ECMWF operational analysis

Operational T511/L60 ECMWF analyses of the near-surface flow fields shown on figure 12 explain the causes for the distinct meteorological situations.

During ASTAR 2004 a low pressure system was slowly propagating parallel to the Scandinavian mountain range north-eastward in a period of two days before 19 May 2004. On 19 May 2004 at 12:00 UTC the center of the low was located directly above Northern Scandinavia. Above the Norwegian Sea and Svalbard, the almost parallel easterly wind throughout the lower troposphere was nearly uniform with a magnitude of $V_H \approx 8 \text{ m s}^{-1}$. Given a maximum buoyancy frequency of $N = 0.010 \text{ s}^{-1}$ (inspection of the ECMWF analyses gave locally smaller values of 0.005 s^{-1} upstream of Svalbard), the Froude number is $\mathcal{F} = V_H / (N h_0) \approx 0.55 \dots 1.6$, where h_0 is the maximum height of the orography. The square of this dimensionless number can be interpreted as ratio of the kinetic energy of

an air parcel upstream of the obstacle to the potential energy it would gain when lifted to h_0 . For $\mathcal{F} < 1$ the parcels flow predominantly around the obstacle whereas for $\mathcal{F} > 1$ the flow has enough energy to pass over the mountains. Thus, the range of calculated Froude numbers \mathcal{F} for $h_0 = 500 \dots 1500 \text{ m}$ explains a partial flow around and above Svalbard during ASTAR 2004.

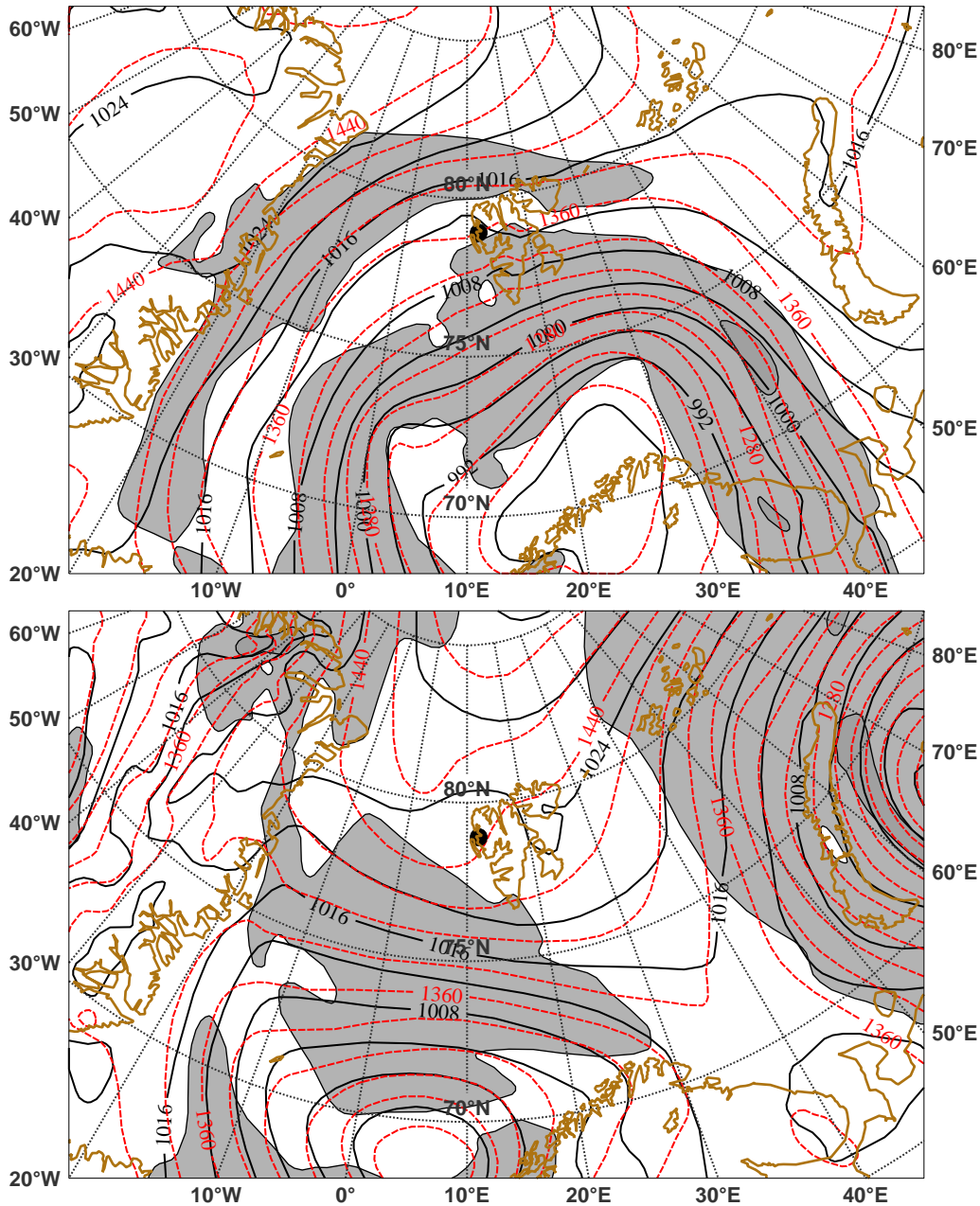


Figure 12: Mean sea level pressure (hPa; solid black lines), geopotential height (m; red dashed lines) and horizontal wind speed $> 10 \text{ ms}^{-1}$ (ms^{-1} , shaded, contour interval 10 ms^{-1}) at 850 hPa valid on 19 May 2004 12:00 UTC (top) and on 14 April 2005 12:00 UTC (bottom). Source: T511/L60 ECMWF operational analyses. Provided by Dr A. Dörnbrack (DLR-IPA, Germany).

The synoptic situation around Svalbard was quite similar for the Foehn-like period during the SVALEX 2005 campaign: the position of the core of the low pressure system

was shifted towards west. Thus, the high wind speed region between the low and the high pressure system was displaced south of Svalbard in accordance with the straight cloud streets visible in the MODIS satellite imagery on that day (c.fig. 11). Again, the magnitude of the horizontal wind speed was less than 10 ms^{-1} resulting in a similar situation for the flow above and around Spitsbergen, i.e. a nearly equal Froude number.

5.1.3 Radiosonde observations

The vertical profiles of the relative humidity (RH), temperature (T) and horizontal wind (V_H) during ASTAR 2004 display the temporal evolution of the Foehn-like event (c.fig. 13).

The profiles indicate a development from the unstable situation with strong fluctuations and inversions in the boundary layer (red profile) into the stable situation with well mixed boundary layer and weak inversions (green profile) during the ASTAR Foehn-like event. The opposite is observed for the SVALEX event (blue and black profiles).

Whereas the profiles on 15 May 2004 show a strong capping inversion at about 1200 m altitude separating the humid air in the boundary layer from much drier air in the free troposphere, the RH profile of the 19 May 2004 is more uniform vertically. This is confirmed by the elevated capping inversion at 1800 m altitude.

The very opposite temporal evolution from a higher mixed state in the boundary layer to a more stable state with a pronounced capping inversion at about 1000 m altitude have been observed during SVALEX 2005. This is in accord with the ceasing winds above Svalbard after 14 April 2005 and the formation of a surface inversion in the lowest 200 m, typical for the high-pressure conditions, which followed the event.

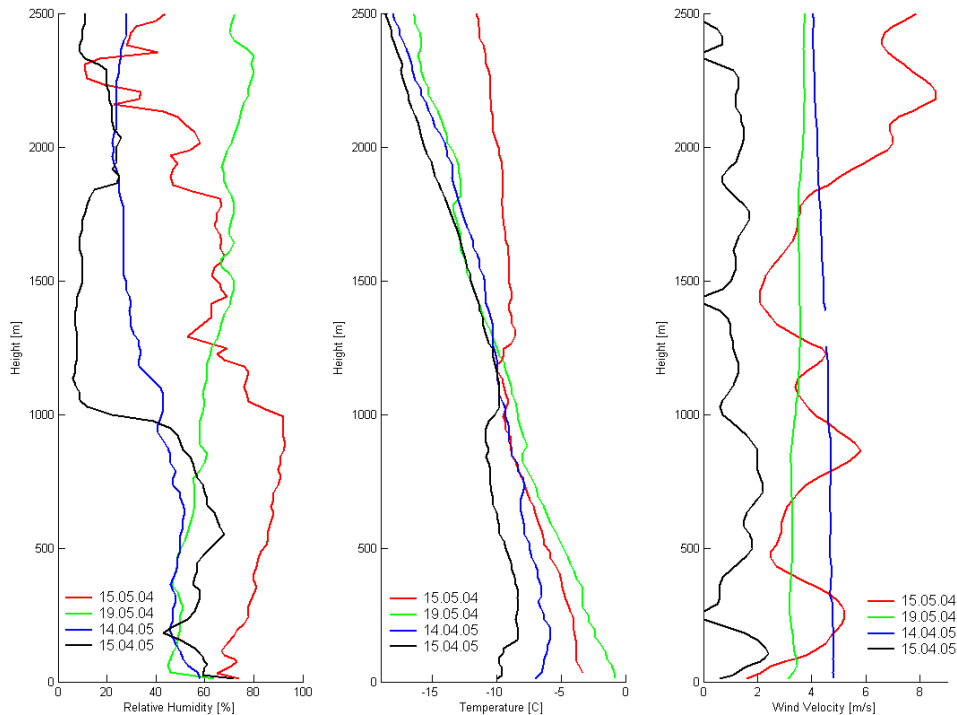


Figure 13: *Relative humidity, temperature and horizontal wind profiles obtained with the radiosonde on 15 May 2004 and 19 May 2004 (ASTAR) and on 14 April 2005 and 15 April 2005 (SVALEX). The radiosonde data were provided by A. Herber (AWI Bremerhaven, Germany).*

5.1.4 NOAA HYSPLIT trajectories

Additionally to the ECMWF operational analyses, isobaric backward trajectories were calculated with the publically available NOAA HYbrid Single-Particle Lagrangian Integrated Trajectory (HYSPLIT) Model (<http://www.arl.noaa.gov/ready/hysplit.html>; see Draxler and Rolph [72]) to analyse the long-range horizontal transport associated with the individual situations.

Generally, during most days of the ASTAR 2004 campaign, the NOAA HYSPLIT backward trajectories show the sampled air remained trapped at lower tropospheric layers in the high Arctic. The trajectories released in Ny-Ålesund at 10:00 UT on 15 May 2004 are characteristic for the period before the Foehn-like event during ASTAR 2004. The air parcels remained isolated in the Arctic for at least 5 days at every given level below 1800 m altitude, i.e. there is no indication of anthropogenic pollution mixed in from lower latitudes (c.fig. 14).

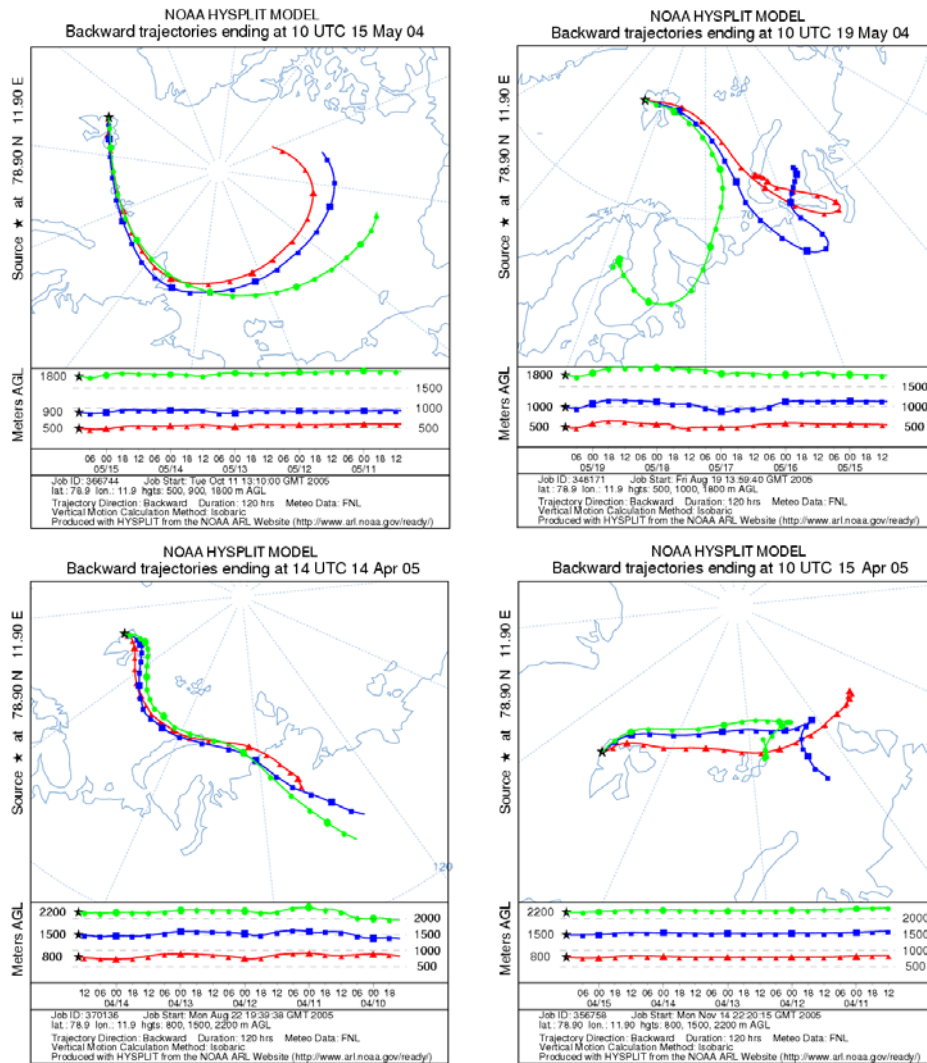


Figure 14: NOAA HYSPLIT backward trajectories obtained for parcels released at 10:00 UTC on 15 May 2004 (left top) and 19 May 2004 (right top) for the ASTAR 2004 campaign, and at 14:00 UTC on 14 April 2005 (left bottom) and 12:00 UTC on 15 April 2005 (right bottom) for the SVALEX 2005 campaign. The different color mark different release heights.

In contrary, the backward trajectories calculated for air parcels released at the same time and location for 19 May 2004 passed shortly through non-polar regions (c.fig. 14). The air at altitudes of 500 *m* and 1000 *m* streaked the north-western part of the West Siberian Plain, an industrially active area, just to mention coal mining in Vorkuta and Uralsk, gas industry in Novyy Port, Ureugoy and Yomburg, oil industry in Ustbaltyk, Samotlor and Ukhta. The air at the altitudes around 1800 *m* streaked the coastline of eastern part of Kola Peninsula and passed by Arkhangelsk 3 days prior to its arrival in Ny-Ålesund. However, the non-uniform character of the air mass transport indicates that the pollution (especially soot, which in the European and Russian climate conditions tend to be kept close to the surface) had limited ability to travel long distances.

During SVALEX 2005 the four-day lasting persistent south-easterly wind allowed transport of air masses from Siberia through the Svalbard Archipelago to the high Arctic (c.fig. 14). The backward trajectories calculated for air parcels released at Ny-Ålesund on 14 April 2005 at 14:00 UTC show uniform transport at all altitudes directly from the highly (for Siberian standards) inhabited area of the Yenisey Delta between the West Siberian Plains and the Central Siberian Plateau. There, black carbon or soot can be generated from traffic, industrial pollution, outdoor fires and household burning of coal and biomass fuels. The soot particles, largely emitted in areas where cooking and heating are done with wood and coal at a low temperatures hindering complete combustion, can be expected as a source of contamination. Afterwards, beginning on 15 April 2005 the weather pattern started to weaken, while a day after it changed favouring winds blowing in exactly opposite direction and bringing altered polluted air back over Svalbard.

5.1.5 FLEXPART long-range pollution transport

The analyses of the air mass origins and long-range transport of pollutants was performed using the Lagrangian particle dispersion model FLEXPART described by Stohl et al.[73], Stohl and Thomson[109] (<http://zardoz.nilu.no/~andreas/flextra+flexpart.html>). The model is based on the ECMWF T511/L60 operational analysis interpolated on an equidistant $1^\circ \times 1^\circ$ latitude/longitude grid. It uses the $1^\circ \times 1^\circ$ degree EDGAR 3.2 1995 inventory data set (<http://www.mnp.nl/edgar/model/>) for *CO*, *NO₂*, *SO₂* emissions and Global PCB data set (<http://www.nilu.no/projects/globalpcb/>) for *PCB-153* emissions.

Basically, for each backward simulation 40.000 particles are released in the volume of the sampled air. The full turbulence and convection parametrization is applied (Seibert and Frank [110]). The results are shown in terms of, so called, retroplume displaying 5-dimensional data (Stohl et al. [111]). Every 24 *h*, particle positions are assigned to one of 5 clusters at which position a circle is drawn (c.fig. 15). The circle's radius represents the number of particles in a cluster, its color indicates the altitude, and the number gives the time backward in days. The trajectory of retroplume's centroid, the time series of its mean altitude with 5 clusters (red circles), and the fraction of particles in the boundary layer and in the stratosphere are given.

The FLEXPART analyses performed for both research flights on 19 May 2004 and 14 April 2005 can be viewed at (<http://zardoz.nilu.no/~andreas/ASTAR/>). The simulations were done for few pre-selected locations along the flight path each 200 *m* between ground and flight altitude at 3000 *m*.

Since the FLEXPART simulations reveal similar results as the NOAA HYSPLIT backward trajectories in terms of the air mass transport, here only results for 1800 *m* altitude for the 14 April 2005 are discussed (c.fig. 15). The retroplume particles were spread incoherently over northern Europe and Asia and between 45°N and 80°N . The highest particle concentrations with generally low (less than 3%) fraction of particles in both, the boundary layer and in the stratosphere, were at the altitudes between 1500-2500 *m* over the north-eastern Asia 5-6 days before their arrival in Ny-Ålesund.

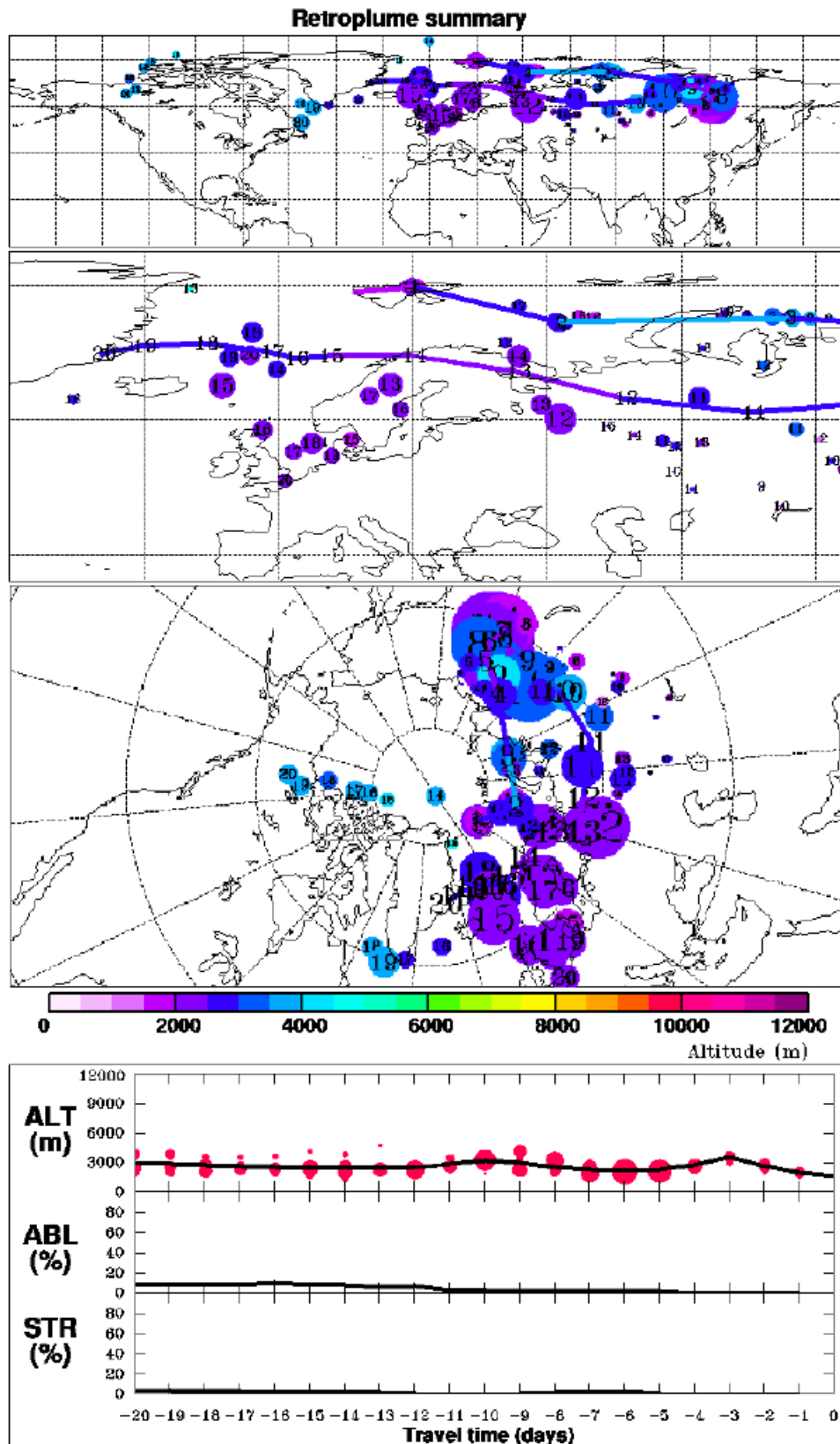
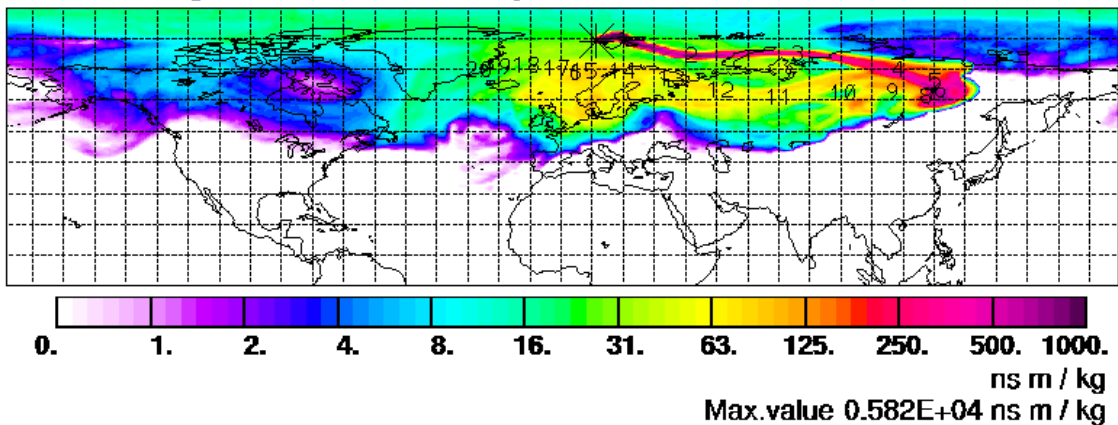


Figure 15: The FLEXPART simulations for particles released between 1600-1800 m altitude at 14:45 on 14 April 2005. The retroplume is displayed globally and in European and polar regions. Provided by Dr A. Stohl (NILU, Norway).

In terms of the anthropogenic pollution transport on the 14 April 2005 particles take-up in over Europe and Asia is likely (c.fig. 16 and 17). The column residence time (c.fig. 16, top) show the air coming from North Sea and northern Europe (10-20 days backward), circling over the Lena Delta in the north-eastern part of Russia (5-8 backward days), and brought back over the Yenisey Delta prior to arrival in Ny-Ålesund. According to the footprint residence time plot (bottom) the anthropogenic pollutions take-up over the southern Scandinavia and central Baltic Sea, and, ever more likely (maximum of 0.16 pskg^{-1}), over the Lena Delta. The CO widely spreads over almost entire Europe and eastern/central Asia with highest values ($0.065 \cdot 10^{-10} \text{ ppbvm}^{-2}$) over the southern part of Great Britain, the north-eastern France and the central/northern Germany. The NO_2 shows high values over the southern part of Great Britain, the Baltic Sea, Denmark, the Netherlands and northern Germany with highest values ($0.031 \cdot 10^{-10} \text{ ppbvm}^{-2}$) over the eastern part of Baltic Sea. Similarly, the SO_2 show highest values ($0.062 \cdot 10^{-10} \text{ ppbvm}^{-2}$) over North-eastern France, southern Germany and also over Czech Republic. The emission sources of $PCB-153$ are widely spread over the whole northern and central Europe, and show high concentrations over the eastern and central Asia as well. The highest values (above $0.5 \cdot 10^{-16} \text{ pptvm}^{-2}$) are over the southern part of Great Britain, France, Germany and peaks around Stockholm, Helisnki, Riga, St.Petersburg, Moscow and Swerdlowsk.

Column-integrated S-R-Relationship



Footprint S-R-Relationship

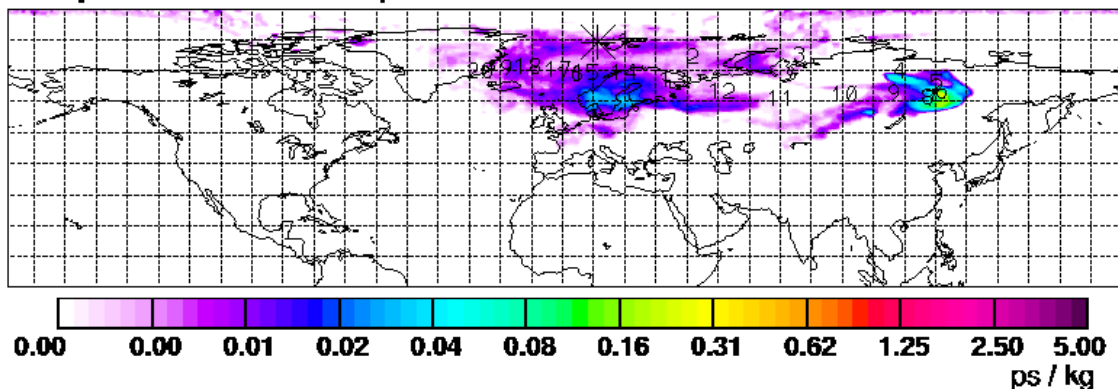
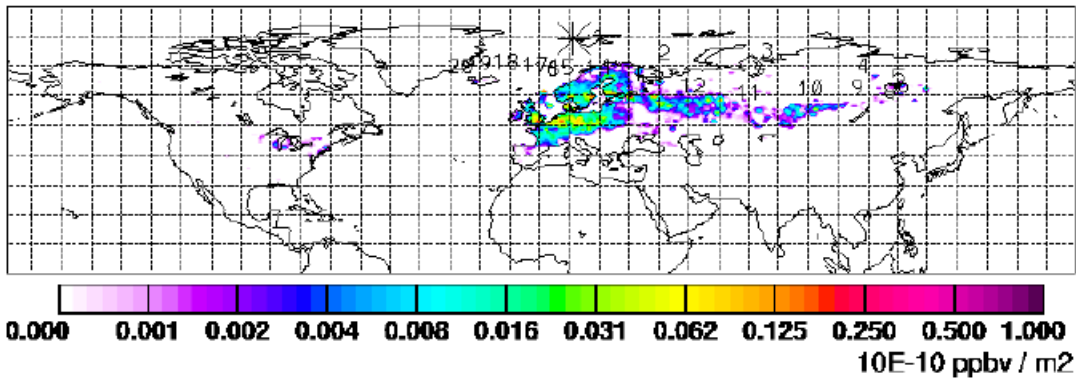
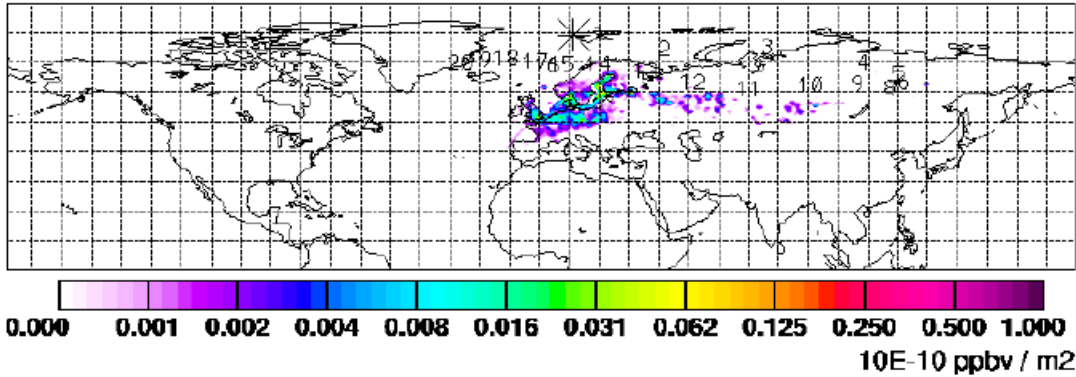


Figure 16: The *FLEXPART* simulations for particles released between 1600-1800 m altitude at 14:45 on 14 April 2005. Globally displayed are the vertically integrated residence time of the particles indicating the air transport from eastern Siberia (top) and the footprint residence time averaged over the lowest 150m indicating the possible anthropogenic pollution take up mainly over Lena Delta and Scandinavia 5-8 days and 14-15 days prior to its arrival in Ny-Ålesund (bottom), respectively. Provided by Dr A. Stohl (NILU, Norway).

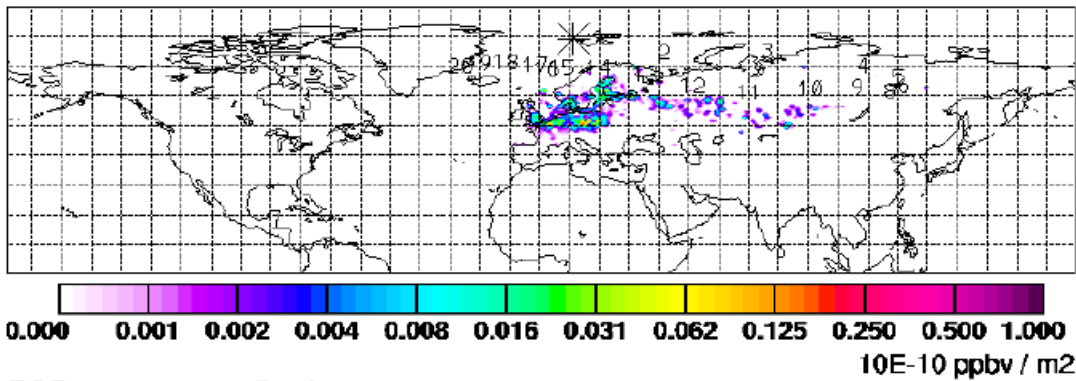
CO source contribution



NO2 source contribution



SO2 source contribution



PCB source contribution

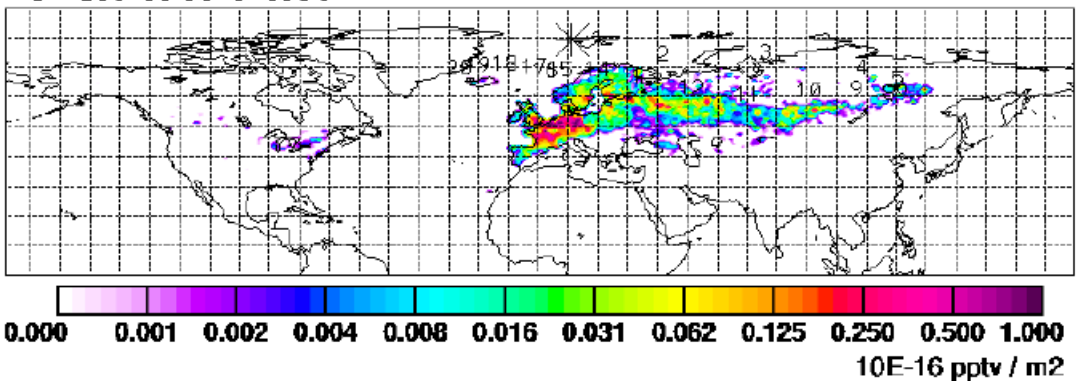


Figure 17: The FLEXPART simulations for particles released between 1600-1800m altitude at 14:45 on 14 April 2005. Globally displayed are the emission contributions of CO, NO₂, SO₂ according to the EDGAR 3.2 1995 inventory and PCB-153 according to the Global PCB data set. Provided by Dr A. Stohl (NILU, Norway).

5.1.6 ECMWF operational analysis for 19 May 2004

To illustrate the Foehn-like situations in more detail, figure 18 depicts characteristic horizontal distributions of meteorological variables near 1000 m altitude for the ASTAR 2004 case. The area of warm air west off Svalbard and colder air surrounding it in the North and over the land with a maximum temperature difference of about 7 K is well captured by the operational T511/L60 ECMWF analyses. Due to the adiabatic cooling of the ascending air, the area east of the largest mountains cools below 260 K associated with increased values of the cloud ice and liquid water content (c.fig. 18 right); during descent the air warms and forms the observed cloud-free gap with negligible values of cloud ice and liquid water content west off Svalbard.

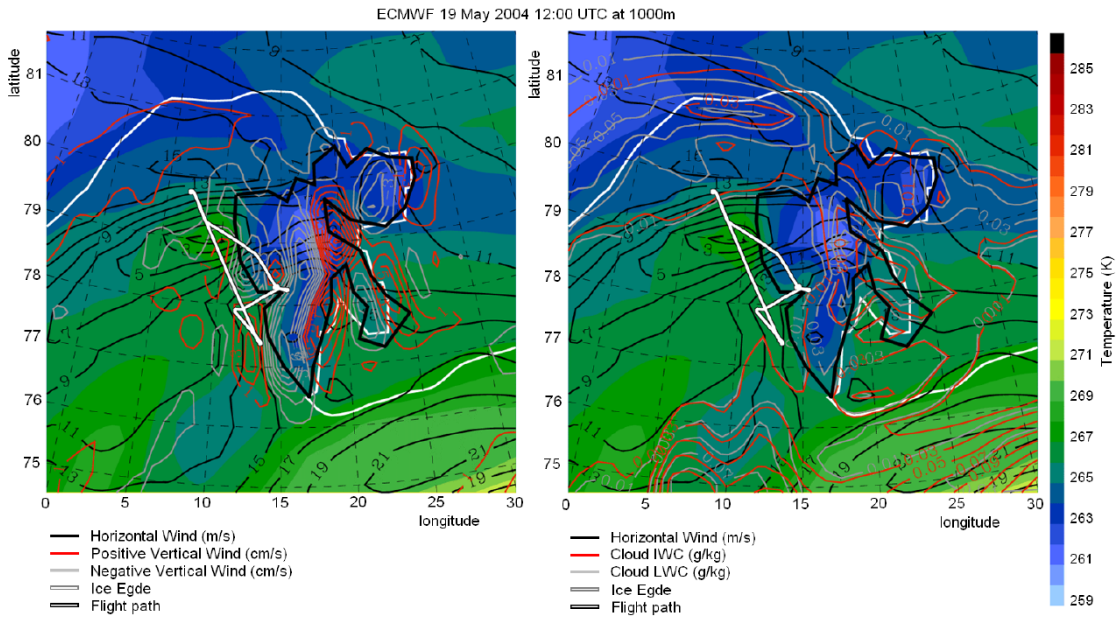


Figure 18: *Horizontal cross-sections of horizontal wind speed (black solid lines; ms^{-1}), temperature (K; color shaded) and left: vertical velocity (red positive, gray negative; cms^{-1}) and on the right: cloud ice water content (red lines; gkg^{-1}) and cloud liquid water content (gray lines; gkg^{-1}) at model level 8 ($\approx 1000m$ altitude) valid on 19 May 2004 12:00 UTC. The white solid lines mark the ice edge and the flight path of Polar 2 on 19 May 2004, respectively. Source: T511/L60 ECWMF operational analyses. Provided by Dr A. Dörnbrack (DLR-IPA, Germany).*

Most remarkably is the formation of a localized jet with $V_H > 15 ms^{-1}$ at the northern tip of Svalbard (Skeie and Grønås [112], Sandvik and Furevik [113]), at around 80°N and 3-9°E, a so-called corner-wind, similar to the tip jets frequently occurring at the southern tip of Greenland (Doyle and Shapiro [114], Moore and Renfrew [115]). Further south in the lee of the mountain at around 79°N and 5-11°E V_H decreases below $2 ms^{-1}$ forming a broad wake region in the warm air. Further south the magnitude of the horizontal wind speed increases again in association with the low pressure system located over Northern Scandinavia. The vertical winds show wave-like structures with periodically changing sinking and rising obviously locked to the underlying orographic obstacles.

Figure 19 juxtaposes the meteorological conditions up- and downstream of Svalbard during the ASTAR 2004 Foehn-like event by means of vertical cross-sections for 30°E and 10°E, respectively. At a longitude of 30°E, the isentropes indicate an inversion layer (layer

of increased thermal stability, i.e. denser contour lines) at about 500 m altitude north of 81°N over the pack ice region. Towards south, the height of this capping inversion increases up to 1000...1500 m altitude; south of 77°N the tilted isentropes mark the baroclinic zone associated with the low pressure system further south. There, the magnitude of the horizontal wind speed V_H is maximum and amounts to about 22 m s^{-1} . Directly upstream of Svalbard, $V_H \approx 6 \dots 12 \text{ m s}^{-1}$ depending on the altitude. Even the clouds visible in the MODIS satellite imagery (c.fig. 11, left) are analysed by enhanced values of cloud ice and liquid water content upstream of Svalbard. The vertical wind speed at this upstream section is very low without any coherent structures.

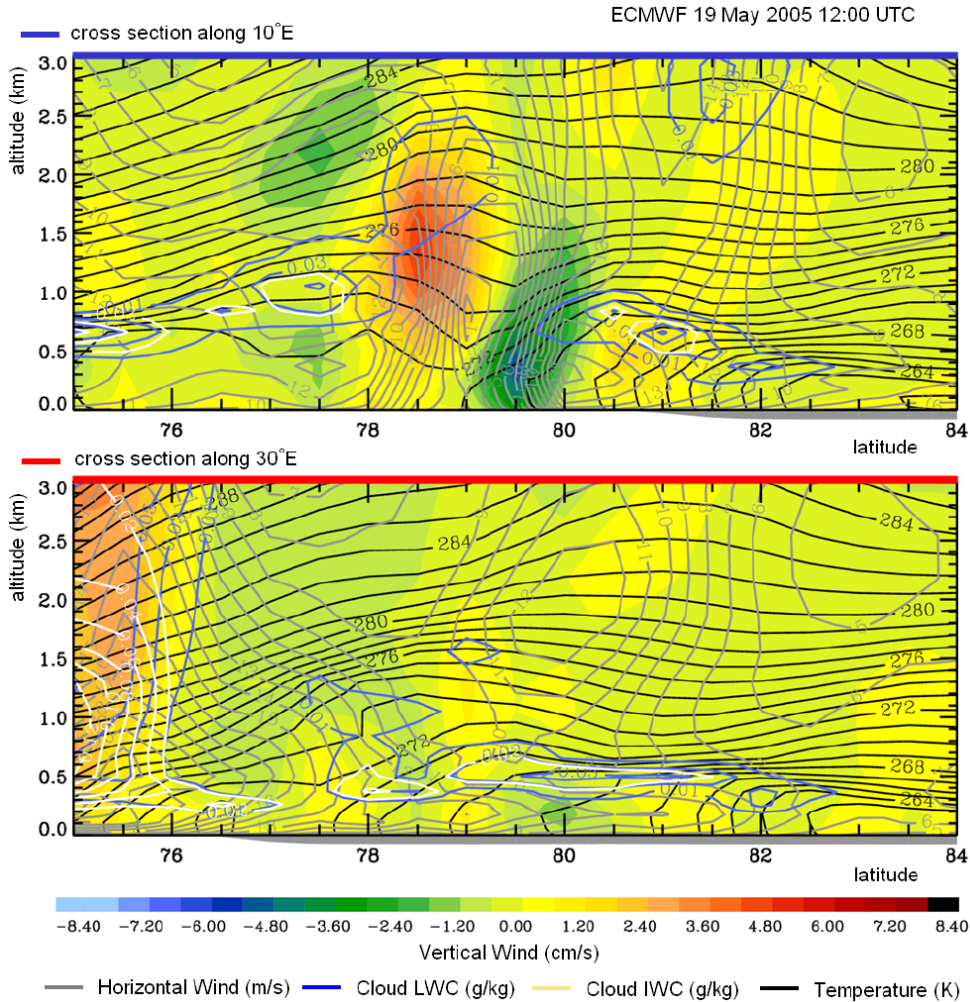


Figure 19: Vertical cross-sections of vertical wind (color shaded; cm s^{-1}), horizontal wind speed (gray solid lines; m s^{-1} , potential temperature (solid black lines; K) and cloud ice water content (white lines; g kg^{-1}) and cloud liquid water content (blue lines; g kg^{-1}) along 10°E (top) and 30°E (bottom) valid on 19 May 2004 at 12:00 UTC. The gray areas below the abscissas mark the locations of the pack ice up- and downstream of Svalbard, respectively. Source: T511/L60 ECMWF operational analyses. Provided by Dr A. Dörnbrack (DLR-IPA, Germany).

In contrast, the vertical cross-section drawn downstream at 10°E reveals pronounced up- and downdrafts between 78°N and 81°N. The up- and downdrafts belong to two counter-rotating horizontal vortex tubes with axes pointing into the plane plotted in fig-

ure 19: south of the ice edge, the northern vortex rotates anticlockwise and produces the strong downdraft at about 79°N in concert with its clockwise rotating counterpart further south. Directly north of the downdraft in the center of the northern vortex tube, the horizontal wind speed is maximum ($V_H \approx 16\text{ ms}^{-1}$ at about 400 m altitude) indicating the corner-wind or tip jet as seen in figure 18. It is interesting to note that the isentropic surfaces in the vicinity of the ice edge are lifted significantly due to the upward motion and dropped due to the descending in the vortex. This results in a rather steep slope of isentropic surfaces along the south-north flight pathes of the POLAR 2 on this day, c.fig. 18. Later, we will see that this characteristic shape of the isentropes and the associated vertical transport of aerosols leads to a triangularly-shaped distribution of the lidar backscatter ratio (c.cpt. 5.5).

The T511/L60 ECMWF operational analyses for 19 May 2004 was used as initial conditions for a high-resolution numerical experiment using the non-hydrostatic anelastic model EULAG (c.cpt. 5.9.2).

5.1.7 The mixed-phase cloud study of ASTAR 2004

In contrast to the clear-sky weather situations, the ASTAR 2004 measurements for the low tropospheric mixed-phase clouds investigations were usually taken during periods of partly clear-sky, partly cloudy conditions (c.cpt. 5.10).

These conditions occurred predominantly at the end of the ASTAR 2004 campaign. Observations of mixed-phase clouds containing ice crystals during May/June are rather unlikely at lower latitudes as much higher temperatures generate a pure water clouds in low troposphere. However, the statistic of the meteorological data over Svalbard shows a significant amount of clouds containing ice crystals occurring between April and June (Herber et al. [65]).

The particular study described in chapter 5.10 deals with the observation of the natural feeder-seeder phenomenon with the ice crystals precipitating to supercooled boundary layer stratocumulus clouds.

5.2 Intercomparison of AMALi and KARL lidars operated in the zenith-aiming ground based configuration

For two measurements taken with different lidars, at the same time, in the same way, and with application of the same profile averaging in time and space, their signal statistics can still differ significantly due to differences in the emitted laser power, the sizes of the used receiving telescopes (Matthias et al. [102]). The system intercomparison is crucial to assess their ability to obtain the same results when the same evaluation scheme is applied.

The AMALi and KARL intercomparison measurements were taken for both systems operated simultaneously at 532 nm in a zenith-aiming ground based configuration under typical 'lidar-day' clear-sky weather conditions on 15 June 2004 between 21:30-22:10 UT at the Koldewey Station in Ny-Ålesund. The systems were placed 30 m apart, distant enough to ensure that each lidar's laser beam and telescope field of view will not overlap the other up to the tropopause. In such a configuration KARL's data were recorded up to the tropopause and the AMALi's data up to 7.5 km height.

The lidars were compared with respect to the backscatter ratio profiles retrieved for both lidars using the same evaluation scheme. The backscatter ratio profiles were calculated using the standard Klett-Fernald-Sasano approach (Klett [28], Klett [29], Fernald [105], Sasano et al. [116]). The calculation was done under the assumption of the height independent lidar ratio of 30 srad resulting in a maximum of a backscatter ratio about 1.54 at 500 m above ground. The KARL's profiles were calibrated by setting a boundary condition in the tropopause with backscatter ratio of 1.05. The AMALi profiles were obtained

up to 5.5 km and therefore calibrated at a height between 4.8-5.0 km with a backscatter ratio of 1.06.

In figure 20 the temporal evolution of the backscatter ratio profiles of both lidars obtained on 15 June 2004 between 21:30-22:10 UT (left and middle), as well as the 20 min integrated time intervals comparison at 21:30 UT and 21:50 UT with the profiles calculated for the entire time interval are presented.

The agreement of KARL and AMALi retrievals is very good with deviations less than 3%. Stronger deviations, up to 30%, are seen only at the range below 750 m. There the lower, underestimated KARL's backscatter ratios occur due to the wrong adjustment of the near-range small telescope on that particular day. Generally, the confidence in the KARL's results obtained in the lowest 1.2 km frequently fails due to the difficulty of the assessment whether the proper adjustment of the near-range small telescope was made (Ritter [80]). The existence of an additional measurement providing cross-check values for the Karl's retrieval within the lowest troposphere could greatly improve the confidence in the results. An idea of a method with a potential of such validation using a scanning approach with additional lidar system (AMALi) is presented in chapter 5.3.

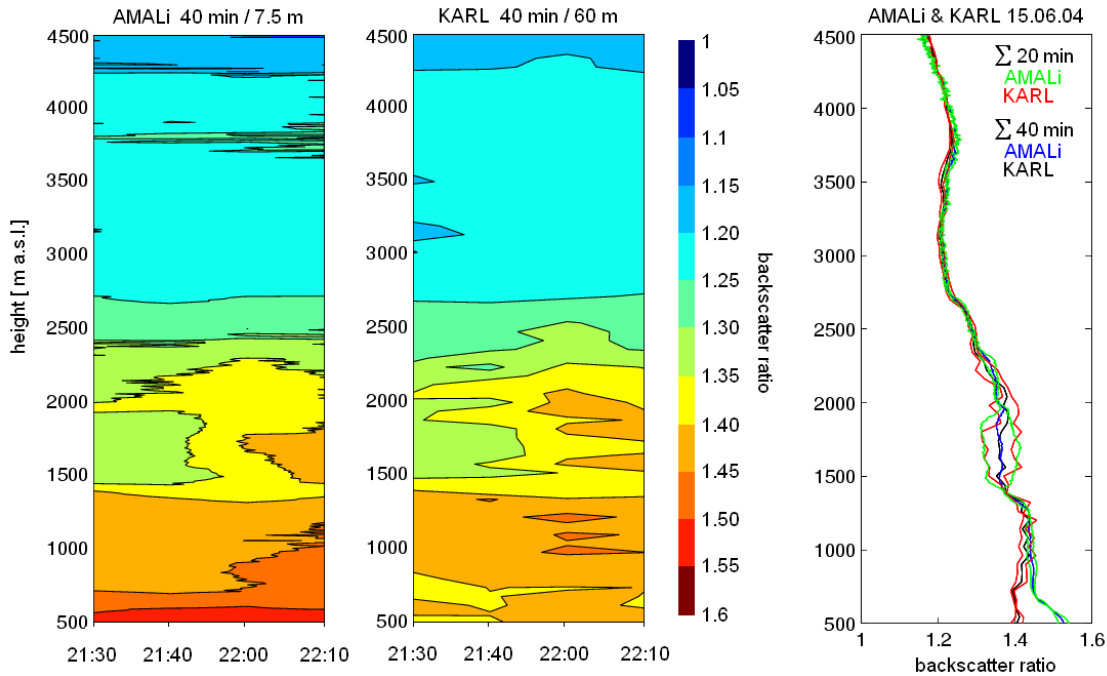


Figure 20: The comparison of the 532nm backscatter ratio profiles retrieved from measurements between 21:30-22:10 UT on 15 June 2004 for AMALi and KARL lidars operated in zenith-looking ground based configuration. Subvisible clouds passing the lidar site between 1.5 - 1.8 km are well captured.

Deviations in the backscatter values at a layer between 1.4 km and 2.4 km altitude are caused by passing thin, subvisible clouds, well captured by both lidars. Already for 20 min integration time both lidar retrievals converge, i.e. deviations in this height interval are mainly due to the high temporal and spatial variability of these clouds. The condensation in this layer must be dominated by small scale processes with a life time of 20 min since the averaging of the lidar signals is just sufficient to smear them out.

Good agreement of the profiles above the mentioned KARL's lower range give evidence that both lidars obtain the same results. Whereby signals noise and/or detection

efficiencies of both instruments are of no concern, giving confidence for the future two-stream evaluation of the data obtained with lidars operated in airborne and groundbased configuration (c.cpt. 5.4).

5.3 Variability of the particle extinction coefficient over the Kongsfjord obtained from the horizontally-aiming ground based AMALi measurements

On the 13.06.04 a one hour horizontal measurement with the AMALi lidar operating in the ground based configuration from the NDSC Koldewey Station building was made to obtain the particle extinction coefficient at 532 nm in the boundary layer over Kongsfjorden. The laser beam was sent at a small inclination angle of $+2.5^\circ$ from a height of 10 m a.g. aiming into the direction of uninhabited area of the Tre Kroner mountain to avoid the potential danger with respect to the eye-safety.

This almost horizontal measurement allowed for the direct retrieval of the particle extinction coefficient under the assumption of a homogeneous aerosol rich atmosphere using the slope method described in the chapter 4.3.1. The 'aerosol rich' atmosphere assumption made usually for the horizontal measurements in the boundary layer at lower latitudes, i.e. $\alpha^{mol} \ll \alpha^{part}$ is not applicable in the case of relatively clear Arctic air. Hence, the extinction values obtained with the slope method have to be corrected for the contribution due to the molecules. For this analysis, the molecular extinction coefficient α^{mol} was calculated for the standard atmosphere with $p_s = 1013,25\text{ hPa}$ and $T_s = 288,15\text{ K}$ resulting in a value of $2 \cdot 10^{-5}\text{ m}^{-1}$.

The slope method applied to a period between 20:00-20:50 on 13.06.04 provided 5 particle extinction coefficients averaged over 10 min at a range between $1150\text{ - }1450\text{ m}$:

Time [UT]	20:00	20:10	20:20	20:30	20:40
$\alpha_{532}^{part} [\text{m}^{-1}]$	$3.29 \cdot 10^{-5}$	$3.12 \cdot 10^{-5}$	$4.45 \cdot 10^{-5}$	$8.94 \cdot 10^{-5}$	$4.63 \cdot 10^{-5}$
$\Delta\alpha_{532}^{part} [\text{m}^{-1}]$	$\pm 0.18 \cdot 10^{-5}$	$\pm 0.26 \cdot 10^{-5}$	$\pm 0.16 \cdot 10^{-5}$	$\pm 0.19 \cdot 10^{-5}$	$\pm 0.26 \cdot 10^{-5}$

These values correspond to a horizontal visibility of $10\text{ - }20\text{ km}$. The mean value of the particle extinction coefficient amounts to $6.3(\pm 0.2) \cdot 10^{-5}\text{ m}^{-1}$, averaged over the whole period of 50 min and in the same range. Within the given errors almost the same value of the particle extinction was obtained during the first 20 min of the measurement. Afterwards, a significant increase of the extinction is recorded. This indicates the short-term variability of the particle optical properties on that particular day.

The knowledge of these extinction values can be of a great help for the correction of the KARL's retrievals suffering from the high uncertainty in the lowest 1.2 km (c.cpt. 5.2).

In addition to the KARL's measurements of particle extinction coefficient, the sun-photometer measurements of the optical depth of the whole atmosphere taken from the NDSC Koldewey Station building, as well as the in-situ measurements of the particle extinction at the Zeppelin Mountain Station located about 1 km south of the NDSC building at about 500 m altitude were available. Since these measurements are not directly comparable another approach for the KARL's validation is required.

From the AMALi particle extinction coefficients obtained with the slope approach the particle backscatter coefficients can be calculated by applying the same lidar ratio value that was used for KARL's particle backscatter coefficient profiles retrieved for each 10 min period. Hence, the values obtained with both lidars can be directly compared and the KARL's profile can be corrected to match the AMALi validation values. Unfortunately, the simultaneous vertical measurements with KARL on that day were not possible due to the occurrence of thick clouds at about 1.9 km altitude.

However, the idea of applying a small scanning lidar for validating the KARL's retrievals shall be used in the future, i.e. the combination with the AMALi's scanning measurements taken from the Zeppelin Station with the laser beam sent every 60 s at one of the 3 angles of $\pm 20^\circ$ and 0° providing (after slope inversion) for each time step 3 particle extinction coefficients values at approximately 160 m, 500 m and 860 m and at the range between 1100-1500 m off the lidar. The values obtained at the two higher altitudes will be used for the validation of the KARL's profiles, and the value at the lowest altitude for the interpolation of the KARL's profiles down to the ground. Additionally, these measurements will allow the study of the extinction variability over the Kongsfjorden, also in the case when thick clouds above 1000 m disable the KARL's observations.

5.4 The two-stream inversion of the airborne nadir-aiming AMALi and zenith-aiming ground based KARL data

In this chapter the successful and, to my knowledge, first-ever application of the two-stream backscatter lidar evaluation method to the non-simulated, real nadir-aiming airborne and zenith-aiming ground based lidar signals is presented (Stachlewska et al. [33]).

The two-stream algorithm is revised, expanded and applied to data obtained during simultaneous measurements taken with a nadir-aiming AMALi, integrated onboard AWI research aircraft Polar 2, overflying a zenith-aiming KARL based in Ny-Ålesund on Svalbard during ASTAR and SVALEX campaigns. The feasibility of the two-stream method to retrieve extinction and backscatter coefficients profiles without assumption of their proportionality is demonstrated. The estimation of lidar constants is given in chapter 5.4.1. The comparison of the two-stream and Raman retrievals is presented in chapter 5.4.3. This proves the greater sensitivity and underlines the potential of the two-stream approach for spaceborne lidar data evaluation and validation during future ASTAR campaigns.

5.4.1 Estimation of the AMALi and KARL instrumental constants

The extinction coefficient profiles in the two-stream approach can be obtained directly without any a priori assumptions from the background and range corrected AMALi and KARL signals. However, to derive the backscatter coefficient profiles directly from the two-stream approach the instrumental constants have to be obtained first (c.pt. 4.5.1). The method for the determination of the constants of ground based C_K and airborne C_A lidars, in case when one of the lidars observes an aerosol poor layer, as for example in the free-troposphere, was proposed in chapter 4.5.2. Using this approach the KARL instrumental constant C_K was calculated from the β and α retrieved with Klett-Fernald's elastic KARL algorithm according to the constraints given in chapter 4.3.3.

Depending on assumed $B(h)$ between the ground and the tropopause or the bottom of Cirrus clouds at about 8-9 km and selected boundary condition $\beta(h_r)$ at the calibration interval between 10-12 km an integration towards the aircraft's flight level accumulates to at least 20% uncertainty of $\beta^{part}(h_f)$. Different combinations of $B(h)$ and $\beta(h_r)$ alter the value of C_K significantly less than the value of $\beta^{part}(h_f)$ diminishing this uncertainty by almost a factor of 4 if the mean of C_K is calculated in the tropopause according to equation (30). For the data of 15 May 2004 best agreement of the optical depth obtained from the Klett-Fernald's elastic KARL retrieval with both τ_{layer}^{part} and τ_{sun}^{part} was obtained for a boundary condition of $\beta_{ref}^{part} = 0.3 (\pm 0.05) \cdot \beta^{mol}$ resulting in a lidar constant $C_K = 1.65 (\pm 0.1) \cdot 10^{14} mV m^3 srad$ calculated at the mentioned calibration interval. For the same boundary condition $C_K = 2.03 (\pm 0.1) \cdot 10^{14} mV m^3 srad$ was found for the data of 19 May 2004. The 23% deviation in these values is due to the lower laser power caused by higher surrounding temperature on the first day under investigation. The lidar constant for the AMALi instrument was found to be $C_A = 1.43 (\pm 0.1) \cdot 10^{13} mV m^3 srad$.

5.4.2 Calculation constrains and errors of the two-stream AMALi and KARL retrievals

The two-stream calculation constrains

The applicability of the two-stream method depends critically on the constraint that both lidars probe the same air masses. Due to their relative movement AMALi and KARL detected different air masses directly above the Koldewey Station and below the Polar 2 aircraft. Hence, for the two-stream calculations of the β^{part} , α^{part} and $B(h)$ profiles at the heights directly above the lidar and directly below the aircraft more height steps than required by constraints of geometrical compression of each lidar (c.cpt. 3.1 and 3.2.2) were excluded.

The data were pre-selected to obtain as high as possible signal-to-noise ratio of both averaged signals whereby the spatial averaging of AMALi and temporal averaging of KARL's signals are kept as short as possible. Additionally, the clouds screening by interpolation of the signal values between the bottom and the top of the cloud, is applied in case when any low density subvisible clouds were recorded by one of the lidars.

The extinction profiles on both days were derived directly from equation (4) using 532 nm channel lidar signals provided with 60 m range resolution, averaged over 10 min in case of KARL and over 8 min case of AMALi. The Poisson smoothing on 5 elements is applied to the obtained extinction profiles. Both τ_{layer} and τ_{layer}^{part} in the range where the method was applied were calculated from these extinction profiles. The Rayleigh extinction α^{mol} and backscatter β^{mol} profiles were obtained from radiosonde launches at the Koldewey Station. The absorption contribution to the extinction, mostly due to the ozone, shows negligible values at 532 nm in the Arctic troposphere and was for this analysis neglected. Cirrus and subvisible clouds, if detected by KARL in the upper troposphere, were treated with low lidar ratios $B_{Ci} = 12$ for green light (Ansmann [96]).

An information on the particle optical depth of the whole atmosphere τ_{sun}^{part} was obtained from sunphotometer measurements at the Koldewey Station. The zenith looking KARL and the sunphotometer generally probe different air, i.e. sunphotometer measures at 29° elevation above horizon and KARL underestimates retrieved values at the heights below its geometrical compression. Therefore, the τ_{sun}^{part} is used as a rough information when compared with the particle optical depth obtained from the Klett's elastic KARL retrieval. The values of C_K and C_A obtained in chapter 5.4.1 were used for the calculations for each day, respectively.

The two-stream contra the Raman retrievals - error comparison

The two-stream 532 nm β^{part} , α^{part} and $B(h)$ profiles were compared with corresponding profiles derived from the Raman nitrogen KARL's returns using Ansmann's approach (Ansmann [96]). The Raman α profiles were derived from the inelastic scattering lidar equation for 607 nm, while Raman β profiles were calculated from the ratio of 532 nm and 607 nm, both with the boundary condition β_{ref}^{part} derived in chapter 5.4.1 for consistency. The Raman evaluation was performed with a 20 minute integration time, i.e. twice as large as the integration intervals applied for the the two-stream retrieval. Further lowering of the integration time of the Raman retrieval was not possible due to insufficient signal-to-noise ratio of the averaged signals.

The errors of both types of the extinction retrievals depend almost entirely on the noise of the signals. The main problem of the Raman extinction retrieval occurs due to the derivative of the noisy signal with height (Whiteman [117], Rocadenbosch [118]). The calculations of the biases in the particle backscatter and extinction retrievals due to the temperature dependence of the Raman scattering (Whiteman [119]) show negligible values for KARL's nitrogen channel. In the case of two-stream extinction retrieval the error is mainly due to the division of two noisy lidar signals. Hence, for the both types of

retrievals error propagation calculation was necessary.

According to error propagation the uncertainties of extinction coefficient (σ_{ext}) and backscatter coefficient (σ_{bsc}) retrieved with the Raman approach are $\sigma_{ext}^R = 5 \cdot 10^{-5} m^{-1}$ and $\sigma_{bsc}^R = 1 \cdot 10^{-7} m^{-1} srad^{-1}$.

The uncertainty of the two-stream extinction coefficient is $\sigma_{ext}^{TS} = 1 \cdot 10^{-6} m^{-1}$. The error of the two-stream backscatter is proportional to the error of lidar constants, i.e. the 5% imprecision of the C_K results in accuracy of the backscatter coefficient of $\sigma_{bsc}^{TS} = 1.5 \cdot 10^{-7} m^{-1} srad^{-1}$. The noise of lidar signals and error of the determination of extinction hardly affects the backscatter accuracy.

5.4.3 Comparison of the two-stream AMALi and KARL retrieval to the Raman KARL retrieval

The comparison of the retrievals obtained with the two different methods for the data taken on two days during the ASTAR 2004 campaign is discussed below.

For 15 May 2004 data recorded around 10:00 UT in a height layer between 635 m and 2435 m proved analysable. The cloud screening was applied to AMALi data in a layer of 120 m thickness around 1440 m altitude. The two-stream β^{part} , α^{part} and $B(h)$ (solid lines) compared to the corresponding values according to Ansmann's Raman evaluation (dashed lines) are presented in figure 21 (red). The aerosol layer visible in the two-stream α^{part} retrieval with a maximum at 1800 m altitude has its maximum at a 100 m lower altitude in the Raman α^{part} profile. The lower aerosol layer has a maximum at around 900 m altitude for both types of α^{part} retrieval but with higher values in the two-stream profile. The total optical depth calculated for the two-stream layer τ_{layer} sums up to a considerable value of 0.084, where particle optical depth τ_{layer}^{part} is 0.064, mainly due to contribution from both mentioned layers. Otherwise, the background particle extinction coefficient is around $0.15 \cdot 10^{-4} m^{-1}$, the background particle backscatter coefficient around $0.7 \cdot 10^{-6} m^{-1} srad^{-1}$ and a lidar ratio of 20 srad. These values are characteristic for the clean arctic summertime condition.

The profiles retrieved from the data recorded on 19 May 2004 at around 9:35 UT at a height interval between 815 m and 2075 m are shown in figure 21 (black). The cloud screening of AMALi data in a layer of 120 m thickness around 1020 m altitude was necessary. At the altitude of around 1800 m a layer of enhanced extinction and lidar ratio is visible again. Apart from this layer the air appears clean with similar particle extinction background value and lidar ratio as for the previous day and τ_{layer} of 0.035 and τ_{layer}^{part} of 0.02, mainly due to mentioned aerosol layer. For this day even lower values of the background particle backscatter coefficient around $0.3 \cdot 10^{-6} m^{-1} srad^{-1}$ were observed.

The retrievals of the two-stream and the Raman techniques on both days agree well. Given mentioned uncertainties of extinction and backscatter coefficients σ^{TS} and σ^R all retrieved β^{part} , α^{part} and $B(h)$ profiles coincide well, with small deviations only in the layers of highest extinction values. While for 15 May 2004 one might speculate about a slight height shift between the profiles, such a behaviour is not observed on the second day. Therefore, we address these deviations partially to noise, with above given error tolerances, and partially to real variations of the atmosphere during the longer intergration of the Raman-shifted lidar profiles (c.pt. 5.4.2).

For both days layers of enhanced extinction values hardly visible in the backscatter profiles were observed, underlining the necessity to determine backscatter and extinction independently of each other from the lidar measurements (Sasano [116]). The discussion of the physical origin of these layers is given in chapter 5.8.

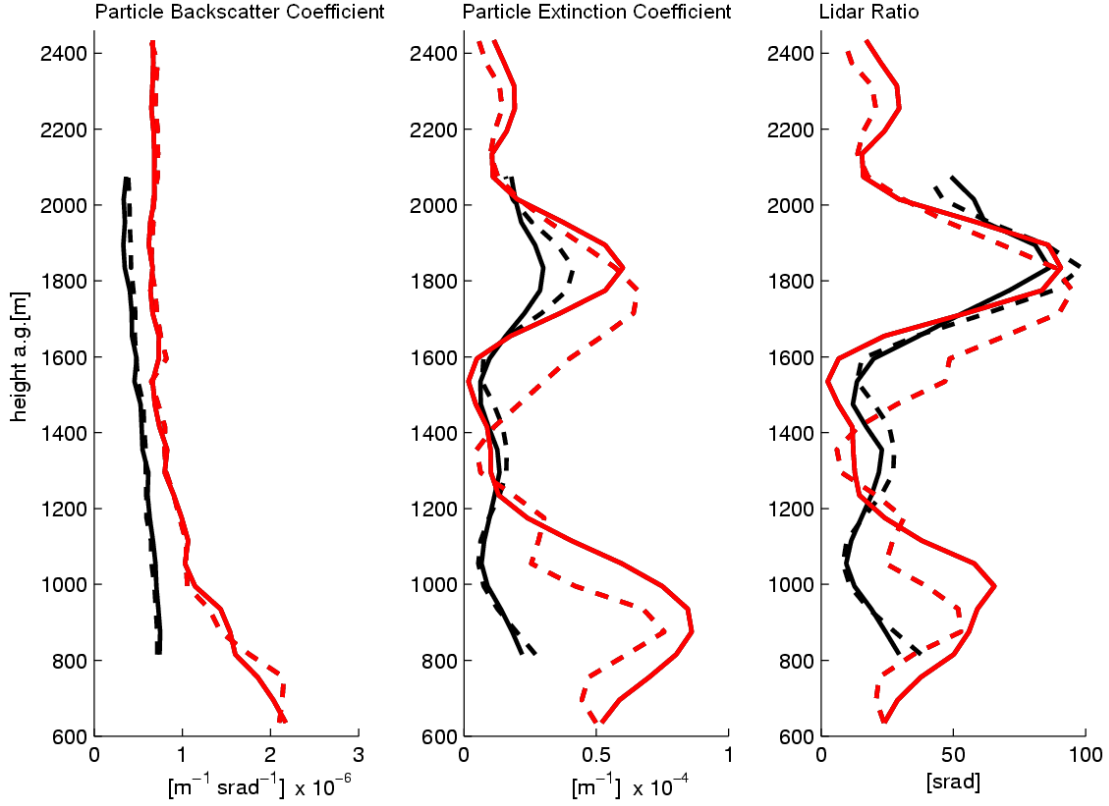


Figure 21: The two-stream 532nm β^{part} , α^{part} and $B(h)$ profiles (solid lines) plotted with corresponding Raman profiles (dashed lines). The red profiles obtained for 10:00 UT on 15 May 2004 and the black profiles obtained for 9:35 UT on 19 May 2004 are identical within the uncertainties given in chapter 5.4.2. The KARL's Raman retrievals were provided by Dr C. Ritter (AWI-Potsdam, Germany).

5.5 The iterative Klett backward algorithm for inversion of the nadir-aiming airborne AMALi lidar data

There are two reasonable ways to proceed with the nadir-aiming airborne lidar data evaluation. Namely, the Klett forward calculation with an initial value at the range intervals close to the lidar $\beta(h_{gc})$ can be performed in the case when the accurate estimation of this value is possible or the Klett backward inversion can be performed if the calibration value far from the lidar, i.e. near ground $\beta(h_{ng})$ is known a priori or can be estimated.

The advantage of the Klett's forward inversion performed with well known value of backscatter at the initial point can be especially valuable for the nadir-aiming airborne lidar measuring in the lower troposphere due to the high signal-to-noise ratio of the obtained signals and due to the increase of aerosol with increase of each range-step as in case of AMALi. In contrary, the standard backward inversion of the nadir-aiming low altitude airborne lidar suffers from the difficulty to estimate the strongly variable aerosol backscatter near ground (Browell [120], Matthey et al. [121]).

In this chapter, an application of another approach for the calculation of calibrated airborne lidar backscatter coefficient profiles during the whole flight is discussed. This approach can be applied in cases when the calibration value cannot be estimated (lack of an aerosol-free layer) or cannot be provided a priori (from an additional onboard in-situ calibration instrumentation, and/or onboard horizontal or vertical scanning of the emitted

lidar light is not available).

The trick to get rid of this calibration problem is, as proposed in chapter 4.6, to estimate accurately the value of backscatter at a range close to the lidar $\beta(h_{gc})$ and to perform the Klett's backward inversion in an iterative way. The calculation of calibrated airborne lidar backscatter ratio profiles is performed in the following steps. Firstly, calculate the particle backscatter value $\beta^{part}(h_{gc})$ close to the aircraft under the assumption that the transmittance term $T = 1$ near the aircraft; secondly, guess the $\beta_{Klett}^{part}(h_{ng})$ near ground and use it as a calibration value for the calculation of the particle backscatter profile using the backward Klett inversion; thirdly, check whether the calculated value of the backscatter at the height close to the aircraft $\beta_{Klett}^{part}(h_f)$ matches the estimated $\beta^{part}(h_{gc})$; if not, change the value of $\beta_{Klett}^{part}(h_{ng})$ accordingly to Newton method, recalculate the $\beta_{Klett}^{part}(h)$ profile and compare both values again; finally, perform such iterations until $\beta_{Klett}^{part}(h_f)$ and $\beta^{part}(h_{gc})$ match.

In this thesis few examples of the application of this iterative approach with respect to the study of the different types of aerosol (c.pt. 5.9.1) or in the case study of the low density mixed-phase clouds (c.pt. 5.10) are discussed. In chapter 5.5.2 an example of such calculations for the airborne AMALi measurements obtained under a clear-sky conditions in the gap area as described in chapter 5.1 is presented.

5.5.1 The discussion of the uncertainties of the iterative airborne inversion

Unlike for the zenith-looking tropospheric lidars (Masumoto and Takeuchi [122]), generally, for the short-range nadir-aiming airborne lidar the largest term of the error propagation of the backscatter coefficient profiles is due to the wrong assumption/estimation of the backscatter calibration value (partial derivative of backscatter over range). The wrong assumption of the lidar ratio contributes much less to the backscatter ratio uncertainty (small partial derivative of backscatter over lidar ratio).

In the case of the approach proposed in this thesis the assumption of the transmittance term $T = 1$ in the airborne lidar equation permits accurate estimation of $\beta(h_{gc})$ in range intervals close to the lidar, i.e. at an altitude near the aircraft but beyond geometrical compression of the lidar (c.pt. 4.6).

In case of the AMALi lidar, for the height chosen just below a geometrical compression of 235 m the expected error for neglecting the transmittance term varies from 0.7% for the particle extinction of $0.15 \cdot 10^{-4} m^{-1}$ typical for clear Arctic atmosphere ($T \approx 0.993$), up to 2.8% for the particle extinction of $0.6 \cdot 10^{-4} m^{-1}$ for aerosol contaminated atmosphere ($T \approx 0.972$). Hence, the clearer the atmosphere and the better the knowledge of the molecular contribution to the extinction α^{mol} (for example from nearby meteorological sounding) the better the transmittance estimate, i.e. the lower uncertainty of the $\beta(h_{gc})$ calculation.

Hence, the accuracy of the α and β calculated with the iterative approach at any time during the flight depends mainly on the assumption of the lidar ratio since the error of the estimation of $\beta(h_{gc})$ near the aircraft (and dependent on it, iteratively found $\beta(h_{ng})$ near ground) hardly affects the error of the backscatter retrieval itself.

5.5.2 The application of the iterative airborne inversion for the calibrated 'along-flight' backscatter coefficient calculation

The lidar backscatter ratio profiles obtained during the whole flight on 19 May 2004 and 21 May 2004 are shown in figure 22. Both flights were performed under similar weather conditions (c.pt 5.1) and show similar values of the retrieved backscatter ratios. Hence, for brevity only results for the first day are discussed in detail in the following. Mind, that the corresponding flight path for that day was sketched in figure 18.

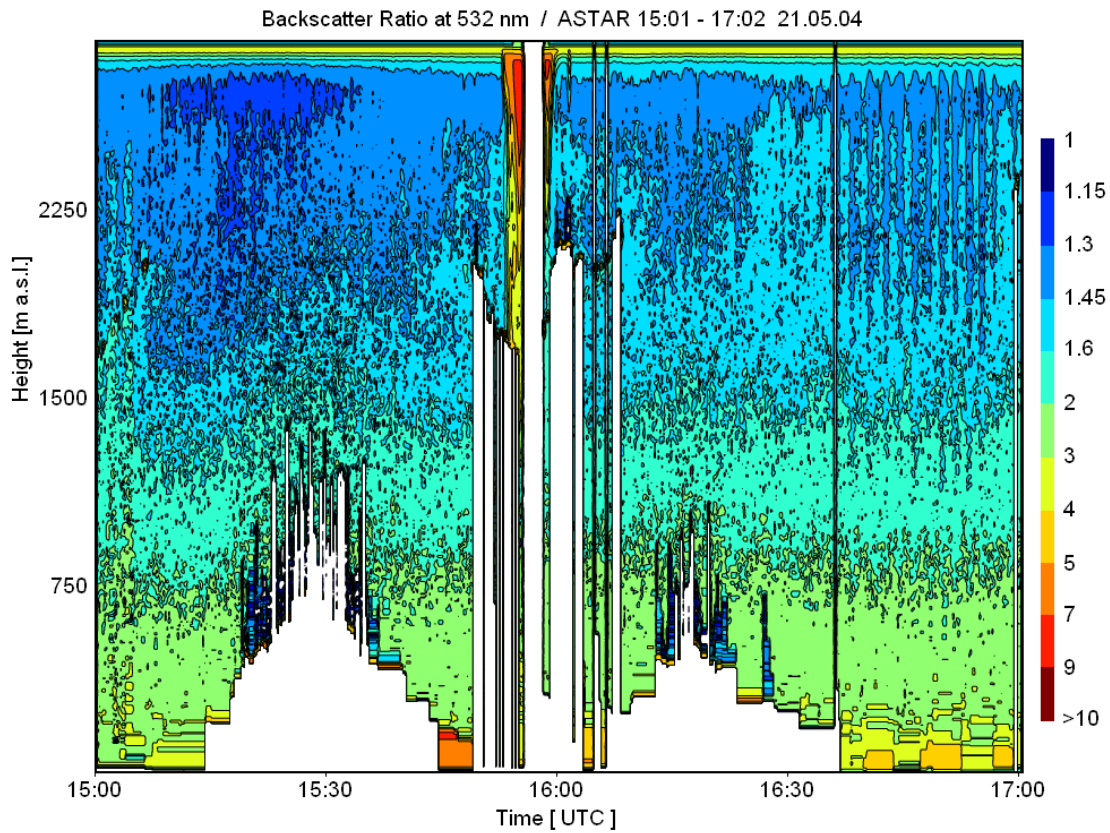
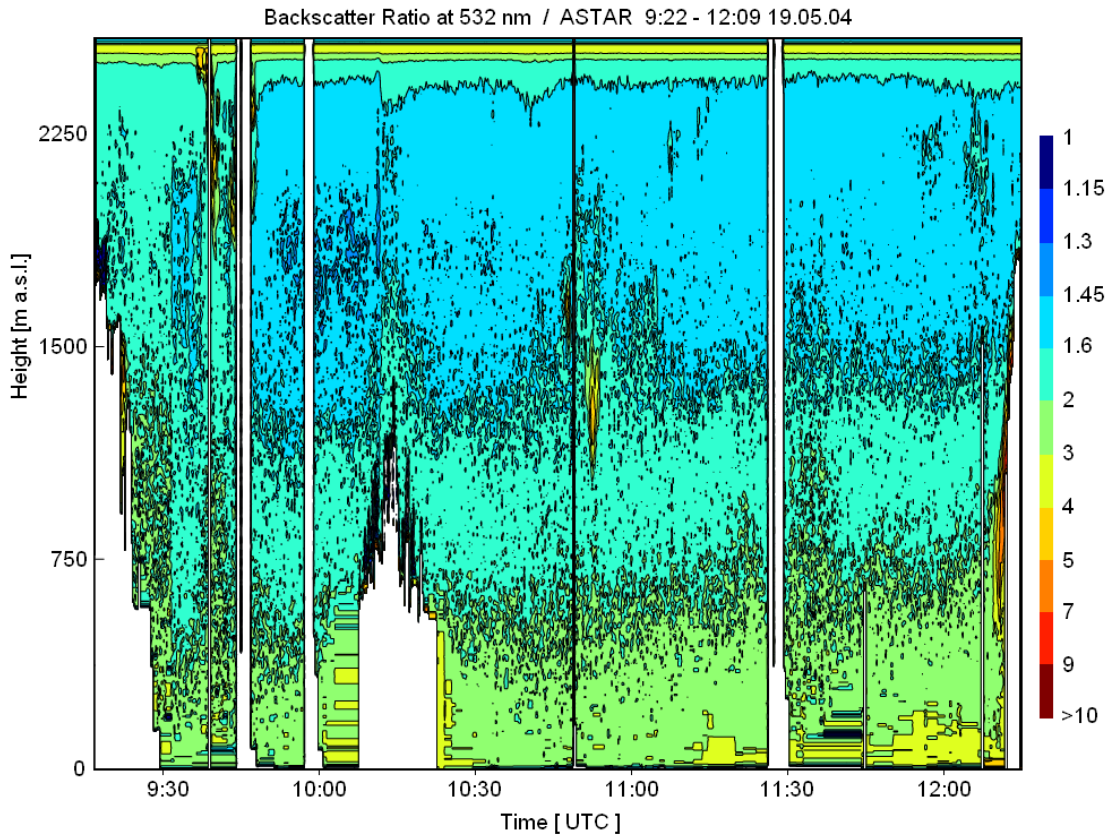


Figure 22: The calibrated backscatter ratio profiles along the flight (c.fig.4 and 18) retrieved using the iterative Klett's approach for 19 May 2004 (top) and 21 May 2004 (bottom). The data were obtained by the nadir-aiming airborne AMALi lidar from the flight altitude of 2650 m and from 3000 m, respectively, during the ASTAR campaign.

On 19 May 2004, the measurements started just after leaving the base at Longyerbyen airport. Firstly, the heading in the direction of Ny-Ålesund to overfly the stationary KARL lidar at the Koldewey Station was taken. Afterwards, the heading North-West continued until the cloud band above the ice edge was reached. Then the Polar 2 turned to South-West direction and continued along a strait path down to Bellsund mouth area. Finally, after turning offshore Wedelland plain the heading West was taken and at the latitude of Isfjord mouth changed to heading East in direction of Longyearbyen.

The simultaneous measurements of AMALi and KARL taken during the Koldewey Station overflights allowed to obtain the AMALi lidar instrumental constant $C_A = 1.43 (\pm 0.1) \cdot 10^{13} mV m^3 srad$ (c.cpt. 5.4.1) which was used in the two-stream inversion (c.cpt. 5.4.3). The obtained lidar ratio profile at the Ny-Ålesund location showed mainly background lidar ratio of $20 srad$ with a layer of extremally high values of the lidar ratio of $80 srad$ due to the existence of the aerosol layer of rather local origin (c.cpt. 5.8). Additionally, the air mass transport had a non-uniform character, whereby a contamination with the anthropogenic aerosol could not be totally excluded (c.cpt. 5.1.4 and 5.1.5). Hence, the choice of the appropriate lidar ratio for calculations along the flight was not straight forward.

Therefore, the sensitivity study with respect to the estimation of the error due to the assumption of a different type of lidar ratio were performed. For the following constraints on the lidar ratio the error of the backscatter coefficient calculation was obtained:

$$\left| \begin{array}{c} B(h) = const [srad] \\ \Delta \beta_{t1}^{part} [m^{-1} srad^{-1}] \end{array} \right| \begin{array}{c} 20 \\ \pm 1.8 \cdot 10^{-7} \end{array} \left| \begin{array}{c} 25 \\ \pm 0.3 \cdot 10^{-7} \end{array} \right| \left| \begin{array}{c} 30 \\ \pm 0.7 \cdot 10^{-7} \end{array} \right| \left| \begin{array}{c} 35 \\ \pm 1.4 \cdot 10^{-7} \end{array} \right|$$

assumed for the clean air, the clean air with a bit of aerosol, the air with considerable aerosol load, and the polluted arctic air, respectively. Additionally, the height dependent lidar ratio set to $35 srad$ between 0 - 1600 m and to $20 srad$ at 1600 - 2500 m were performed for which (within the given above uncertainties) the same values of the particle backscatter coefficients as for the corresponding constant lidar ratios results were obtained.

Hence, the sensitivity studies show no significant hindering of the iterative calculations when the constant lidar ratio is assumed. This result is mainly due to the short integration range for the AMALi measurements, so that the assumption of the constant lidar ratio does not introduce significant error, as discussed in chapter 5.5.1. The accuracy of the backscatter coefficient calculated with the iterative approach is assumed to be $\sigma_{bsc}^{IK} = 2.0 \cdot 10^{-7} m^{-1} srad^{-1}$.

The backscatter ratio profiles (c.fig. 22) were calculated with 15 s temporal resolution corresponding to 1 km spatial resolution to provide appropriate temporal and spatial resolution for the comparisons with the ECMWF operational analyses (c.cpt. 5.1) and the EULAG model results (c.cpt. 5.9.2). In case of thick clouds the backscatter ratio could not be retrieved due to the multiple scattering.

The striking feature captured on both backscatter ratio plots are the triangularly-shaped aerosol gradients measured in the North-West area offshore Svalbard. In both cases, the flight paths were nearly parallel to this aerosol gradients at the northernmost part of the flights. It is interesting to note that the triangular shape of the aerosol distribution is probably related to the vertically risen isentropic surfaces (c.fig. 19, top). Thus, the enhanced vertical transport of the sea salt aerosols from the rough sea in the region of the corner-wind is most likely responsible for high aerosol load inside the 'triangles'. This is studied in detail in chapter 5.9.2 by using a high resolution numerical model EULAG for the emission and transport of different aerosol types. For example, this analysis allowed for the interpretation of the very high backscatter ratios in the lowest altitudes at the end of the flight observed just outside the Isfjorden mouth by associating it with the Adventalen dust event which occurred a day before (c.cpt. 5.9).

5.6 Clean and polluted Arctic air and their characteristic properties

The airborne missions of ASTAR 2004 focused on investigation of horizontal and vertical extend, layering and characteristics of tropospheric aerosol of typical clean Arctic summer conditions protected from a long-range transport of polluted air masses. A similar study but for the aerosol loads contaminated with the anthropogenic origin particles advected to the Arctic from the lower latitudes was in focus of the SVALEX 2005.

The fact that the lidar measurements during both ASTAR and SVALEX were taken in the similar conditions (stable Foehn-like conditions) and in the same area of interest (overflying the Koldewey Station in Ny-Ålesund), allowed for the direct comparison of the lidar retrievals from both campaigns (c.pt. 5.1). During ASTAR Foehn-like period only few AMALi overflights were performed due to the partly cloudy conditions just over the Koldewey Station. During SVALEX three days of non-stop measurements with KARL, the longest measurement period at a time in its history, with 13 AMALi overflights covered the entire Foehn-like period.

Here the results of the comparison study with respect to measurements taken on 19 May 2004 and 14 April 2005 are presented. The first of the selected for the two-stream retrieval profiles represents the background aerosol loads of clean conditions investigated during the Foehn-like period between 18-23 May 2004. The second profile, with much higher aerosol load, is representative for the Arctic Haze event which occurred during 12-16 April 2005 Foehn-like period.

The optical properties of investigated atmosphere on each of this days were obtained using the two-stream approach. The two-stream β^{part} , α^{part} and $B(h)$ profiles obtained for both days at 532 nm were derived with the constraints described in chapter 5.4.3. The cloud screening for the SVALEX day was not necessary. The values of $C_K = 2.03 (\pm 0.1) \cdot 10^{14} mVm^3srad$ and $C_A = 1.43 (\pm 0.1) \cdot 10^{13} mVm^3srad$ and a boundary condition of $\beta_{ref}^{part} = 0.3 (\pm 0.05) \cdot \beta^{mol}$ were used for the calculations for both days. The uncertainty of the retrieved two-stream extinction σ_{ext}^{TS} is $1 \cdot 10^{-6} m^{-1}$ and the error of the two-stream backscatter σ_{bsc}^{TS} is $1.5 \cdot 10^{-7} m^{-1} srad^{-1}$.

Sets of profiles $\alpha^{part}(h)$, $\beta^{part}(h)$, and $B(h)$ obtained for each day are presented in figure 25. These profiles were compared between each other and interpreted in terms of their optical properties (extinction, backscatter, depolarisation, optical depth), macrophysical properties (humidity, temperature, origin) and microphysical parameters (refractive index, size distribution and particle number concentration) providing 'clean' contra 'haze' characteristics (c.pt. 5.6.2 and 5.6.3, respectively).

5.6.1 General situation during ASTAR 2004 and SVALEX 2005

General situation during ASTAR 2004

The preliminary analysis of all of the aerosol airborne in-situ measurements taken from onboard the Polar 4 aircraft during the whole ASTAR 2004 campaign (Matsuki et al. [123]) confirmed the typical clean Arctic background conditions characterised by low values of aerosol concentrations and extinctions and low variability throughout the whole troposphere (c.fig. 23).

However, during some flights distinct differences between different layers in the free troposphere were found, both for accumulation mode aerosol and fine particles. On some days an intensive new particle formation in marine boundary layer near Ny-Ålesund reaching aerosol number concentration up to $3\text{-}4 \cdot 10^3 ppcm^{-3}$ were observed. On the flights performed in centre of low pressure system were it was measured very clean air mass with almost completely depleted accumulation mode aerosol and relatively high total number concentrations ranging from $5\text{-}10 \cdot 10^2 ppcm^{-3}$ in marine boundary layer and in free troposphere.

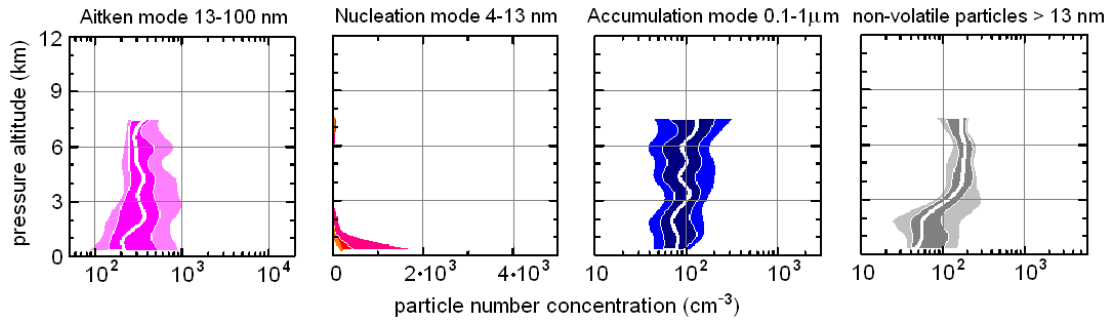


Figure 23: *The preliminary results of the aerosol in-situ measurements obtained from all Polar4 flights justifying the clean Arctic background conditions during the ASTAR 2004 campaign. Provided by A. Minikin (DLR-IPA, Germany).*

The in-situ and remote ground-based measurements at the Koldewey, Rabben and Zeppelin stations generally confirmed the airborne observations. Very clean conditions manifested in the low amounts of the light absorbing particles (soot) remaining below 10 ng cm^{-3} for long periods. Particle number densities ranged from less than 200 to above 1000 ppcm^{-3} with very low concentrations of large particles (less than few ppcm^{-3}).

According to sunphotometer measurements taken in Ny-Ålesund, only low aerosol contaminations were observed. The daily average of the particle optical depths τ_{sun}^{part} retrieved for the 532 nm was varying around 0.075 and 0.055 at the beginning and end of the ASTAR Foehn-like period (c.fig. 24). The low values of the Ångström exponent suggests that the values of τ_{sun}^{part} must be, at least partially, addressed to the existence of the passing subvisible clouds or Cirrus (Sassen and Arnott [124]).

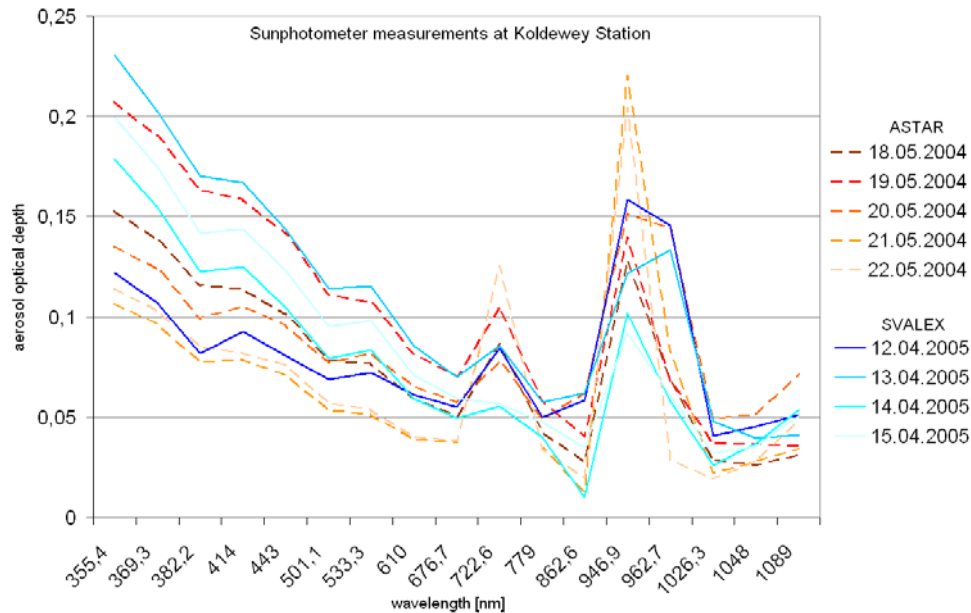


Figure 24: *The comparison of the daily averaged particle optical depth spectra obtained with the sunphotometer during the Foehn-like period at ASTAR (dashed redish curves) and SVALEX campaigns (solid blueish). The sunphotometer data were provided by A. Herber (AWI Bremerhaven, Germany).*

From KARL's measurements, usually, background values of backscatter and extinction coefficients with no depolarisation justifying the existence of only spherical particles were retrieved. For some days a humid layers of enhanced extinction, hardly visible in the backscatter profiles, were obtained also from KARL's Raman measurements (c.cpt. 5.8). Additionally, sometimes high values of volume depolarisation at 532 nm below 2 km altitude were recorded, indicating elongated particles of ice crystals or diamond dust.

General situation during SVALEX 2005

During the SVALEX Foehn-like period the daily average of the particle optical depths derived from the sunphotometer data at 532 nm varied between 0.065 and 0.12 (c.fig. 24). These high values address the haze aerosol, since no existence of Cirrus or subvisible clouds in troposphere was observed, except for the 12 May 2005. The sunphotometer data were corrected for the ozone contribution at the wavelengths within the ozone absorption band ($350\text{ - }370\text{ nm}$ and $450\text{ - }800\text{ nm}$), i.e. in the case of the 533 nm detection channel the correction of the particle optical depth of about 0.02 for the $300\text{ - }350\text{ DU}$.

Generally, KARL's retrievals showed high particle extinction coefficient around $3\text{ - }4 \cdot 10^{-5}\text{ m}^{-1}$ (form 607 nm) and high particle backscatter coefficient $1\text{ - }2.5 \cdot 10^{-6}\text{ m}^{-1}\text{ srad}^{-1}$ (form $532\text{ nm}/607\text{ nm}$) with lidar ratios of around 35 srad , i.e. values characteristic for the polluted arctic spring condition. Only low volume depolarisation ratios at 532 nm were recorded. Also during the SVALEX at some days layers of strongly enhanced extinction, hardly visible in the backscatter profiles, were observed (c.cpt. 5.8).

5.6.2 Background aerosol load at ASTAR campaign

The two-stream profiles of the particle extinction coefficient, the particle backscatter coefficients and corresponding lidar ratio obtained for 532 nm on 19 May 2004 are presented in figure 25 (dashed).

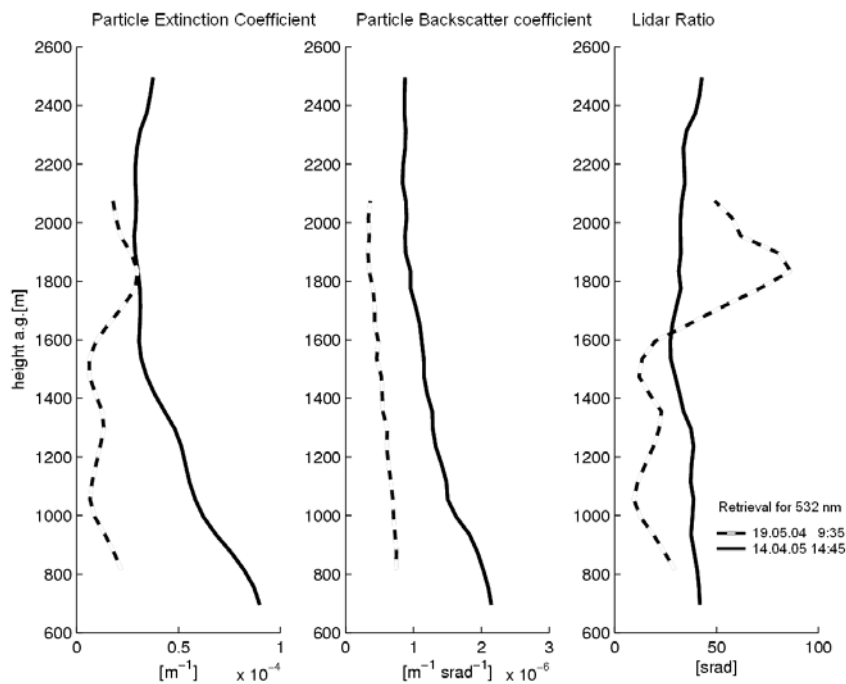


Figure 25: The two-stream β^{part} , α^{part} and $B(h)$ profiles obtained for 532 nm on 19 May 2004 (dashed) ASTAR and 14 April 2005 (solid) SVALEX measurements.

For data of 19 May 2004 recorded at around 9:35 UT a height interval between 815 m and 2075 m was analysed. The aerosol layer with a maximum at about 1800 m altitude with α^{part} enhanced up to $0.3 \cdot 10^{-4} m^{-1}$ and lidar ratio of 80 $srad$. Otherwise the air was clean with typical for the Arctic background values of particle extinction of $0.15 \cdot 10^{-4} m^{-1}$, lidar ratio of 20 $srad$ and very low values of particle backscatter increasing towards the ground level in a range of $0.3-0.7 \cdot 10^{-6} m^{-1} srad^{-1}$. The total optical depth calculated for the layer where the two-stream method was applied τ_{layer} sums up to 0.035 with particle optical depth τ_{layer}^{part} of 0.02.

The sunphotometer measurements in Ny-Ålesund at 9:40 UT on that day recorded τ_{sun}^{part} 0.107 for green light, partly contaminated by passing subvisible clouds at about the flight altitude and Cirrus at 8-9 km , both detected also by KARL. However the high value of the Ångström exponent indicates the existence of small particles which might be due to the aerosol contamination or the existence of a small water droplets (c.fig. 24).

The radiosonde ascent at 11:00 UT in Ny-Ålesund (c.fig. 13, green) show general trend of increase of the relative humidity (from 58% to 72%) and decrease of the temperature (from $-8^{\circ}C$ to $-14^{\circ}C$) with the height within the layer where the two-stream was applied. The temperature inversion at about 1800 m is evident (c.cpt. 5.8).

The inversion of the microphysical parameters of the profiles measured on 19 May 2004 was not possible, since the condition of providing the set of at least 2 α and 3 β necessary for the inversion (c.cpt. 4.7) was not fulfilled, due to the failure of KARL's 355 nm detection channel. Therefore, inversion for the set of retrieved backscatter and extinction profiles obtained with KARL on 18 May 2004 is given in figure 26. As the measured on that day background values of extinction and backscatter coefficients were in the order of magnitude of the ones measured on the 19 May 2004, as well as on other clear-sky days during the campaign, the obtained results are considered as representative for most measurements during ASTAR.

The values characteristic for the background conditions of the complex refractive index $m = 1.4 + 1 \cdot 10^{-4}i$ typical for the water particles, the bimodal size distribution (Morawska et al. [125]) dominated with only a few large particles of the effective radius varying between 0.6-1.2 μm with very narrow σ of 1.26 and an extremely low particle concentrations varying between 0.5-3 cm^{-3} were retrieved.

Generally, during most days of the ASTAR campaign, the NOAA HYSPLIT backward trajectories calculated for the Ny-Ålesund location showed the air trapped at lower tropospheric layers in the high Arctic (c.cpt. 5.1.4). Although, for 19 May 2004 the NOAA HYSPLIT backward trajectories (c.fig. 14) and the FLEXPART retroplum (see: Polar 2 time 1 at <http://zardoz.nilu.no/~andreas/ASTAR/>) show air masses passing through non-polar regions at a different locations for the various analysed altitudes. In addition the FLEXPART indicated possible antropogenic pollution in-take over Finland and Kola Peninsula at about 1800 m , which is an altitude corresponding to the maximum extinction on this day (c.fig. 25). However, the contamination with the antropogenic pollution from the lower laltitudes seem not likely due to the very low extinction of these air mass. Therefore, the air measured on 19 May 2004 can be interpreted as a typical for the clean summer conditions in Arctic (d'Almeida et al. [126], Covert et al. [127], Zielinski and Patelski [58]), with a humid layer of local origin rather than of an advection phenomenon (c.cpt. 5.8).

5.6.3 Increased aerosol load at SVALEX campaign

For the measurements taken on 14 April 2005 at around 14:45 UT the analysed height interval between 700 m and 2500 m show strongly enhanced β^{part} , α^{part} and $B(h)$ in comparison with the corresponding ASTAR profiles. The lowest values of the particle extinction are around $0.3 \cdot 10^{-4} m^{-1}$ corresponding to the maximum of the measured values on 19 May 2004. Likewise, the values of the backscatter are much higher then previously

varying between $0.9 - 2.2 \cdot 10^{-6} m^{-1} srad^{-1}$. The lidar ratio varies around $35 srad$ indicating polluted Arctic atmosphere. The total optical depth of the two-stream layer τ_{layer} sums up to considerable 0.095 with the particle optical depth τ_{layer}^{part} of 0.076 .

The sunphotometer measurements at 14:45 in Ny-Ålesund for the green light recorded τ_{sun}^{part} of 0.084 (c.fig. 24), while for the whole Foehn-like period mean value of 0.099 in Ny-Ålesund and of 1.19 in Longyerbyen was obtained, interpreted as high enough to be associated with Arctic Haze particles (Heintzenberg [11]).

There is no evidence of Cirrus or subvisible clouds in upper troposphere from KARL measurements and both lidars show no depolarisation signature at $532 nm$.

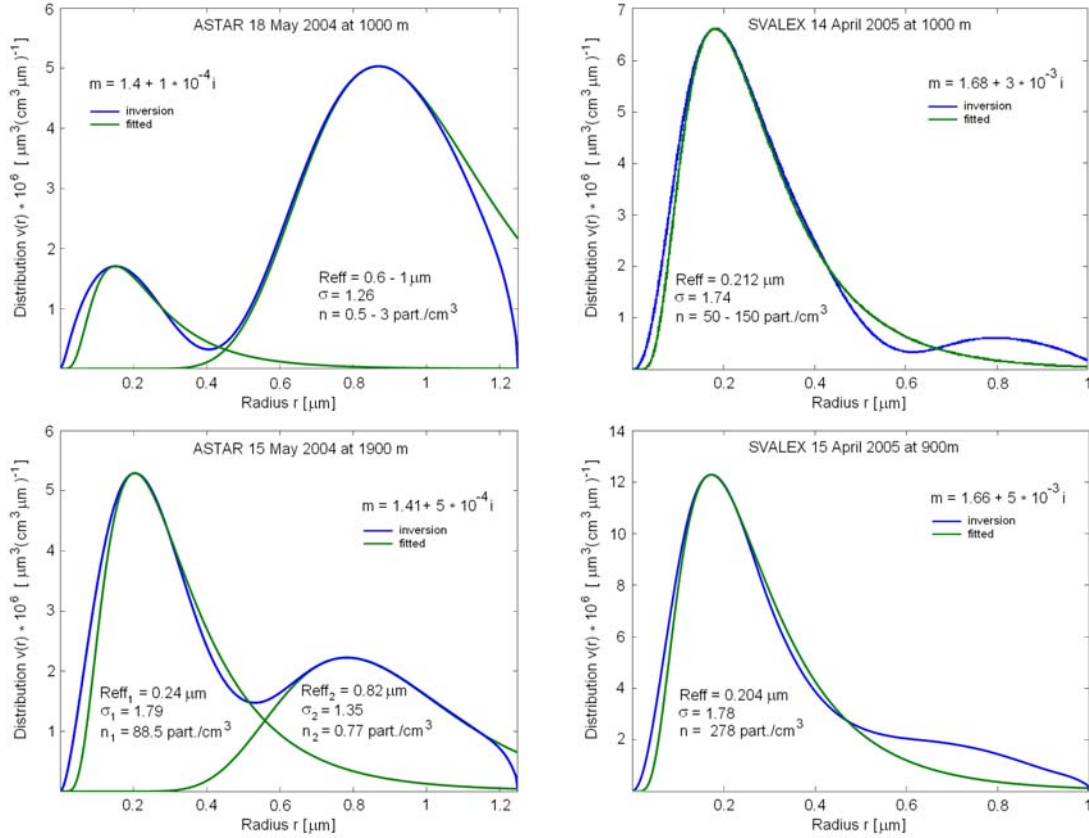


Figure 26: The results of the microphysical parameter inversion obtained for the sets of the KARL's α^{part} and β^{part} at $355 nm$, $532 nm$ and $1064 nm$. On 18 May 2004 and 14 April 2005 retrieved values represent the characteristic clean (ASTAR) and polluted (SVALEX) conditions. On 15 May 2004 and 15 April 2005 calculations were done for the altitudes corresponding to the layers of strongly enhanced α^{part} undiscernible in β^{part} , independent on the clean/polluted conditions during both campaigns (c.cpt.5.8). The microphysical parameter inversion code was provided by Dr C. Böckmann and A. Kirsche (University of Potsdam, Germany). The calculations were performed from the KARL's measurements by Dr C. Ritter (AWI-Potsdam, Germany).

The radiosonde ascent at 12:30 UT in Ny-Ålesund recorded the mean value of relative humidity of 31% and temperature of $-12.2^\circ C$ within the layer where the two-stream was applied (c.fig. 13). The decrease of temperature and relative humidity dropping from 50% at $700 m$ to its minimum of 22% at about $2000 m$ and rising again to reach 28% at $2500 m$ shows similarities with the particle extinction profile. Just below a weak inversion layer seem to be present, otherwise there is no evidence of existence of inversions up to

tropopause.

The inversion of the microphysical parameters for KARL's measurements on 14 April 2005 retrieved the complex refractive index $m = 1.68 + 3 \cdot 10^{-3}i$ typical for anthropogenic aerosol (c.fig. 26). Slightly higher than usual value of $Re\ m$ indicate possible soot contamination, not unusual during the Arctic Haze events in this area (Yamanouchi et al. [19]). The size distribution is characterised by a monomodal log-normal distribution (Morawska et al. [125]) with the effective radius of $0.2\ \mu m$ with σ of 1.7 and high particle concentrations varying between $50 - 150\ cm^{-3}$.

Both, the NOAA HYSPLIT and the FLEXPART analysis, indicate the uniform transport from Yenisey and Lena Delta where the soot particles can be expected as a source of contamination (c.cpt. 5.1.4 and 5.1.5). The local source of contaminations with CO , NO_2 and SO_2 are possible at Ny-Ålesund area at 14:45.

The measured enhanced values for the extinction and the backscatter coefficient with almost constant but significantly higher than typical clean Arctic air lidar ratio values, the low humidity and volume depolarisation with the high particle concentrations together with the trajectories justify anthropogenic contaminations. Especially the high extinction of this air and long duration of its way through mid-continental area makes such contaminations possible. Therefore, advection of anthropogenic origin air masses from the mid-latitudes, i.e. the Arctic Haze event, seems more likely than any local contaminations.

5.7 Estimation of the temporal progress of the Arctic Haze event during SVALEX campaign

In this chapter a study focused on the Arctic Haze temporal progress for the observations taken on 15 April 2005 during the day of the strongly enhanced aerosol load in the vicinity of Ny-Ålesund and Longyearbyen under the Foehn-like conditions during the SVALEX campaign is presented. On that day sunphotometers in both mentioned sites recorded the highest values of the particle optical depth, while generally higher values were measured during the whole campaign in Longyearbyen.

On 15 April 2005 between 11:46-13:04 UT AMALi flew 5 times over KARL. For brevity here 3 of these overflights, first, third and fifth, referred to as t_1 , t_3 and t_5 , are analysed and interpreted.

The data obtained for each of these overflights are directly comparable, as each was made along the same flight path and against the wind direction blowing from the glacier located in south-eastern end of the fiord towards the mouth of the fiord. The flight turn points were done over an open sea outside the fiord and over a the Tre Kroner behind the glacier. The aircraft cruising speed was lowered to a minimum of 90 kt for each overflight which allowed to acquire highest possible number of laser-shots within the area of interest and to increase the representativity of the data collected with AMALi. Hence, the best compatibility of KARL signals averaged over time with AMALi signals averaged over time and space was achieved.

The calculations of the sets of particle extinction and backscatter coefficient and the corresponding lidar ratio profiles was done using the two-stream approach (c.cpt. 5.4 and 4.5). In contrary to the standard two-stream approach where the backscatter ratio calibration value is set to unity at the range where both signals show the same shape (Cuesta [128]) in our case it is calculated for each of the times from equation 28 with the transmittance term obtained from the two-stream extinction profiles for that particular time and the lidar instrumental constants obtained according to chapter 4.5.2. Within the given uncertainties the values of both constants at $532\ nm$ were the same for each time interval, i.e. $C_K = 1.03(\pm 0.1) \cdot 10^{14} mV m^3 srad$ and $C_A = 4.2(\pm 0.1) \cdot 10^{13} mV m^3 srad$. The advantage of this approach over the mentioned above standard approach is clear. Even in very clean Arctic atmosphere, as during the ASTAR 2004, the background backscatter

ratio values ranges between 1.2-1.6 (c.fig. 20 and 30), i.e it is always higher than the value of the backscatter ratio due to the molecules alone, which is by definition unity. Hence, the standard approach results in bias in the backscatter ratio and the lidar ratio retrievals, while this approach not.

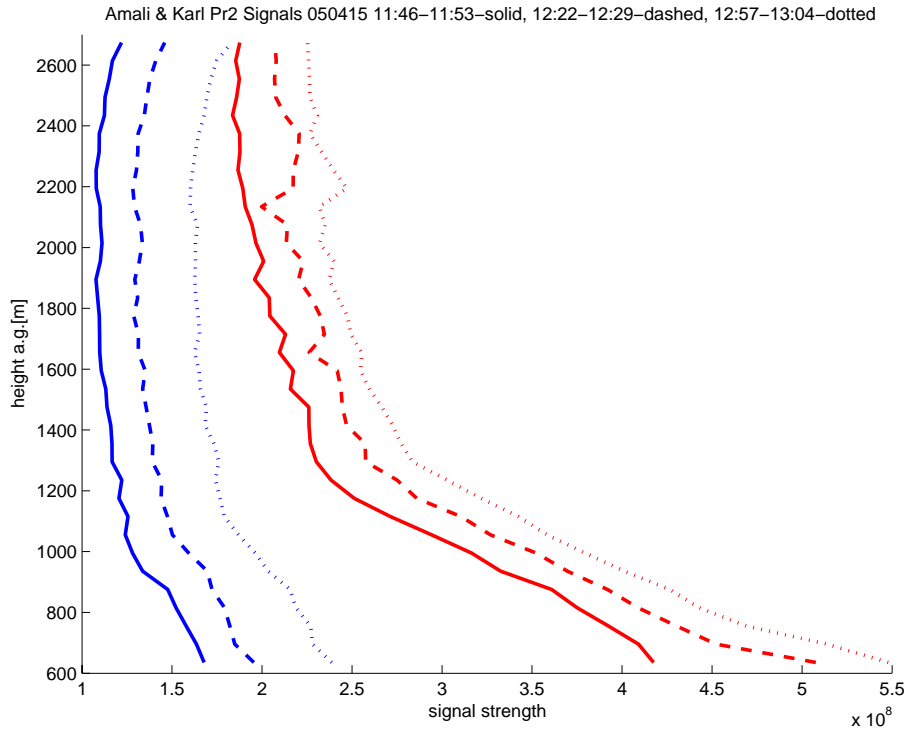


Figure 27: The range and background corrected signals at 532 nm of AMALi (blue) and KARL (red) for time intervals t_1 (solid), t_3 (dashed) and t_5 (dotted) obtained on 15 April 2005 during the Arctic haze SVALEX measurements. The signals are investigated prior to the two-stream method application to pre-select the regions for the inversion.

The visual inspection the range and background corrected lidar signals (c.fig. 27) within a range of KARL's and AMALi's completed overlap (0.6-2.64 km) show significant differences at particular altitudes where systems sampled into different air, i.e. for all profiles between 2.1-2.64 km directly below AMALi lidar and for t_3 profile at around 1.65 km. The visual assesment of the lowest range of the applicability of the method is not as strait forward, due to the strong increase of the KARL's signal.

The range of the two-stream applicability was defined in a layer between 1.2-2.1 km for each profile (c.fig. 28). The optical properties retrieved for 532 nm within this layer range with the uncertainties obtained as in chapter 5.4.3 are given below:

profile	$\alpha_{layer}^{part} [m^{-1}]$	$\beta_{layer}^{part} [m^{-1}srad^{-1}]$	$B_{layer} [srad]$	τ_{layer}^{part}
t_1	$2.8 (\pm 0.1) \cdot 10^{-5}$	$1.1 (\pm 0.15) \cdot 10^{-6}$	26	0.026
t_3	$4.6 (\pm 0.1) \cdot 10^{-5}$	$1.4 (\pm 0.15) \cdot 10^{-6}$	33	0.042
t_5	$4.7 (\pm 0.1) \cdot 10^{-5}$	$1.45 (\pm 0.15) \cdot 10^{-6}$	32	0.043

Each of the AMALi and KARL signals and the retrieved backscatter and extinction profiles show fast (within about an hour) increase for each overflight to the values typical for polluted arctic air (d'Almeida et al. [126]).

Interesting enough that below 1.2 km a layer of enhanced extinction and lidar ratio, similar to these found during the ASTAR measurements, is evident (c.cpt. 5.8).

Since overflights were performed in the same area, a contamination with the aircraft's exhaust itself has to be taken into account. However, the visual observations of a decrease of the visibility in Kongsfjord during these overflights linked it with an advection of the pollution from the direction of Longyearbyen (Stachlewska [79]). Both, the long-range transport of the continental pollutants, as well as contaminations of a local origin cannot be excluded. Two possible scenarios can explain the obtained optical parameters, an advection of particles of the same composition and microphysical properties but larger in size at each time or/and an advection of particles of the same size and composition which start to grow in Kongsfjord.

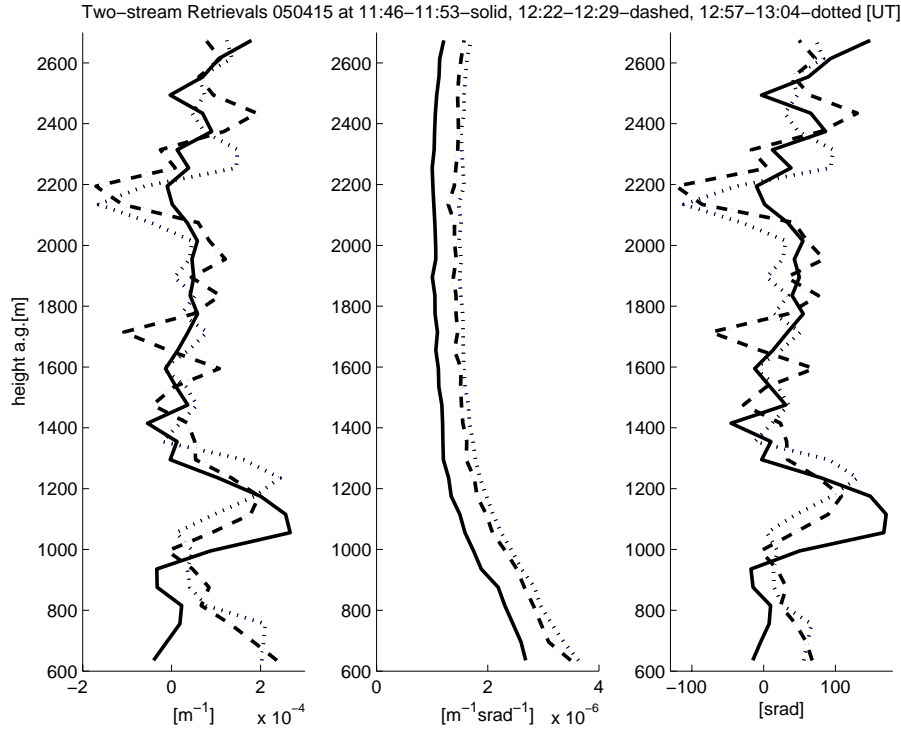


Figure 28: The two-stream 532nm β^{part} , α^{part} and $B(h)$ profiles for time intervals $t1$ (solid), $t3$ (dashed) and $t5$ (dotted) retrieved for 15 April 2005 during the Arctic Haze SVALEX measurements. At about 1200 m a layer of strongly enhanced particle extinction coefficient is evident. The negative values at about 1700 m ($t3$) and at 2200 m ($t3$ and $t5$) are caused by lidars sampling into different air masses (c.fig.26).

This study demonstrates a great advantage of the two-stream method over the Raman method for observations of the temporal development of the small-scale atmospheric events. The typical day-time KARL's Raman extinction profile has a resolution of 1-3 h (c.pt. 3.1). In special cases the resolution of such retrievals can be improved to 20 min (c.pt. 5.4.3). However, in this latter case the evaluation is very difficult due to significantly large noise of the Raman signals and, hence the strong dependence of these retrievals on applied smoothing.

Lowering of the cruising speed of the Polar 2 aircraft to the minimum (90 kt) allows for prolongation of the sampling time of 'the same' air mass by both lidars during the AMALi's overflights. Hence, the two-stream retrievals with 8-10 min averaging are provided. Such adjustment of the speed of the CALIPSO satellite during the future CALIPSO lidar and KARL lidar validation experiments will not be possible.

Therefore, during the next ASTAR campaign the measurements in an extra mode, namely the zenith-aiming airborne AMALi and the CALIPSO lidar, shall be performed to

increase the compatibility area between both systems. An example of basic geometrical considerations for any airborne-satellite hybrid experiments allowing the assesment of the airborne configuration parameters (flight path, flight altutude) can be found in Gebhardt et al. [129].

5.8 Investigation of the occurence of the humid layers over Ny-Ålesund

On 15 May 2004 and 19 May 2004 during ASTAR and on 15 April 2005 during SVALEX layers of a strongly increased particle extinction coefficients and lidar ratios, hardly visible in the particle backscatter profiles obtained at 532 nm using the two-stream method are clearly evident in the lowest 2000 m . Moreover, for all of these layers both AMALi and KARL lidars showed no depolarisation signature at this wavelength.

During both ASTAR days at an altitude of about 1800 m a layer of lidar ratio around 80 srad and enhanced particle extinction up to $6 \cdot 10^{-5}\text{ m}^{-1}$ for 15 May 2004 and $3 \cdot 10^{-5}\text{ m}^{-1}$ for 19 May 2004 was retrieved

Additionally, at an altitude of about 900 m an aerosol layer of lidar ratio around 60 srad and enhanced particle extinction up to $8 \cdot 10^{-5}\text{ m}^{-1}$ for 15 May 2004 was found (c.fig. 21). During the SVALEX day on 15 April 2005 at an altitude of about 1150 m an aerosol layer of lidar ratio around 100 srad and enhanced particle extinction up to $1.8 \cdot 10^{-4}\text{ m}^{-1}$ is clearly visible (c.fig. 28). The characteristic of these layers in terms of their optical properties at 532 nm is given below:

Date	Time [UT]	Height [m a.s.l.]	$\alpha_{in\text{ layer}}^{part}$ [m^{-1}]	α^{part} [m^{-1}]	$B_{in\text{ layer}}$ [srad]	B [srad]	β^{part} [$\text{m}^{-1}\text{srad}^{-1}$]
15.05.04	10:00	900	$8 \cdot 10^{-5}$	$1.5 \cdot 10^{-5}$	60	20	$0.7 \cdot 10^{-6}$
15.05.04	10:00	1800	$6 \cdot 10^{-5}$	$1.5 \cdot 10^{-5}$	80	20	$0.7 \cdot 10^{-6}$
19.05.04	9:35	1800	$3 \cdot 10^{-5}$	$1.5 \cdot 10^{-5}$	80	20	$0.3 \cdot 10^{-6}$
14.04.05	14:45	N/A	N/A	$3 \cdot 8 \cdot 10^{-5}$	N/A	35	$0.9 \cdot 2.2 \cdot 10^{-6}$
15.04.05	12:25(t3)	1150	$1.8 \cdot 10^{-4}$	$4.6 \cdot 10^{-5}$	100	33	$1.3 \cdot 10^{-6}$

where all values obtained for the existing layers of strongly enhanced extinction and lidar ratio (assigned *in layer*) are shown next to the mean values obtained for the same measurement outside these layers.

As possible causes for the existence of these layers the following were considered: the contaminations with strongly absorbing long-range radiation particles, as soot (Yamanouchi [19]) of local origin or advected from the lower latitudes; the precondensation (Kasten [130]) recorded prevalently by KARL as subvisible water clouds; the existence of a Foehn-like pause formed as result of retreat of the orographic wave pattern characterised by rapid fall of the temperature and increase of the relative humidity (Carnuth et al. [131]); the cumulation of the particles under the stable, thin inversion layer capping the mountain gap flow layer on the downstream flow into the Kongsfjord valley (Mayr et al. [132]).

The microphysical parameters retrieval justify a possible contamination by soot particles (compare Rem) within the layer on the 15 April 2005 (c.fig. 26, bottom right). The obtained values of m , σ and R_{eff} are similar to the retrieved for the previous day (top right). However, on the 14 April 2005 the layers are not visible at any altitude where of the profiles were obtained (c.fig. 25). The strong increase of the small sized particle number concentrations in the layer (almost doubling, if compared to the calculations beyond) is remarkable.

Noteworthy, a similar results were obtained for the comparison of the microphysical properties of the clean background air on 18 May 2004 dominated by a few large particles

(c.fig. 26, top left) with the values retrieved for the layer visible on 15 May 2004 dominated by significantly larger amount of a small sized particles (bottom left). While, again the m (typical for water particles), as well as σ and R_{eff} retrieved for the large sized particles remain similar.

The long-range transport for each of the days shows the air mass origin in both, the high Arctic or at the lower latitudes (c.cpt. 5.1.4). According to the backward trajectories on the 19 May 2005 soot contaminations within the layer, at least theoretically, could have been possible (c.fig. 14, 1800 m , top right). However, the enhancement of the particle extinction occurs even stronger (c.fig. 21, 1800 m red) for the air trapped isolated in the Arctic on 15 May 2004 (c.fig. 14, all levels, top left). The only possible anthropogenic contaminations of this air could be due to the existence of the aged pollutants, which were not evident from the obtained microphysical parameters.

The layers occurred during the clean (15 May 2004 and 19 May 2004) and the polluted (15 April 2005) conditions, as well as during the Foehn-like events (19 May 2004 and 15 April 2005) and during the 'normal' clear-sky conditions (15 May 2004).

However, all found layers were strongly dependent on existence of the inversion layers, evidenced from the radio sounding (c.fig. 13). In all cases, independently on clean or polluted conditions, the radiosonde data confirmed the existence of layers with humidity of 50-90% and temperatures down to $-13.5^{\circ}C$, although some of the radiosonde launches took place up to two hours after the AMALi's overflights over the Koldewey Station (c.cpt. 5.1.3).

The characteristic of these inversion layers in terms of their thickness ΔH , temperature ΔT_{inv} and relative humidity ΔRH_{inv} as well as the strength of temperature and relative humidity gradients is given below:

Date	Time [UT]	H	ΔH	ΔT_{inv}	ΔRH_{inv}	$\frac{\Delta T_{inv}}{\Delta H}$	$\frac{\Delta RH_{inv}}{\Delta H}$
	[UT]	[m a.s.l.]	[m]	[$^{\circ}C$]	[%]	[$^{\circ}C m^{-1}$]	[% m^{-1}]
15.05.04	11:00	1200	140	2.0	37	0.143	0.264
15.05.04	11:00	1800	40	0.4	21	0.01	0.525
19.05.04	11:00	1800	50	0.6	7	0.012	0.140
14.04.05	12:30	700	60	0.3	4	0.005	0.066
15.04.05	11:00	1000	130	1.0	40	0.008	3.077

The enhanced particle extinction coefficient, together with the high lidar ratios, the low particle backscatter coefficient, the low volume depolarisation and the inversion-related relative humidity and temperature suggest that the layer was composed of a large number of a very small, spherical, supercooled water droplets, not unusual at the pristine conditions of our polar site. Such low temperatures do not contradict with the existence of water droplets at low altitudes in Arctic (c.cpt. 5.10). Over the Beaufort Sea at altitudes below 2 km and temperatures down to $-9^{\circ}C$ clouds generally contain purely liquid particles (Pinto et al. [133]).

More credible than the long-range advection of pollutants is the local origin of such layers due to the local meteorological disturbances at the measurement site caused by surrounding mountains of an altitude varying around 800 m on both sides of the Kongsfjord with the Tre Kroner peaks exceeding altitude of 1200 m in the south-west end of the fjord valley. The water droplets are accumulated just below the inversion layers (c.cpt. 5.1) caused by enhanced vertical mixing in the turbulent flow over the rough Svalbard mountain. The contamination of some of these layers with low amounts of soot of the advective origin is possible and might cause, due to the absorption of the 532 nm laser light, even stronger particle extinction coefficient enhancement in the layer, as on 15 April 2005.

5.9 Aerosol variability in the Foehn-like gap area during ASTAR campaign

The aim of this work is to investigate the variability of the marine boundary layer aerosol load using airborne AMALi measurements (c.cpt. 5.9.1) and the interpretation of these data in terms of satellite imagery, the long-range air mass transport and small-scale model simulations (c.cpt. 5.9.2). As the ASTAR flights of the 19 May 2004 and 21 May 2004 showed the similar characteristics of the aerosol distribution along the straight South - North flight tracks (c.cpt. 5.5.2), the analysis in the following sections concentrates on the first observation.

5.9.1 The categorisation of the lidar backscatter ratio profiles

For a study of the temporal and spatial variability of the marine boundary layer aerosol the actual flight path has to be carefully planned before the flight to fulfil the requirement of passing at a particular times the pre-defined points along the flight, while the wind pattern, the pilots skills, the available flight time and as large as possible aeral coverage are to be accounted for pattern planning.

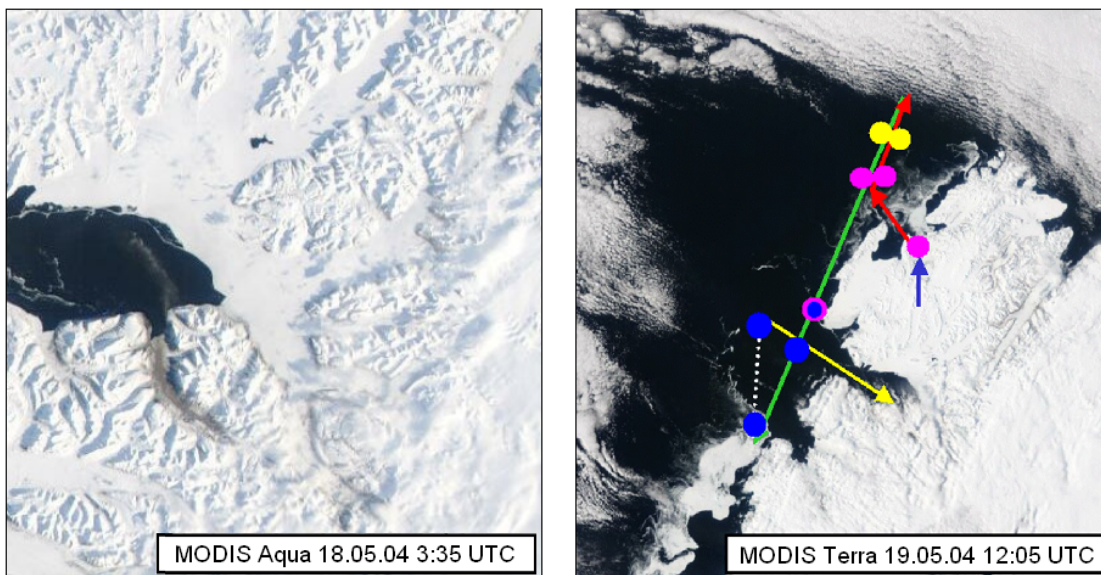


Figure 29: The different areas of the selected profiles along the flight path are shown schematically on MODIS Terra image on 19 May 2004 (right). The dust in the Adventdalen captures by MODIS Aqua channel on 18 May 2004 (left). Source: <http://rapidfire.sci.gsfc.nasa.gov>

The calibrated backscatter ratio profiles along the flight path between 9:26 - 12:05 UT on the 19 May 2004 were calculated using the iterative backward Klett approach described in chapter 4.6. Figure 30 shows 9 selected backscatter ratio profiles calculated with a constant lidar ratio of 25 srad , and averaged over 1 min , corresponding to about 4 km horizontal resolution and 7.5 m vertical resolution. The profiles were selected along the flight path shown schematically on the MODIS Terra image on the right hand side of the figure 29. Each of the retrieved profiles is confined to a particular area along this path and represents characteristic aerosol load. Hence, the categorisation to three groups marked with a pink, yellow and blue dot was possible (c.fig. 30).

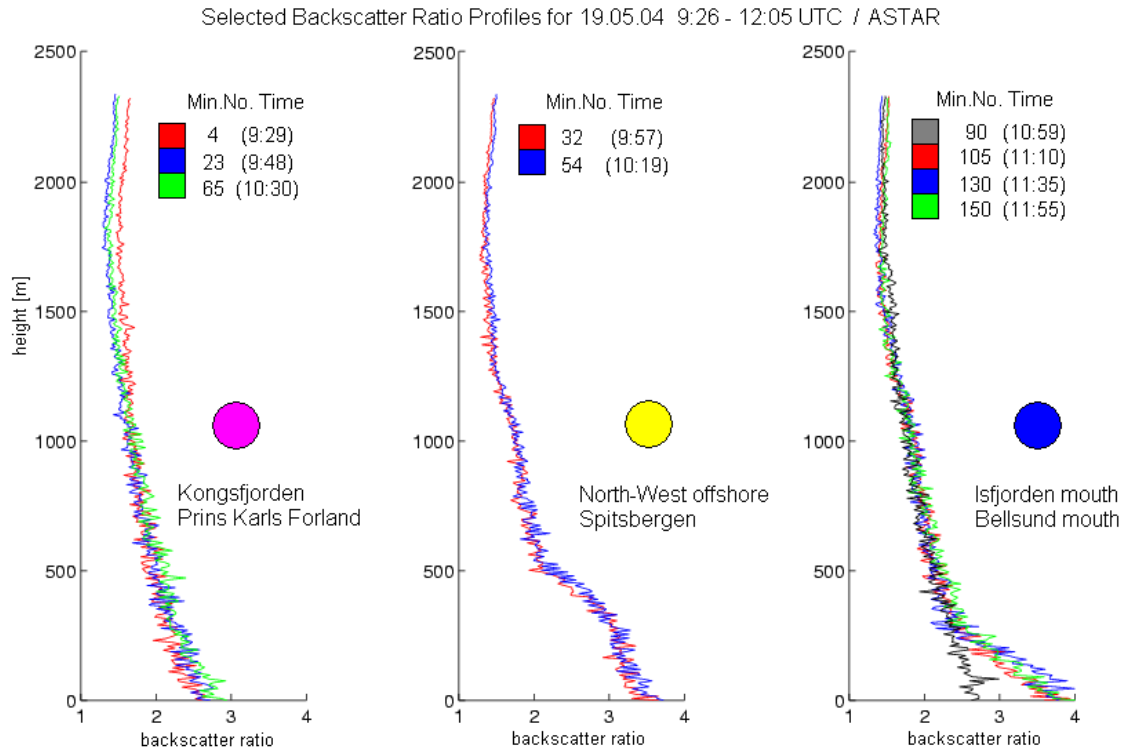


Figure 30: The selected along the flight path backscatter ratio profiles at 532 nm obtained for measurements on 19 May 2004 during ASTAR. The stable conditions in the Foehn-like gap area can be assessed from the temporal and spacial variability of the profiles confined to the different areas along the flight path shown schematically on the right hand side of the MODIS image in figure 29.

The profiles found in the *pink category* are characteristic for the typical low aerosol load Arctic atmosphere with maximum backscatter ratio values of 2.6 near the sea level. The background values are around 1.6 for the profile measured at 9:29 UT (4th minute of the lidar observation) corresponding to the AMALi overflight of Koldewey Station in Kongsfjorden. The remaining two profiles in pink category selected offshore west tipp of Spitsbergen show even lower backscatter ratio values of 1.3. It is interesting that these two profiles measured at almost the same area, though with 42 *min* delay (at 9:48 and 10:30) still reveal a similar structure. This means that the meteorological conditions have not much changed in this period resulting on higher/lower aerosol contaminations due to the horisontal or vertical transport.

The profiles in the *yellow category* measured even further north-west off Spitsbergen at 9:57 and 10:19, i.e. with 22 *min* delay with respect to each other, also coincide very well. Their background values at above 1500 *m* were around 1.3 but strong aerosol load in lowest 500 *m* with maximum of 3.5 above the sea level and elevated up to 1200 *m* aerosol load of backscatter ratio around 2 were observed.

Also the three profiles of the *blue category* taken at 11:10, 11:35 and 11:55 offshore Isfjorden mouth and Bellsund mouth coincide very well. In contrary to the previous categories these profiles were obtained at distances of 50-100 *km*, i.e. well spatially separated from each other. Consequently, an assessment of the spatial variability of the atmosphere for this category is possible. The backscatter ratio background values of all these profiles are around 1.4 and their vertical aerosol distribution resembles the one of the pink category. In contrast, the sharp gradient occurred at the lower altitude below 300 *m* in the

blue profiles, where much higher backscatter ratio of 4 near the surface were obtained.

Although rather close to the other blue profiles (both, in time and space), the 10:59 (90th minute of observation) profile is different and very similar in magnitude and shape to the pink observations. This and all pink profiles were taken in the lee of Svalbard mountains and north of the Isfjorden indicating similar conditions of atmospheric transport and mixing of aerosols. All other vertical profiles are different as they contain a sharp gradient either at about 500 *m* (yellow northernmost profiles) as at about 300 *m* (blue profiles south of the mouth of Isfjorden).

The significantly enhanced backscatter ratios close to the northernmost turning point of the Polar 2 can be explained by the vertical rise of the planetary boundary layer height as shown by the inclined ECMWF isentropic surfaces (c.fig. 19, top) and the lifted capping inversion height in the 19 May 2004 radiosonde profile (c.fig. 13, green). Thus, the associated violent turbulent mixing of sea salt aerosols emitted from the ocean might have affected the shape of the yellow profiles. This slightly higher values of the background backscatter ratio above 1200 *m* altitude are probably related to the greater vertical transport of humid air from the lower troposphere by the strong updrafts related to the flow past Svalbard.

Lower horizontal wind speed and the absence of the counter-rotating vortices at the northern tip of Svalbard might have reduced the vertical mixing south of Isfjorden. Hence, the altitude of the gradient is lowered (southward) and the pink and blue profiles themselves are much steeper than the yellow profiles. Besides sea salt aerosols as a main possible source one cannot exclude dust as a cause for the enhanced backscatter ratio downstream of the mouth of Isfjorden (blue profiles).

A day before, the dust was emitted from the sandy bed of Adventalen and transported along the valley towards the Isfjorden, where the prevailing easterly winds diluted the sand particles (c.fig. 29 (right)). Events like this are more common in autumn when the valleys of Svalbard are free of snow (Stokke et al. [134]). However, the dry conditions during the preceding weeks melted/evaporated the thin snow layer in the valley. As a result, this valley was the only one on Svalbard not covered with snow during the mid of May 2004.

5.9.2 Comparison of the lidar backscatter profiles with output of a local scale dispersion model EULAG

The interpretation of the backscatter ratios which are representative for each region in terms of the origin of particular aerosol loads along the flight path on 19 May 2004 can be done, as discussed in chapters 5.1.4 and 5.1.5, in terms of the output of the large-scale FLEXPART or NOAA HYSPLIT models. However, due to the particular meteorological situation during the Foehn-like event, other local aerosol sources are quite likely as well. Hence, a small-scale dispersion model with an implemented high-resolution orography can prove helpful in an interpretation of the airborne lidar data.

In this section, preliminary results of mesoscale numerical simulations are presented. The numerical experiments are performed with the non-hydrostatic anelastic model EULAG. An up-to-date comprehensive description of the model and its capabilities can be found in Prusa and Smolarkiewicz [74], and Smolarkiewicz and Prusa [75]. The governing equations for momentum, potential temperature and three scalar species are solved by means of finite-difference approximations using a second-order accurate nonoscillatory forward-in-time approach by Smolarkiewicz and Margolin [135]. Dörnbrack et al. [136] employed the various numerical options of EULAG to investigate the reliability and consistency of numerical solutions of different community models for a sheared flow past a bell-shaped mountain.

Specifying the surface distribution of different species, their emission and atmospheric transport was simulated with the model. The initial condition of this simulation were

taken from the upstream ECMWF section at 30°E (see Fig. 19): $U = -8\text{ m s}^{-1}$ and $\Theta(z) = \Theta_0(1 + N^2z/g)$, whereby $\Theta_0 = 264.15\text{ K}$ and the buoyancy frequency N being piecewise constant: $N = 0.0086\text{ s}^{-1}$ for $z < 1000\text{ m}$, $N = 0.0240\text{ s}^{-1}$ for $1000\text{ m} < z < 1500\text{ m}$ emulating the capping inversion, and $N = 0.0160\text{ s}^{-1}$ for $z > 1500\text{ m}$.

Spitsbergen mountains are represented by a digital topography with $2\text{ km} \times 2\text{ km}$ resolution; the whole domain comprises 360×360 equidistant grid points with a resolution of $\Delta x = 2000\text{ m}$ and 51 vertical levels up to a height of 5000 m . The numerical simulations were run for 12 hours with a time step of 6 s .

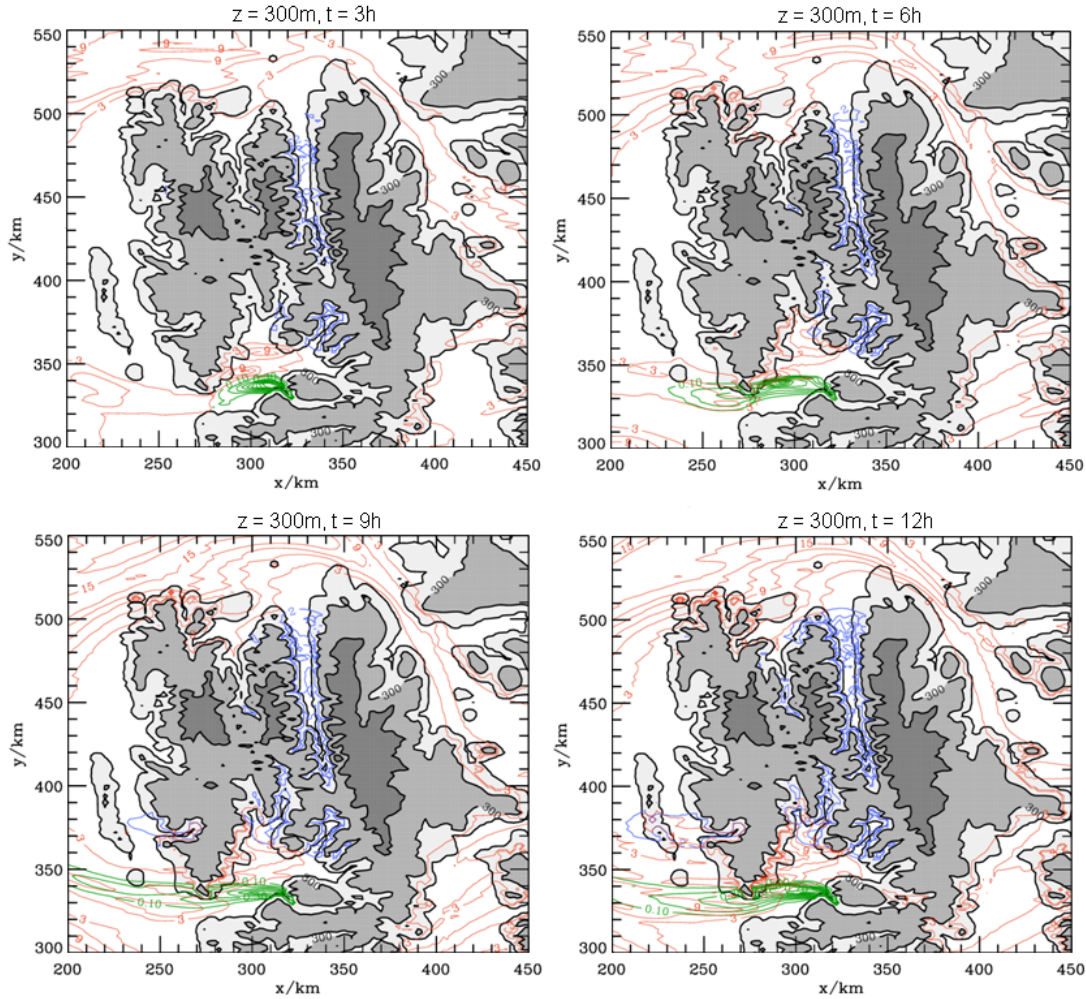


Figure 31: Simulated distribution of scalar species in arbitrary units representing soil dust (green), sea salt (red) and snow (blue) at 300 m altitude after 3, 6, 9, and 12 hours of simulation time. The initial conditions of the simulations are prescribed to represent the meteorological conditions for the AMALi observations on 19 May 2004. The topography is plotted at 10 m , 300 m , and 800 m , respectively. Provided by Dr A. Dörnbrack (DLR-IPA, Germany).

Three different aerosol sources were prescribed at the surface: one species represents sea salt aerosols and hence its source was restricted to the open water area; the second species shall represent snow particles emitted over the whole land surface. A limited release of a third species emulating soil dust was exclusively prescribed in Adventsdalen as observed during the ASTAR 2004 campaign. All the different species get mobilized if the wind velocity at the surface exceed a critical threshold of 1.2 m s^{-1} , afterwards, the species

get vertically mixed by the turbulent flow past the Svalbards mountains. The mobilization phase of the species was modelled according to the formulas presented by Ničković and Dobričić [137]. In this preliminary simulations, the same value of the effective amount of aerosol mobilized at ground was applied for all species.

Figure 31 depicts the temporal evolution of the aerosol distribution every 3 hours by horizontal cross-sections at 300 *m* altitude. Due to the strong corner-wind at the northern tip of Svalbard and the associated enhanced vertical mixing the simulated sea salt aerosol concentration increases with time. This produces a pronounced meridional concentration gradient toward the wake region further south which is less loaded with aerosol. Thus, the simulation results are in qualitative agreement with the lidar observations: the increased aerosol concentration found in the profiles of the yellow category presented in figure 30 was most likely caused by sea salt aerosols. Also the sharp concentration gradient found in the lidar observations is well reproduced by the model simulations. The lowest aerosol content is simulated west and north-west offshore Prins Karls Forland and can be linked to the low backscatter ratios obtained for the pink category profiles in figure 30.

The enhanced aerosol concentration around the mouth of Isefjord was simulated as consisting of a mixture of soil dust and sea salt aerosol. Generally, this is in accord with the observed increase of lidar backscatter in the lowest 300 *m*. However, whether the dust really contributed to the enhanced backscatter must be studied in the future. In the numerical simulations a continuous dust source was prescribed; however, the dust event terminated about 24 hours before the airborne observation. Thus, a realistic simulation of the dust particle emission and transport including sedimentation for a longer period must be done in the future.

It is interesting to note that the numerical model calculated a plume consisting of snow and sea salt without dust in the area south-west offshore Prins Karls Forland (c.fig. 31, simulation time $t = 12 h$). At higher vertical levels, the enhanced aerosol concentration is dominated by snow with maximum values between 1000 *m* and 1500 *m* altitude. Here, one can only speculate if the observed backscatter maximum at about 10:45 UT in figure 22 was generated by drifting ice particles which could not sink due to the large positive vertical velocity in this region (c.fig. 19). Again, a more realistic simulation of the particle properties of snow will give an answer. At the end, the lidar observations will be used to improve the aerosol parametrizations in EULAG in future studies.

5.10 Observations of mixed-phase clouds with alternated AMALi and in-situ instrumentation

The investigations of climate change due to clouds with respect to changes of cloud radiative properties (altitude, area coverage and cloud properties), changes due to indirect effect of aerosols on cloud formation, and changes due to cloud modification on ice pack, are lately recognized important, especially in climatologically pivotal areas such as the Arctic (c.cpt. 1). The information on the properties of arctic clouds, though few campaigns were dedicated to perform clouds measurements in Arctic (c.cpt. 2), is relatively scant, which makes the modelling of the aerosol-cloud-climate interactions especially challenging.

The measurements carried out during ASTAR 2004 campaign in the vicinity of Svalbard Archipelago can well contribute to such collaborative studies since Svalbard is a well-fitting spot to assess the scientific issues mentioned above. The mountainous orography of the archipelago allows for measurements over various distinct terrains. The suitable geographical position with its permanently maintained research stations, as for example Koldewey Station, Rabben Station, Zeppelin Mountain Station, Hornsund Station (c.cpt. 2.1.2), an access to logistic for research aircrafts at the airports in Longyearbyen and Ny-Ålesund (c.cpt. 2.1.1), together with a space observations from polar orbital satellites, for example future CALIPSO or CLOUDSAT makes Svalbard even more interesting

for such studies. Additionally, Svalbard atmosphere is characterised by strong condition transitions from polluted to clean aerosol during Springtime which makes the analysis and interpretation of the measurements much easier as in the mid-latitudes.

5.10.1 New aerosol-cloud investigations aspects during ASTAR 2004

The airborne activities during the ASTAR 2004 campaign were extended, with respect to the ASTAR 2000, by the deployment of an additional research aircraft Polar 2 for remote measurements of the vertical distribution of optical properties of the atmosphere using the AMALi lidar, as well as the in-situ measurements of the optical and microphysical parameters of clouds using instrumentation of the Laboratoire de Météorologie Physique (LaMP).

The contribution by LaMP to the ASTAR campaign focused on the detailed in situ characterisation of microphysical and optical properties of Arctic clouds including particularly the ice phase (mixed-phase clouds). With the observed properties in the future studies of the aerosol-cloud interactions and the cloud-radiation interactions will be performed. Additional focus was on the development of the adequate methods to validate cloud parameters retrieved from remote sensing techniques.

To achieve these objectives LaMP installed an unique combination of scientific instruments onboard of the AWI Polar 2 aircraft allowing to measure cloud particle properties in terms of scattering characteristics, particle morphology and size, and in-cloud partitioning of ice/water content (c.cpt. 5.10.2).

Consequently, a development of an experimental methodology for the description of the cloud properties using combined remote and in-situ measurements, was possible. Under the requirement that both lidar and in-situ instrumentation probe the same cloud a quasi-simultaneous alternated remote observations of clouds vertical and horizontal structures and depolarisation effects due to the presence of ice particles were combined with in-situ microphysics and optical properties of cloud particles.

5.10.2 The in-situ instrumentation

The LaMP instrumental setup onboard the Polar 2 comprises a Polar Nephelometer, a Cloud Particle Imager (CPI) as well as a Nevzorov (from AWI) and standard PMS probes providing information on cloud particle properties in terms of scattering characteristics, particle morphology and size, and in-cloud partitioning of ice/water content.

The Polar Nephelometer, designed and developed at the LaMP (Gayet et al. [138]), measures the scattering phase function of an ensemble of cloud particles (i.e. cloud droplets, ice crystals or a mixture of these) of a size less than $800 \mu m$ with sampling frequency between 1-1000 *ms*. The scattering phase function at a wavelength of $0.8 \mu m$ is measured by optic fibres on scattering angles between $3.49-10.5^\circ$ with the angular resolution of 0.8° and between $15-169^\circ$ by photodiodes with the angular resolution of 3.5° . The optical parameters such as the extinction coefficient and the asymmetry factor are derived from the measured phase function (Jourdan [139]). The cloud classification in terms of particle phase composition (water droplets, mixed-phase, and ice crystals) and particle size distribution is done by a neural network and is validated by probe measurements. Each classified cloud is cross-checked with results of an inversion method using a physical model of light scattering with the average scattering phase function and the retrievals are compared with size composition obtained by direct measurements.

The standard PMS 2D-C probe (Reuter and Bakan [140]) provides the size spectrum of ice crystals and water droplets. The 2-dim shadow images of cloud particles of 25-800 μm size are focused on a 32-elements diode array read out with a maximum repetition frequency up to 5 *MHz*, digitalised with pixel size of 25 μm with temporal resolution of

were taken at a flight altitude of 3 km while heading straight into southern part of Storfjorden (9:00 - 10:20). During these observations the cloud structures were observed over an ice covered northern part of the fiord and the background aerosol profiles were taken in a cloud-free area over open water just outside the fiord. Finally, after a descent into the marine stratocumulus cloud layer, the heading back along the same flight path (10:30 - 11:30) but at altitudes between $1.1 - 1.5\text{ km}$ towards the northern end of Storfjorden while the in-situ observations were performed.

The water stratocumulus cloud top was about -12°C , not unusual in the Arctic (c.cpt. 5.8). Over the Beaufort Sea at altitudes below 2 km and temperatures down to -9°C clouds generally contain purely liquid particles with the lowest concentration of cloud forming particles due to precipitation and nucleation scavenging in the boundary layer (Pinto et al. [133]).

At upper levels ice particles were evidenced to precipitate down to the stratocumulus layer leading to a possible feeder-seeder phenomenon within the water cloud. Therefore, three kinds of clouds with different microphysical and optical properties, i.e. precipitating ice crystals, mixed-phase cloud and water layer cloud with large drops, were evidenced from both measurements.

5.10.4 The remote sampling with AMALi

The AMALi contribution to this experiment was useful in two ways. Firstly, the availability of the real-time display of the quick-look evaluation of the measured atmosphere allowed for an immediate in-flight interpretation of lidar signals at 532 nm and 1064 nm and a depolarisation ratio at 532 nm . Hence, recognition and guidance of in-situ observations into the areas of particular research interest was possible (c.cpt. 3.2.4).

Secondly, after the flight, the calculation of calibrated backscatter profiles at selected times along the flight path and in the regions of low density clouds was possible (c.cpt. 5.10.6) using the iterative airborne lidar inversion scheme considering Klett-Fernald methodology (c.cpt. 4.6 and 5.5).

Figures 33 and 34 represent the AMALi signals and the depolarisation ratio at 532 nm recorded during the flight sequence performed at 3 km (maximum Polar 2 aircraft ceiling).

During the first part of the measurement, between 8:57 - 9:15 precipitating ice particles are clearly evidenced. At some parts of the cloud system in this time interval the ice crystals seem to reach the water cloud below (9:00 - 9:05 and 9:10 - 9:15).

At the very first part of the measurements between 8:58 - 9:02 the double structure in a lower cloud deck with an ice cloud at an altitude of about 1.5 km topped by a water cloud at about 1.75 km was observed. Otherwise, the lower deck cloud contained highly concentrated spherical particles of low depolarisation ratio of 1.4 - 5 %.

In the upper cloud layer the depolarisation ratio increases from 25 - 30 % to 40 - 50 % which clearly reveal the occurrence of irregularly shaped ice crystals. We may expect these ice crystals precipitation down to the water cloud layer at 1.4 km altitude. Then, due to Findeisen-Bergeron process the ice crystals may grow to the detriment of supercooled water droplets as far as most of them may be consumed. Nevertheless, the observations do not confirm this hypothesis since the precipitating down to the ground stratocumulus feature (9:16 - 9:21) rather highlights depolarisation ratio as low as 1.4 % to 5 % typical for only spherical particles and hence for freezing drizzle.

The second part of the measurements between 9:22 - 9:35 UT was taken in a cloud-free atmosphere above a dense liquid cloud of about $150 - 200\text{ m}$ depth extending horizontally over about 65 km at an altitude of about 1.5 km . The laser beam in both lower deck water clouds was rapidly attenuated due to very high concentration of the scattering centres resulting in the multiple scattering. Hence, the lidar signals and depolarisation ratio below these clouds and the sea level cannot be exploited in the further analysis (Weinman [143]).

The signals above these clouds reveal, due to a weaker beam attenuation, distinct cloud structures containing either large non-spherical particles or spherical particles with a lower concentration.

The final part of the measurement between 9:36-9:42 UT was taken in a cloud-free background atmosphere. The noisy character of depolarisation ratio profiles observed in the clear atmosphere areas is due to lower target concentrations than in aerosol-rich atmosphere or in clouds resulting in a weaker backscatter signal at perpendicular 532 nm wavelength.

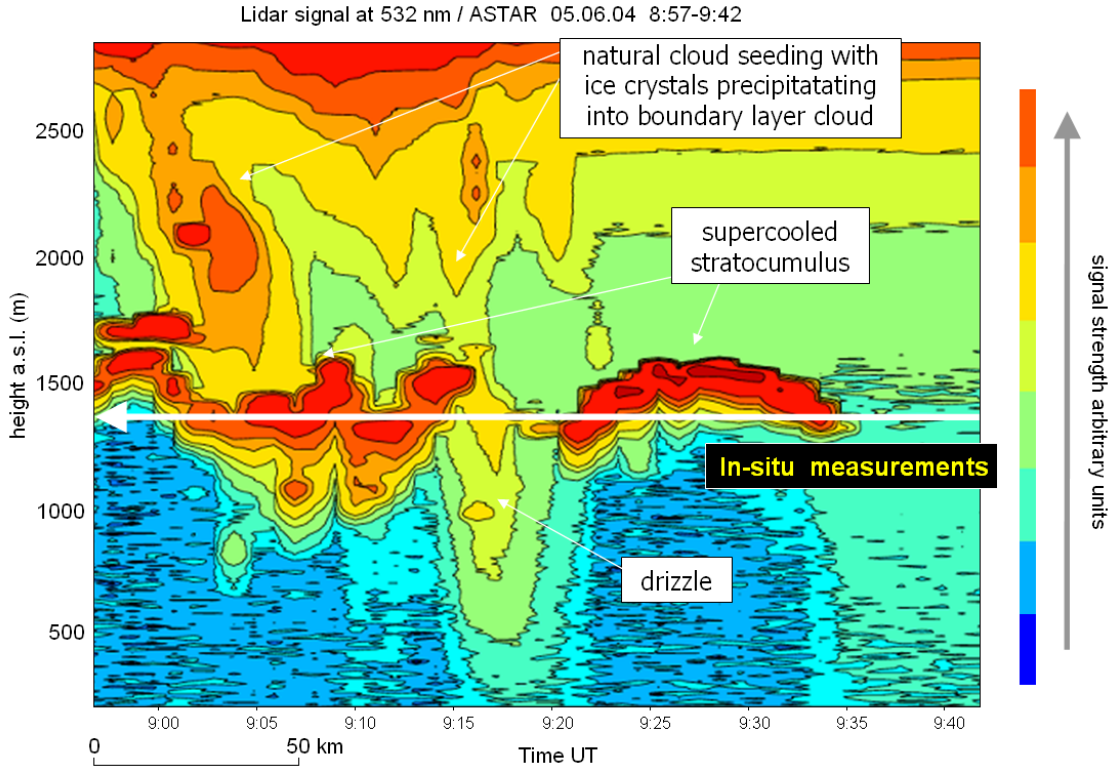


Figure 33: *The vertical cross-section of the attenuated AMALi lidar signal at 532nm for measurements of the mixed-phase clouds between 8:57-9:42 on 5 June 2004 during ASTAR*

Generally, in case of atmospheric regions with very low concentrations of scattering centres backscatter detection at any lidar wavelength is limited. For example, the scattering detection at 1064 nm in very clear atmosphere is usually limited due to the lack of large scattering centres. However, as soon as large particles (dust, large water droplets or ice crystals) appear the detection of these can be done (c.fig. 10).

Similarly, the perpendicular 532 nm detection with the backscatter signals intensities $10^2 - 10^3$ times weaker as for the parallel 532 nm detection, the low densities of the scattering centres in clear arctic atmosphere limit its detection ability, so that the existence of noisy returns in this areas is typical. Hence, the representative mean value of depolarisation ratio of 5.4 % in the clear parts of atmosphere above the water cloud and in cloud-free atmosphere between 9:25 - 9:42 UT was found.

The calculations using the iterative airborne backward Klett inversion algorithm (c.pt. 4.6) allow for the retrieval of the calibrated particle backscatter coefficient along the flight path in areas where the optical depth of the clouds is low enough, i.e. lower than the threshold particle optical depth of 0.065 in a 100 m thick cloud layer. However, for these calculations the lidar ratio has to be assumed.

Usually, for most retrievals of the AMALi observations under clean clear-sky conditions

during ASTAR, the constant lidar ratio of 20-25 *srad* can be assumed (c.cpt. 5.5, error discussion). Theoretically, for the calculations in water clouds the lidar ratio can be obtained from the Mie-theory if, usually difficult, guess of the size of the particles is made. For the ice particles such calculations make hardly sense due to their non-spherical shape, however, if the clouds contain mainly ice crystals an assumption of a lidar ratio between 12-15 *srad* can be made (Ansmann et al. [96]).

Unlike for the usual approach where the lidar ratio is estimated (Carnuth and Reiter [144], Young [145]), this approach allows an application of the iterative Klett algorithm to clouds of low optical densities penetrable with the laser beam without causing the multiple scattering the accurate calculations are done with lidar ratio depending on type of cloud (water/ice) obtained from in-situ observations. The backscatter profiles obtained with such lidar ratios are presented and discussed in chapter 5.10.6).

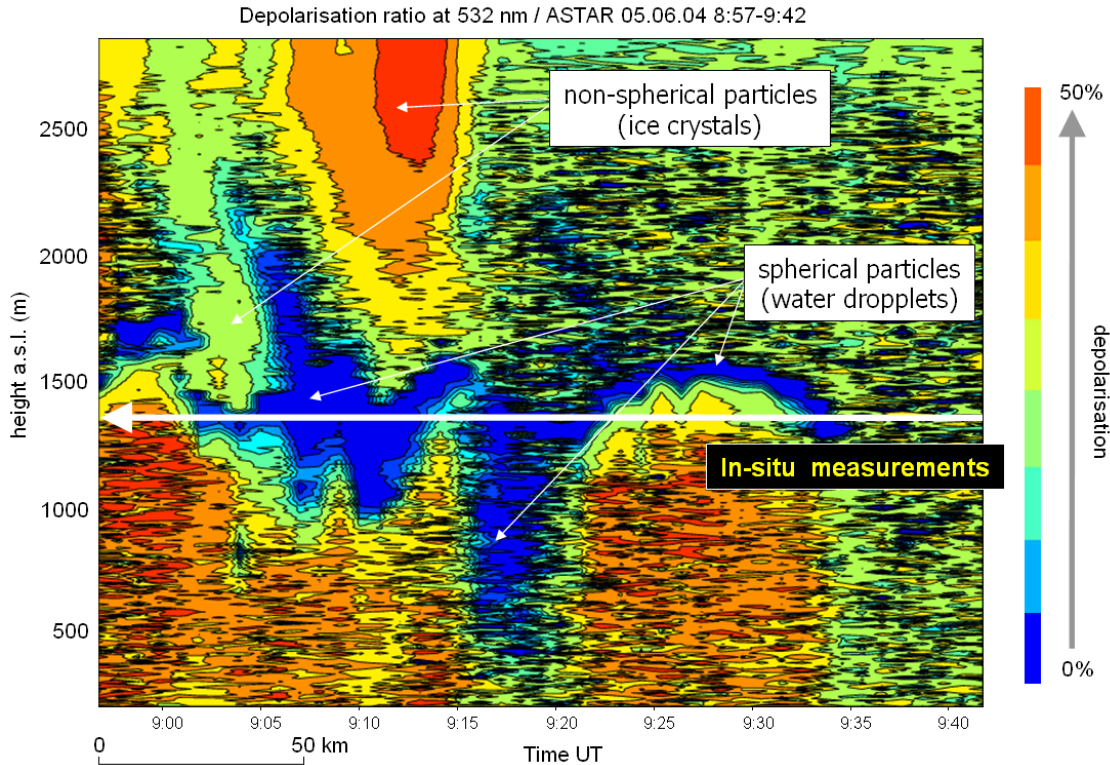


Figure 34: *The vertical cross-section of the depolarisation ratio at 532nm for measurements of the mixed-phase clouds between 8:57-9:42 on 5 June 2004 during ASTAR*

5.10.5 The in-situ sampling with cloud microphysics instrumentation

The in-situ probes provided cloud characteristics in terms of particle size distribution, concentration, ice/liquid water content, morphology, scattering phase function, refractive index and asymmetry factor.

The particle size distributions for water and ice clouds obtained from PMS 2D-C probe and the Polar Nephelometer (after inversion) is depicted on figure 35. Generally, in both types of clouds rather small size cloud droplets with size less than $200 \mu m$ and with no super-large drops were observed. For both types of clouds the concentration of the small size particles with effective diameter around $25 \mu m$ is similar but for the ice cloud a significant fraction of larger particles with effective diameter of around $200 \mu m$ was measured. The particle concentrations of $8 \cdot 10^3 l^{-1}$ with particle extinction of $10 \cdot 10^{-3} m^{-1}$ in water cloud and much lower concentrations of $11 l^{-1}$ and particle extinction of $0.4 \cdot$

$10^{-3}m^{-1}$ in ice cloud were retrieved. In case of a water cloud relatively high concentration of small size droplets are present with absence of large particles. On the contrary, for the ice cloud, the presence of sufficiently large particles causes its 'precipitating' character.

The Nevzorov Probe measured 80 mg m^{-3} liquid water content in the water cloud and 4.3 mg m^{-3} ice water content in ice cloud, respectively.

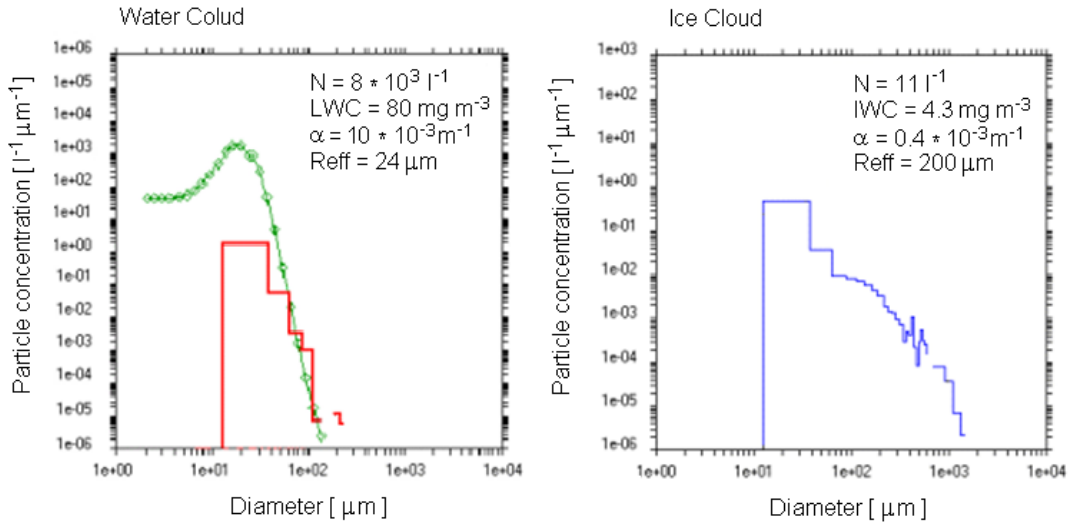


Figure 35: The particle size distributions for water cloud (left) and ice cloud (right) obtained from PMS 2D-C probe (red) and retrieved from the Polar Nephelometer (green) measurements taken on 5 June 2004 during the ASTAR campaign. Provided by Dr. J.-F. Gayet (LaMP, France)

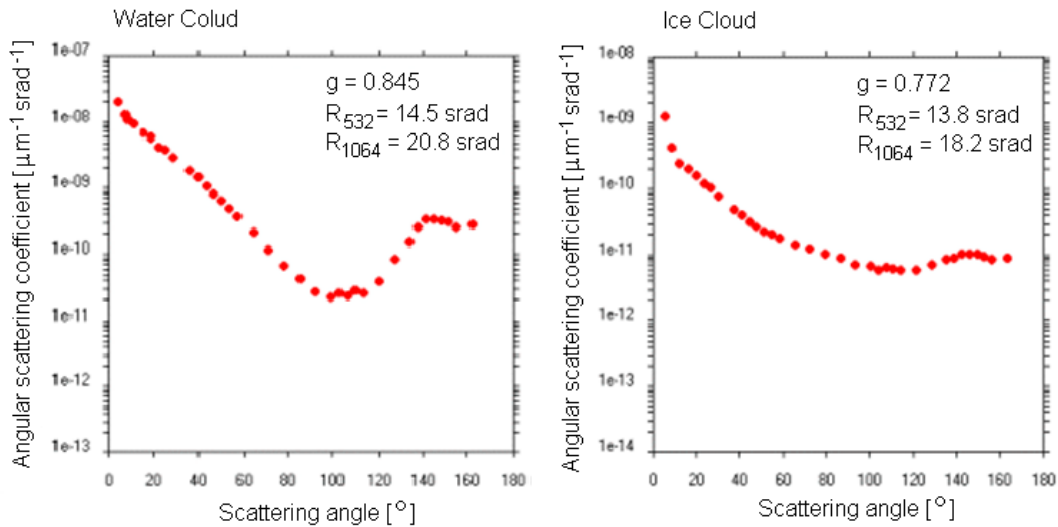


Figure 36: The scattering phase function for water cloud (left) and ice cloud (right) obtained from Polar Nephelometer for measurements taken on 5 June 2004 during the ASTAR campaign. Provided by Dr. J.-F. Gayet (LaMP, France)

The measurements of the scattering phase function for water and precipitating ice crystals obtained with the Polar Nephelometer are shown on figure 36. Characteristic deep minimum due to the spherical particles for the the water cloud is evidenced. For each recognized cloud particle phase composition (water droplets and ice crystals) the optical parameters such as the extinction coefficient, the asymmetry factor and the lidar

ratio were derived from the measured scattering phase function (Jourdan et al. [139]). The lidar ratio of 14.5 srad and, as expected for the ice clouds, a bit lower of 13.8 srad for 532 nm were obtained.

As these results (c.fig. 36) represent mean values obtained during sequences of 2 min for the water cloud and 7 min for the ice cloud, respectively, they are considered statistically reliable due to a very large sampled volume. The natural variability, generally high in any cloud types, is not considered in these results. The statistical errors on microphysical measurements are discussed in details in Gayet et al. [54].

5.10.6 The comparison of the remote and in-situ particle backscatter and extinction retrievals

The figure 37 shows particle backscatter profiles obtained with 2 min temporal resolution corresponding to about 8 km range calculated using the iterative approach with lidar ratios corresponding to 'ice cloud' and 'water cloud' retrieved from the in-situ measurements and 'clear air' lidar ratios assumed to be 25 srad .

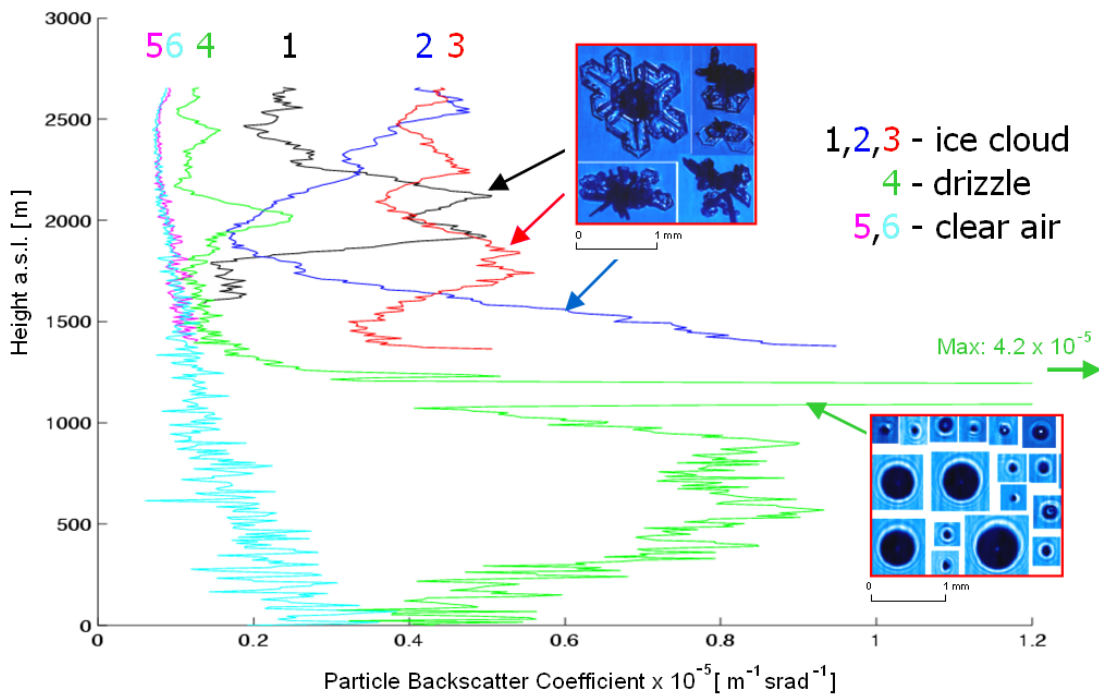


Figure 37: Particle backscatter coefficient retrieved for the preselected regions of the mixed-phase cloud; ice cloud (1-3), drizzle(4), and cloud-free atmosphere (5,6) from the AMALi measurements at 532 nm during the flight on 5 June 2004 at ASTAR campaign. The CPI images of the ice crystals and water droplets attributed to each type of cloud were provided by Dr. J.-F. Gayet (LaMP, France)

The profiles no. 1 - 3 were obtained at 9:00, 9:08 and 9:13 in the area of the precipitating ice crystals. The profile no. 4 was obtained at 9:19 in the drizzle and could be retrieved down to the sea level. The profile no. 5 at 9:27 was obtained in a clear atmosphere above the liquid cloud and, finally, the profile no. 6 at 9:37 in the cloud-free atmosphere was calculated as a reference profile.

The last two profiles were compared for a consistency with the three categories of the different types of the backscatter ratio profiles discussed in chapter 5.9.1. Their shape fits the 'clear air' of the pink category well, though the values of the backscatter ratios

retrieved on 5 June 2004 are slightly higher, with a background backscatter ratio around 1.8 and a maximum of 3 near the sea level.

The lidar particle extinction coefficient of a $0.07 \cdot 10^{-3} m^{-1}$ in the ice cloud area was retrieved for backscatter value of $0.5 \cdot 10^{-5} m^{-1} srad^{-1}$ estimated from particle backscatter coefficient profiles no. 1-3 with corresponding 'ice cloud' lidar ratio of $13.8 srad$.

The lidar particle extinction coefficient of $0.61 \cdot 10^{-3} m^{-1}$ in the drizzle area was retrieved for maximum of the particle backscatter value of $4.2 \cdot 10^{-5} m^{-1} srad^{-1}$ estimated from backscatter profile no. 4 with corresponding 'water cloud' lidar ratio of $14.5 srad$.

The in-situ particle extinction coefficient of a $0.05-0.4 \cdot 10^{-3} m^{-1}$ in the ice cloud and $1-10 \cdot 10^{-3} m^{-1}$ in the drizzle was obtained.

The comparison of particle extinction from remote and direct observations shows similar values in ice clouds and significant differences in drizzle case which can be explained by the time shift between both measurements and by a possible increase of the drizzle formation. The drizzle intensification seems also be reasonable from the analyses of the lidar signals alone. The calculations of particle backscatter profiles in 'cloudy' area is possible only within the range of mentioned threshold values of the particle extinction of less than $0.65 \cdot 10^{-3} m^{-1}$. Hence, the lidar measurements in the intense drizzle sampled by in-situ instrumentation for which the particle extinction coefficient of more than $1 \cdot 10^{-3} m^{-1}$ would not be possible, due to the multiple scattering on these drizzle particles.

Comments on the alternative measurement approach

The airborne remote and in-situ cloud studies comprising the instrumentation on-board of the two aircrafts have been widely used in the 'cloud'-community (Gayet et al. [146]). However, to my knowledge, these are the first observations proving the feasibility of the alternated measurement approach possible if only one aircraft is available.

The combined analysis of remote and in-situ measurements allowed for characterisation of mixed-phase Arctic clouds and for attributing different particle shapes (spherical and non-spherical) to distinct zones of the cloud system. In case of the observations of a feeder-seeder phenomenon three kinds of clouds with different microphysical and optical properties; the precipitating ice crystals, the mixed-phase cloud and the water layer cloud with large drops were found. The identification of vertical and horizontal structures of mixed-phase clouds, the identification of typical signatures of drizzle and ice clouds and the derivation of the typical ice-cloud and liquid-cloud lidar ratios was possible.

The cross-check of the retrieved lidar backscatter and extinction with the in-situ observations proves the feasibility of the alternated probing approach. Though, to improve the methodology more observations coordinated in space and time are necessary.

The lidar measurements of cloud areas and their direct surrounding give an idea on the atmospheric 'dynamics'. It allow to constrain the open questions on whether the surrounding area is entirely clear or contaminated with some cloud particles, as for example in the case of the water drops above boundary cloud deck found between 9:19 and 9:23 in the depolarisation ratios in figure 34. Or whether there is some aerosol associated with the sampled clouds, as for example in the case of the strong aerosol gradients found on the boarder of Foehn-like boundary clouds in figure 22.

Finally, this approach will be continued for the validation of the satellite cloud observations during future ASTAR campaigns, and the results obtained from such alternated measurements should contribute to the modelling of aerosol-cloud-climate interactions.

6 Conclusions and Outlook

The AMALi lidar system constructed and built at the beginning of this project almost three years ago was implemented in many ways for the lower troposphere investigations.

Before the Arctic campaigns took place the system was validated and tested during January-April 2004 while performing ground based investigations of diurnal cycle from the AWI Lidar Laboratory in Potsdam. Additionally, the robust construction and the trouble-free operation of the AMALi lidar allowed for the airborne investigation of the sea-land gradients over the north-western coastline offshore Bremerhaven during the lidar test-campaigns in April 2004 and March 2005.

During the ASTAR 2004 campaign extensive airborne observations of atmospheric events were performed, just to mention few,

- airborne observations of an extend of the local dust plume over Adventdalen,
- investigations of the aerosol gradients between different air masses in North and South offshore the west coast of Spitzbergen,
- investigations of the wave-driven aerosol structures in the same area,
- marine boundary layer observations over the Isfjord,
- combined airborne AMALi, ground based KARL, and ground based remote and in-situ instrumentation at the research stations in vicinity of Ny-Ålesund,
- investigations of the difference in boundary layer aerosol content over
- ice covered sea and the open water sea over the Storfjord by combined remote and in-situ Polar 2 and Polar 4 observations,
- alternated AMALi and in-situ measurements of cloud structures and mixed-phase cloud optical and microphysical characteristics,
- AMALi and in-situ investigations of characteristic falling streaks of a diamond dust,
- investigations of air masses offshore the Sorkapland combined with the in-situ observations at the Polish Station in Hornsund.

Additionally, the ground based AMALi and KARL intercomparison experiment and the ground based AMALi horizontal measurements over Kongsfjord both taken from the AWI's Koldewey Research Station in Ny-Ålesund were performed.

During the SVALEX 2005 campaign the Arctic haze observations aimed to provide a characteristic, horizontal extents and an assessment of the temporal evolution of such event on a small-scale. These were followed by the observations of the polluted air mass spatial and temporal variability, including orographical effects, via parallel and perpendicular measurements with respect to the uniform movement of the polluted air mass.

In the frame of this PhD thesis it is not possible to discuss all of these experiments, hence, the most important results had to be selected to be presented. In the next two chapters comments on each of the issues under concern, as well as an outlook for the future work is summarised.

6.1 Comments on the aerosol and clouds studies described in the frame of this work

Comments on the advantages of the precise knowledge of the lidar constant

For most of the backscatter lidar systems I was acquainted with, the lidar instrumental constant was not known precisely or even not at all, mainly due to the fact that most of these systems used the Klett's evaluation approach for which the lidar instrumental constant is redundant. In this work a way to determine the airborne and ground based lidar instrumental constants precisely was developed and opened a few new aspects for the optical and microphysical parameter retrieval from the backscatter lidar data.

It allowed for the improvement of the Klett's backward approach for the retrieval of the calibrated backscatter ratio profiles from the airborne backscatter lidar data, even if the calibration value is not available or cannot be accurately assumed.

It allowed also for the precise estimation of the initial backscatter calibration value for the application of the Klett's forward approach for the backscatter coefficient retrieval.

Furthermore, it allowed for the successful implementation of the two-stream methodology for the precise calculations of the backscatter coefficient, without the knowledge of the lidar ratio and the calibration value.

Additionally, at least theoretically, it allows for the direct calculation of the aerosol microphysical properties from the range corrected lidar signals, i.e. independently from the extinction and backscatter retrievals.

Comments on the two-stream methodology

The two-stream method is an interesting tool for data evaluation from combined lidar measurements. It proved feasible for the AMALi airborne and KARL ground based data validation and evaluation at a polar site.

In unstable meteorological conditions, it is important that both instruments probe the very same air. However, a simple comparison (division) of both range corrected lidar signals allows for the assessment of the appropriate range for the two-stream application.

The two-stream extinction coefficients were retrieved more precisely than with the Ansmann evaluation approach of the Raman lidar. In the two-stream extinction coefficient profiles, unlike for the Raman retrieval, the main limitation of the obtained profile range is due to the flight altitude of the available airborne/spaceborne craft.

In case that any of the two instruments observes a layer with low or known particle contamination, the lidar constant of this instrument can be precisely determined. Hence, the two-stream backscatter coefficient can be calculated. In the two-stream method, unlike for the Klett inversion, an error of the backscatter calibration causes only bias on the retrieved backscatter profile, i.e. it only shifts the whole profile by a constant value.

Generally, the errors of the two-stream solutions are mainly due to the assumption that both lidars are sampling into exactly the same atmosphere. Hence, in reality the retrieval is possible only if the stability of the measured atmospheric layers lasts a longer time than the time resolution of the airborne lidar sampling.

The application of the two-stream approach for the extinction and the backscatter retrievals from combined ground based and satellite lidar measurements seem feasible as well. Though, the fact that one of the involved instruments in the two-stream method must be air/spaceborne makes this approach quite expensive to be used on everyday basis. However, during future campaigns an ample use of this technique shall be made.

Therefore, especially interesting, is a planned contribution towards validation and analysis of the lidar data obtained from the CALIPSO satellite, which will frequently overfly the polar regions, using the two-stream technique applied to the CALIPSO lidar and the KARL lidar and/or the zenith-aiming AMALi lidar.

Comments on the clean ASTAR contra polluted SVALEX aerosol characteristics

The two-stream method was successfully applied to both clean and polluted (Arctic haze) Arctic air measurements during the clear-sky conditions in the Foehn-gap formed North-West off Svalbard Archipelago. The measurements taken in such interestingly conditions allowed for the comparison of both observations, though they were taken during two campaigns; the ASTAR on 19 May 2004 and the SVALEX on 14 April 2005.

The optical properties of investigated atmosphere on each of these days obtained from the two-stream approach were compared between each other and interpreted in terms of their optical properties (extinction, backscatter, depolarisation, optical depth), microphysical parameters (refractive index, size distribution and particle number concentration) and

meteorological properties (humidity, temperature, origin) providing 'clean' contra 'haze' characteristics.

During the 'clean' day the background values characteristic for the clean Arctic air were retrieved with the particle extinction coefficient varying around $1.5 \cdot 10^{-5} m^{-1}$, the particle backscatter coefficient between $0.3 - 0.7 \cdot 10^{-6} m^{-1} srad^{-1}$ and the lidar ratio of 20 $srad$ with a corresponding complex refractive index $m = 1.4 + 1 \cdot 10^{-4} i$ typical for water particles and a bimodal size distribution dominated with only a few large particles of the effective radius varying between $0.6 - 1.2 \mu m$, very narrow σ of 1.26, and very low particle concentrations between $0.5 - 3 cm^{-3}$. The long-range air mass transport together with the retrieved values of the microphysical and the optical properties suggest that no anthropogenic pollutants were mixed into this air.

A year later, strongly enhanced particle extinction coefficients between $3 - 8 \cdot 10^{-5} m^{-1}$, the particle backscatter coefficients between $0.9 - 2.2 \cdot 10^{-6} m^{-1} srad^{-1}$ and the lidar ratios of about 35 $srad$ were obtained. The corresponding complex refractive index $m = 1.68 + 3 \cdot 10^{-3} i$, typical for anthropogenic aerosol, with noticeably increased value of $Re m$ indicated possible soot contaminations, common for Arctic haze. The size distribution was characterised by a monomodal log-normal distribution with the effective radius of $0.2 \mu m$ with σ of 1.7 and high particle concentrations varying between $50 - 150 cm^{-3}$. The long-range air mass transport indicated the area of Lena Delta and Yenisey Delta as a source of pollution, while the high extinction of this air, its uniform character of the well mixed air within the lower troposphere excludes a local source for the observed aerosol load.

Comments on the evidence of the humid layers in Ny-Ålesund

Most of the profiles retrieved with the two-stream inversion during the ASTAR and the SVALEX campaigns showed an evidence of well pronounced layers characterised by a strongly enhanced particle extinction coefficient and lidar ratio, undiscernible in the backscatter coefficient profiles.

Such a characteristic of the optical parameters usually suggests possible contamination by small amounts of soot particles, which have an effect in enhancement of the extinction coefficient due to its strong absorption of the VIS-radiation. However, an existence of rather a large number of small, supercooled water droplets in the mentioned layer was also credible.

As possible causes for the existence of these layers the following were considered: the contaminations with soot pollutants of local or 'advective' origin; the occurrence of the precondensation conditions as a subvisible clouds; the increase of the relative humidity with the fall of the temperature characteristic for the Foehn-pause formed by the orographic wave retreat; and finally, the cumulation of the particles under a stable, thin inversion layer capping the mountain gap flow layer on the downstream flow into the Kongsfjord valley.

The microphysical parameters justified a contamination by small amounts of soot particles only in one of these layers. The long-range air mass transport showed both the mass origin in the high Arctic or at the lower rather polluted latitudes. The layers occurred during both, the Foehn-like events and the 'normal' clear-sky conditions.

However, all found layers were strongly dependent on the existence of the temperature inversion, evidenced from the radio sounding. Also the microphysical parameters inversion results showed large number ($50 - 300 pcm^{-3}$) of small-sized (around $200 nm$) particles for all layers.

Hence, the local origin of such layers containing a large number of small, supercooled water droplets cumulated just below the inversion layers caused by a meteorological disturbance due to the flow of the air mass over the rough mountains surrounding Kongsfjorden is most credible.

On a methodology point of view it is interesting to note that the observations of such

layers visible only in the extinction and the lidar ratio profiles underline the necessity of a determination of the backscatter and the extinction coefficients independently of each other from lidar measurements. Hence it underlines the necessity of the Karl's Raman approach, the airborne AMALi and KARL two-stream approach and the horizontally-aiming AMALi slope approach for the proper data evaluation.

Comments on the AMALi iterative algorithm

The advantage using an iterative approach proposed in this thesis providing a calibrated quantitative information on the particle backscatter coefficient instead of the qualitative range and background signals provided typically by airborne lidars is clear.

In contrary to most of the airborne evaluation approaches requiring the difficult assessment of the calibration value along the flight in the aerosol rich lower troposphere or additional instrumentation for its measurement, here the method of its precise calculation from the lidar signal alone was discussed and successfully applied to the AMALi data.

The knowledge of the calibration value at any time during the flight allowed for providing the backscatter ratio profiles under the clear-sky conditions, obtained with the assumption of the constant lidar ratios of 20-25 *srad* for clear arctic air and 30-35 *srad* for polluted arctic air. This assumption was found to be not too critical to retrieve accurate backscatter ratio due to a short range of AMALi measurements (2.7 km) under, usually, a very stable Arctic atmosphere and a quasi-uniform air mass transport. For the flights where the air mass transport had non-uniform character and the contamination with pollutants can be expected at a particular altitudes the height dependent lidar ratio was assumed. However, the sensitivity studies for both types of the retrievals showed no significant hindering, i.e. errors less than $2 \cdot 10^{-7} m^{-1} srad^{-1}$ were obtained.

Additionally, the iterative approach was used also to determine the particle backscatter for the observations in the mixed-phase clouds, as long as their low optical densities allowed penetration with the laser beam without causing the multiple scattering. For the calculations in clouds a guess of the lidar ratio is very difficult due to the fact that the partial derivative of the backscatter coefficient over lidar ratio increases with the increase of the backscatter coefficient, i.e. the errors are much larger in clouds. Hence, for these calculations a lidar ratio dependent on type of cloud has to be obtained from the in-situ cloud observations.

Comments on the alternated remote and in-situ cloud measurement methodology

To my knowledge, in this thesis the first observations comprising the airborne remote and in-situ cloud studies proving the feasibility of the alternated approach utilising only one aircraft was presented.

The alternated lidar and in-situ measurements allowed for characterisation of mixed-phase Arctic clouds and for attributing different particle shapes (spherical and non-spherical) to distinct zones of the investigated cloud system.

In the case study of the feeder-seeder phenomenon described in this thesis three kinds of clouds with different microphysical and optical properties were found: the precipitating ice crystals, the mixed-phase cloud and the water cloud with large drops.

The identification of the vertical and horizontal structures of the mixed-phase clouds, the identification of the typical signatures of drizzle and ice clouds, and the derivation of the typical 'ice-cloud' (13.8 *srad*) and the typical 'liquid-cloud' (14.5 *srad*) lidar ratios were possible.

Additionally, the lidar measurements of the cloud areas and the direct surrounding air gave an idea on the 'cloud-dynamics' by assessing whether the surrounding is entirely clear or contaminated with a particular type of aerosol, water or ice crystal particles.

The cross-check of the retrieved lidar backscatter and extinction with the in-situ observations proved the feasibility of the alternated probing approach. The comparison of the

particle extinction coefficient from remote and direct observations showed similar values in ice clouds (lidar: $0.07 \cdot 10^{-3} m^{-1}$, in situ: $0.05 - 0.4 \cdot 10^{-3} m^{-1}$) and significant differences in drizzle case (lidar: $0.61 \cdot 10^{-3} m^{-1}$, in-situ: $1 - 10 \cdot 10^{-3} m^{-1}$). The latter difference can be explained by the time shift of more than 30 min between both measurements and by the drizzle intensification.

In the future more observations coordinated in space and time are necessary for the improvement of the methodology. The approach shall be continued for the validation of the satellite cloud observations (CALYPSO, CLOUDSAT) during the ASTAR 2007 campaign. Finally, the results obtained from such alternated measurements should contribute to the modeling of aerosol-cloud-climate interactions.

Comments on the modelling activities

The knowledge about the origin, transport pathways and vertical structure of aerosol, the physical and chemical properties of the aerosols and clouds including their interaction, as well as their impact on climate in the polar regions, can be greatly improved if a combined effort of complex ground based, airborne and spaceborne observations applied together with regional scale climate modelling tools are implemented.

The collaborative studies on Arctic aerosol-cloud-climate interactions by combining the experimental data on aerosols/clouds properties together with models and the improvement of the required parametrisation of radiation, aerosols and clouds processes are essential.

Each of the ASTAR campaigns provided detailed data sets of optical parameters of Arctic Haze and background conditions which can be used for parameterization of such aerosols in the high resolution regional atmospheric climate model HIRHAM. Some of the required by model sophisticated parameterizations of radiation, aerosol and cloud processes against the provided remote or in-situ observations, as for example the parametrisation of clouds processes with temperature, are still under the development.

For such studies the data obtained during the combined Polar 2 for the AMALi aerosol and cloud measurements and the in-situ clouds measurements together with the Polar 4 for the in-situ measurements of aerosols are highly valuable.

Presented in this thesis characteristics of the optical and microphysical parameters of the 'typical' Arctic Haze (SVALEX 2005) and 'typical' clean arctic conditions (ASTAR 2004) retrieved from combined AMALi and KARL measurements and from the microphysical parameters inversion code shall prove useful for the assessment of the impact of the Arctic haze on climate using the HIRHAM model.

However, existing limitation for the implementation of the lidar information into the atmospheric regional models, including the comparatively small spatial and temporal scale covered by the field campaigns, and the limited information on some parameters, which cannot be directly provided by lidar measurements, as for example particle absorption coefficients, would have to be overcome.

Nevertheless, the new airborne investigations with the AMALi instrument open new data sources for model investigations in two ways.

On one hand, as described in this thesis the obtained along the flight aerosol characteristics can be used for the local scale studies with the small-scale dispersion model EULAG, and will find further application for the parametrisation of the different aerosol types in this model.

On the other hand, data sets representative for the regional scale will become available through the application of the herein proposed methodologies applied to the airborne AMALi lidar and to the satellite borne lidar scheduled for launch this winter (CALIPSO).

6.2 Recommendations for further research

Following is recommended to be performed in the future:

- continuation of the two-stream approach for the airborne data evaluation during the airborne campaigns for the AMALi and the KARL in their current configurations
- validation of the satellite lidar by application of the two-stream approach to the zenith-aiming KARL lidar and the CALIPSO satellite lidar at the satellite overpasses over the Koldewey Station
- validation of the satellite lidar by application of the two-stream approach to the zenith-aiming AMALi lidar measurements onboard Polar 2 flying partly along the flight track of the CALIPSO satellite lidar
- improvement of existing experimental procedure for aerosol-cloud-interaction investigation using the AMALi and the LaMP in-situ instrumentation, also for the validation of the CLOUDSAT data and aerosol-cloud-interaction modelling
- direct implementation of the KARL's lidar signals into microphysical parameters inversion code and feasibility study of this method
- investigation of the potential for implementation of the lidar-obtained vertical and horizontal information on optical and microphysical particle characterisation into the HIRHAM regional climate model
- implementation of a more appropriate 355 nm detection channel instead of the 1064 nm channel for the detection of a small Arctic aerosols
- application of the two-stream approach for the airborne data evaluation at both 532 nm and new 355 nm during the future lidar campaigns for the AMALi and the KARL for aerosol, cloud and Arctic haze investigations
- investigation of the possibility of the Raman channel implementation for the independent particle extinction measurements along the flight
- routine validation of the KARL lidar profiles using AMALi operating in a scanning mode from the Zeppelin Station
- measurements of the atmospheric turbulence using single shot integration times under zenith-aiming ground based configuration
- further investigation of the humid layers over Ny-Ålesund with respect to the meteorological data and the optical and microphysical parameters of these layers

7 Acknowledgements

This work was completed at the Alfred-Wegener-Institute for Polar and Marine Research at the Potsdam Research Unit under the supervision of *Prof. Klaus Dethloff* and *Dr Roland Neuber*. Thank you for your support in affording me the opportunity to learn, built, validate and research with the AMALi lidar, to take part in the ASTAR and SVALEX Arctic airborne field campaigns, and to use the brilliant AWI facilities at the Koldewey Station and at the Lidar Laboratory in Potsdam.

A special thank-you to *Prof. Hanna Pawłowska*, and *Prof. Adolfo Comerón* for your spontaneous and positive decision to referee this thesis.

Countless Thanks to my closest co-worker *Dr Christoph Ritter*. Thank you Chris for taking me seriously as a scientist and for being a remarkable colleague, always ready for a knowledge exchange and discussions on variety of lidar topics. Thank you for joint-developments upon the lidar evaluation schemes and numerous KARL's and microphysics retrievals calculations. At last, for your patience in going over and over this thesis.

Many Thanks are due *Günther Wehrle*, for professional technical expertise in lidar development phase, great help in getting the system through the 'Musterprüfung', and for such a smart, modern and stylish design of the AMALi's heart - respect!

Sincere Thanks to *Dr Andreas Dörnbrack*, for spotting interesting connections between the lidar data and the meteorological events. I trully hope that we will continue the work on AMALi - EULAG simulations. Andy, your valuable suggestions and eminent corrections greatly improved the whole structure of the results chapter of my thesis, thank you!

Much gratitude to *Dr Jean-Francois Gayet and the LaMP-team colleagues*, who assured a great working atmosphere during the alternated flights of the mixed-phase colud observations and awoke my interest in cloud studies. Jean-Francois, thank you for habile and neat corrections of the colud-related chapter of my thesis.

Many Thanks to *Dr Andreas Stohl* for unprompted and energetic way of accepting my wish to perform the FLEXPART simulations. To *Dr Peter van Velthoven* for providing, at a short notice the KNMI trajectories for the SVALEX campaign. To *Dr Andreas Herber* and *Sigrid Debatin* for providing the radiosonde and the sunphotometer data for both campaigns. To *Barbara Heide* for taking voluntary sunphotometer measurements in Longyearbyen during the SVALEX Arctic Haze event. To *Dr hab. Christine Böckmann* and *Andreas Kirsche* for providing the particle microphysical parameter inversion code. To *Dr Andreas Minikin* for providing the preliminary results from the Polar 4 aerosol measurements during the ASTAR campaign.

Special Thanks to *Dr Andreas Herber* for being a marvellous ASTAR co-ordinator and *Dr Thomas Garbrecht* for making the Polar 2 flights a 'gaudi' - it made a difference!

Thanks to all of the ASTAR and the SVALEX co-workers, the staff of the Koldewey Station, the DLR flight operation team and the OPTIMARE team for their infinite support during both campaigns.

I am deeply grateful to *Dr Roland Neuber* and *Dr Marion Maturilli* for all suggestions and corrections of this thesis, to *Holger Deckelmann* for swift help with programming/formatting issues, and to *Heiko Gericke* for recovering my thesis from nonentity!

Much gratitude to *Ms. Christine Litz* for her competent helpfulness and ability to find a right solution with any administrative matter.

My warmest thanks are due to those who encouraged me to embark on the doctoral study especially, to *Dr Matthias Wiegner*, *Dr Mark Tadross* and *Prof. Krzysztof Ernst*. And... to my beloved *Family* and my dearest friends, *Ali Barnes* and *Andy Webb*, for their belief in me to complete it.

Regarding the energy kicks - respect and applause for *Joka*, *Magik*, *Abradab*, *Feel-X* from *Kaliber 44* and *Mr. Maloke*, *Snuggles* and *Pit* from *Puppetmastaz* :)

References

- [1] S. K. Friedlander, *Smoke, Dust, and Haze. Fundamentals of Aerosol Dynamics*, Oxford University Press, 2000.
- [2] J. H. Seinfeld and S. N. Pandis, *Atmospheric chemistry and physics. From air pollution to the climate change*, John Wiley & Sons., New York, 1998.
- [3] K.-N. Liou, *Radiation and Cloud Processes in the Atmosphere. Theory, Observation and Modeling*, Oxford University Press, 1992.
- [4] K. C. Young, *Microphysical Processes in Clouds*, Oxford University Press, 1993.
- [5] P. V. Hobbs ed., *Aerosol-Cloud-Climate Interactions*, Academic Press, 1993.
- [6] K. Y. Kondratyev, *Climatic Effects of Aerosols and Clouds*, Springer Praxis Books, Environmental Sciences, 1999.
- [7] Intergovernmental Panel on Climate Change, *Climate Change 1995. The IPCC Second Assessment Report*, Cambridge University Press, 1996.
- [8] Intergovernmental Panel on Climate Change, *Climate Change 2001. The IPCC Third Assessment Report*. http://www.grida.no/climate/ipcc_tar/wg1/index.htm, Cambridge University Press, 2001.
- [9] Arctic Climate Impact Assessment, *Impacts of a Warming Arctic: The ACIA Scientific Report*. <http://www.acia.uaf.edu/pages/scientific.html>, Cambridge University Press, 2004.
- [10] L. A. Barrie, "Arctic air pollution: an overview of current knowledge," *Atmosph. Environ.* **20**, pp. 643–663, 1986.
- [11] J. Heintzenberg, "Arctic haze: Air pollution in polar regions," *Ambio* **18**, pp. 50–55, 1989.
- [12] G. E. Shaw, "The Arctic haze phenomenon," *Bull. Am. Meteorol. Soc.* **76**, pp. 2403–2412, 1995.
- [13] B. A. Bodhaine and E. G. Dutton, "A long term decrease in Arctic-Haze at Barrow, Alaska," *Geophys. Res. Letters* **20**, pp. 947–950, 1993.
- [14] W. Jaeschke, T. Salkowski, J. P. Dierrsen, J. V. Truembach, U. Krischke, and A. Guenther, "Measurements of trace substances in the arctic troposphere as potential precursors and constituents of arctic haze," *J. Atm. Chem.* **34**, pp. 291–319, 1999.
- [15] R. J. Charlson and T. M. L. Wigley, "Sulphate aerosol and climatic change," *Scientific American* **270**, pp. 48–57, 1994.
- [16] J. E. Penner, S. Y. Zhang, and C. C. Chuang, "Soot and smoke aerosols might not warm the climate," *J. Geo. Res.* **108 D21**, p. 4657 doi:10.1029/2003JD003409, 2003.
- [17] P. Aalto, K. H. abd E. Becker, R. Weber, J. Salm, J. Makela, C. Hoell, C. O'Dowd, H. Karlsson, M. Vakeva, I. K. Koponen, G. Buzorius, and M. S. Kulmala, "Physical characterization of aerosol particles during nucleation events," *Tellus* **53B**, pp. 344–358, 2001.

- [18] R. Treffeisen, A. Herber, J. Ström, M. Shiobara, T. Yamanouchi, S. Yamagata, K. Holmén, M. Kriews, and O. Schrems, “Interpretation of Arctic aerosol properties using cluster analysis applied to observations in the Svalbard area,” *Tellus* **56B**, pp. 457–476, 2004.
- [19] T. Yamanouchi, R. Treffeisen, A. Herber, M. Shiobara, S. Yamagata, K. Hara, K. Sato, M. Yabuki, Y. Tomikawa, A. Rinke, R. Neuber, R. Schumacher, M. Kriews, J. Ström, O. Schrems, and H. Gernandt, “Arctic study of tropospheric aerosol and radiation (ASTAR) 2000: Arctic haze case study,” *Tellus* **57B**, pp. 141–152, 2005.
- [20] K. Dethloff, A. Rinke, R. Lehmann, J. H. Christensen, M. Botzet, and B. Machenhauer, “Regional climate model of the Arctic atmosphere,” *J. Geophys. Res.* **101**, pp. 23401–23422, 1996.
- [21] A. Rinke, K. Dethloff, and M. Fortmann, “Regional climate effects of Arctic haze,” *Geophysical Research Letters* **31**, pp. L16202, doi:10.1029/2004GL020318, 2004.
- [22] J. R. Jensen, *Remote Sensing of the Environment: An Earth Resource Perspective*, Prentice Hall: Upper Saddle River, 2000.
- [23] W. von Hoyningen-Huene, M. Freitag, and J. B. Burrows, “Retrieval of aerosol optical thickness over land surfaces from top-of-atmosphere radiance,” *J. Geophys. Res.* **108**, pp. D9 4260, doi:10.1029/2001JD002018, 2003.
- [24] R. T. H. Collis, “Lidar: A new atmospheric probe,” *Quart. J. Roy. Meteorol. Soc.* **92**, p. 220, 1966.
- [25] J. Bösenberg and V. Matthias, et al. I. Stachlewska (65 aut.), *EARLINET: A European Aerosol Research Lidar Network to establish and aerosol climatology*, vol. Report no. 348, ISSN 0937 1060, Hamburg, 2003.
- [26] R. M. Measures, *Laser Remote Sensing. Fundamentals and Applications*, Wiley & Sons, New York, 1984.
- [27] C. Böckmann, I. Mironowa, D. Müller, L. Schneidenbach, and R. Nessler, “Microphysical aerosol parameters from multiwavelength lidar,” *J. Opt. Soc. Am.* **22/3**, pp. 518–528, 2005.
- [28] J. D. Klett, “Stable analytical inversion solution for processing lidar returns,” *App. Opt.* **20**, pp. 211–220, 1981.
- [29] J. D. Klett, “Lidar inversions with variable backscatter/extinction values,” *App. Opt.* **24**, pp. 1638–1643, 1985.
- [30] A. Ansmann, M. Riebesel, and C. Weitkamp, “Measurements of aerosol extinction profiles with Raman lidar,” *Opt. Lett.* **15**, pp. 746–748, 1990.
- [31] G. J. Kunz, “Bipath Method as a way to measure the spatial backscatter and extinction coefficients with lidar,” *App. Opt.* **26**, pp. 794–795, 1987.
- [32] H. G. Hughes and M. R. Paulson, “Double-ended lidar techniques for aerosol studies,” *App. Opt.* **27**, pp. 2273–2278, 1988.
- [33] I. S. Stachlewska, C. Ritter, and R. Neuber, “Application of new inversion algorithms for airborne lidar measurements of aerosols and clouds in Arctic,” in *Lidar Technologies, Techniques, and Measurements for Atmospheric Remote Sensing*, U. Singh, ed., *The SPIE - The Europe International Symposium on Remote Sensing, Bruges, Belgium*, pp. 5984–33, in print.

- [34] J. Cuesta and P. H. Flamant, “Two-stream lidar inversion algorithm for airborne and satellite validations,” in *Proceedings of 22nd International Laser Radar Conference (ILRC 2004)*, G. Pappalardo and A. Amodeo, eds., *ESA SP-561 1*, pp. 471–474, 2004.
- [35] I. S. Stachlewska and C. Ritter, “Two-stream inversion algorithm applied to elastic lidar measurements in Arctic. Comparison with Ansmann’s approach for Raman lidar retrievals,” *to be submitted in Applied Optics*.
- [36] I. S. Stachlewska, C. Ritter, and R. Neuber, “Nadir-aiming airborne elastic lidar data evaluation by single-profile calibration,” *in preparation*.
- [37] M. Fortmann, “Zum Einfluss troposphärischer Aerosole auf das Klima der Arktis,” *Berichte zur Polar- und Meeresforschung* **486**, 2004.
- [38] R. Treffeisen, A. Rinke, M. Fortmann, K. Dethloff, A. Herber, and T. Yamanouchi, “A case study of the radiative effects of Arctic aerosols in March 2000,” *ELSEVIER Atmospheric Environment* **39**, pp. 899–911, 2005.
- [39] T. S. Bates, B. J. Huebert, J. L. Gras, F. B. Griffiths, and P. A. Durkee, “International Global Atmospheric Chemistry (IGAC) projects first aerosol experiment (ACE 1): Overview,” *J. Geophys. Res.* **103**, pp. 16297–16318, 1998.
- [40] F. Raes, T. Bates, D. Vogelenzang, M. van Liedekerke, and G. Verver, “The second aerosol characterization experiment (ACE-2): General overview and main results,” *Tellus* **52B**, pp. 111–125, 2000.
- [41] A. Ansmann, U. Wandinger, A. Wiedensohler, and U. Leiterer, “Lindenberg Aerosol Characterization Experiment 1998 (LACE 98): Overview,” *J. Geophys. Res.* **107**, p. 8129 doi: 10.1029/2000JD000233, 2002.
- [42] V. Ramanathan et al., “The Indian Ocean Experiment: An integrated analysis of the climate forcing and effects of the great Indo-Asian haze,” *Journal of Geophysical Research* **106**, pp. 28371–28398, 2002.
- [43] A. Minikin, A. Petzold, J. Ström, R. Krejci, M. Seifert, J. Baehr, H. Ziereis, H. Schlager, R. Busen, and U. Schumann, “Interhemispheric differences in the properties of the upper tropospheric background aerosol,” *J. Aerosol Science* **32 s.1**, pp. 1043–1044, 2001.
- [44] J.-F. Gayet, J. Ovarlez, V. Shcherbakov, J. Ström, U. Schumann, A. Minikin, F. Auriol, A. Petzold, , and M. Monier, “Cirrus cloud microphysical and optical properties at southern and northern midlatitudes during the INCA experiment,” *J. Geophys. Res.* **109**, pp. No. D20 , D20206, DOI 10.1029/2004JD004803 (AGU), 2004.
- [45] F. Immler and O. Schrems, “LIDAR measurements of cirrus clouds in the northern and southern hemisphere during INCA (55N, 53S): A comparative study,” *Geophys. Res. Lett.* **29 (16)**, pp. 1809, doi:10.1029/2002GL015077, 2002.
- [46] B. Kärcher and J. Ström, “The roles of dynamical variability and aerosols in cirrus cloud formation,” *Atmos. Chem. Phys.* **3**, pp. 823–838, 2003.
- [47] M. Seifert, J. Ström, R. Krejci, A. Minikin, A. Petzold, J.-F. Gayet, H. Schlager, H. Z. U. Schumann, and J. Ovarlez, “Aerosol-Cirrus interactions: A number based phenomenon at all?,” *Atmos. Chem. Phys.* **4**, pp. 293–305, 2004.

- [48] M. J. McGill, L. Li, W. D. Hart, G. M. Heymsfield, D. L. Hlavka, P. E. Racette, L. Tian, M. A. Vaughan, , and D. M. Winker, “Combined lidar-radar remote sensing: Initial results from CRYSTAL-FACE,” *J. Geophys. Res.* **109**, pp. 1043–1050, 2004.
- [49] E. Raschke, P. Flamant, Y. Fouquart, P. Hignett, H. Isaka, P. R. Jonas, H. Sundqvist, and P. Wendling, “Cloud-radiation studies during the European Cloud and Radiation Experiment (EUCREX),” *Surveys in Geophysics* **19**, pp. 89–138, 1998.
- [50] H. Pawlowska, J.-L. Brenguier, Y. Fouquart, W. Armbruster, S. Bakan, J. Descloitres, J. F. C. Flamant, A. Fouilloux, J.-F. Gayet, S. Gosh, P. Jonas, F. Parol, J. Pelon, and L. Schller, “Microphysical and radiative properties of stratocumulus clouds: the EUCREX mission 206 case study,” *Atmos. Res. Elsevier* **55/11**, pp. 85–102, 2000.
- [51] J.-L. Brenguier, P. Y. Chuang, Y. Fouquart, D. W. Johnson, F. Parol, H. Pawlowska, J. Pelon, L. Schüller, F. Schröder, and J. R. Snider, “An overview of the ACE-2 cloudy column closure experiment,” *Tellus* **52B**, pp. 814–826, 2000.
- [52] S. Menon, J.-L. Brenguier, O. Boucher, P. Davison, A. D. Del Genio, J. Feichter, S. Ghan, S. Guibert, X. Liu, U. Lohmann, H. Pawlowska, J. E. Penner, J. Quaas, D. L. Roberts, L. Schüller, and J. Snider, “Evaluating aerosol/cloud/radiation process parameterizations with single-column models and Second Aerosol Characterization Experiment (ACE-2) CLOUDY COLUMN observations,” *J. Geophys. Res.* **108(D24)**, pp. 4762–4772, 2003.
- [53] T. Hayasaka, N. Kikuchi, and M. Tanaka, “Absorption of solar radiation by stratocumulus clouds: Aircraft measurements and theoretical calculations,” *J. Appl. Meteor.* **34**, pp. 1047–1055, 1995.
- [54] J.-F. Gayet, S. Asano, A. Yamazaki, A. Uchiyama, A. Sinyuk, O. Jourdan, and F. Auriol, “Two case studies of winter continental-type water and mixed-phase stratocumuli over the sea 1. microphysical and optical properties,” *J. Geophys. Res.* **107**, pp. No. D21 , 4569, DOI 10.1029/2001JD001106 (AGU), 2002.
- [55] S. Asano, A. Uchiyama, A. Yamazaki, J.-F. Gayet, and M. Tanizono, “Two case studies of winter continental-type water and mixed-phase stratocumuli over the sea 2. Absorption of solar radiation,” *J. Geophys. Res.* **107**, pp. No. D21 , 4570, DOI 10.1029/2001JD001108 (AGU), 2002.
- [56] R. C. Schnell, “Arctic Haze and the Arctic Gas and Aerosol Sampling Program (AGASP),” *Geophys. Res. Lett.* **11**, pp. 361–364, 1984.
- [57] C. Leck, E. K. Bigg, D. S. Covert, J. Heintzenberg, W. Maenhaut, E. D. Nilsson, and A. Wiedensohler, “Overview of the atmospheric research program during the International Arctic Ocean Expedition 1991 (IAOE-91) and its scientific results,” *Tellus* **48B**, pp. 136–155, 1996.
- [58] T. Zielinski and T. Petelski, “Aerosol physical properties measured in the Arctic during the AREX campaigns 2000-2003,” *Journal of Aerosol Sciences* **II**, pp. 725–726, 2004.
- [59] T. Yamanouchi, M. Wada, M. Shiobara, S. Morimoto, Y. Asuma, and S. Yamagata, “Preliminary report of the Arctic Airborne Measurement Program 2002 (AAMP 02),” *Polar Meteorol. Glaciol.* **17**, pp. 103–115, 2003.

- [60] J. Verlinde, J. Y. Harrington, G. M. McFarquhar, J. Mather, D. Turner, B. Zak, M. Poellot, T. Tooman, A. J. Prenni, G. Kok, E. Eloranta, A. Fridlind, C. Barhmann, K. Sassen, P. J. DeMott, and A. Heymsfield, “Overview of the Mixed-Phase Arctic Cloud Experiment (M-PACE),” in *Eighth Conference on Polar Meteorology and Oceanography, San Diego, CA*, http://ams.confex.com/ams/Annual2005/techprogram/paper_85743.htm, *American Meteorological Society*, 2005.
- [61] A. Aramow, V. T. Yannuzzi, P. Q. Ollson, C. Bahrman, J. Y. Harrington, and J. Verlinde, “Mesoscale modelling during M-PACE,” in *Eighth Conference on Polar Meteorology and Oceanography, San Diego, CA*, http://ams.confex.com/ams/Annual2005/techprogram/paper_87319.htm, *American Meteorological Society*, 2005.
- [62] V. T. Yannuzzi, E. Clothiaux, H. Verlinde, and J. Harrington, “Introduction and important events prior to Mixed-Phase Arctic Cloud Experiment,” in *Fifteenth ARM Science Team Meeting Proceedings, Daytona Beach, Florida*, 2005.
- [63] R. Treffeisen, L. Thomason, A. Herber, J. Ström, S. Burton, and T. Yamanouchi, “Sage II and III aerosol extinction measurements in the Arctic troposphere,” *submitted to J. Geophys. Res.* .
- [64] R. Schumacher, “Messung von optischen Eigenschaften troposphärischer Aerosole in der Arktis,” *Berichte zur Polar- und Meeresforschung* **386**, 2001.
- [65] A. Herber, L. Thomason, H. Gernandt, U. Leiterer, and D. Nagel et al., “Continuous day and night aerosol optical depth observations in the Arctic between 1991 and 1999,” *J. Geophys. Res.* **107 D10**, p. doi:10.1029/2001JD000536, 2002.
- [66] I. S. Stachlewska, G. Wehrle, B. Stein, and R. Neuber, “Airborne Mobile Aerosol Lidar for measurements of arctic aerosols,” in *Proceedings of 22nd International Laser Radar Conference (ILRC 2004)*, G. Pappalardo and A. Amodeo, eds., *ESA SP-561 1*, pp. 87–89, 2004.
- [67] G. Wehrle, I. S. Stachlewska, and R. Neuber, *Dokumentation für die AMALi Lidar Musterprüfung für Einsatz auf dem Polar 2 Do 288 D-CAWI Flugzeug*, Alfred-Wegener-Institute, Library Potsdam, Potsdam, 2003.
- [68] O. Zielinski, “Airborne pollution surveillance using multi-sensor systems,” *Sea Technology* **10**, pp. 28–32, 2003.
- [69] T. Garbrecht, A. Herber, D. Steinhage, and O. Zielinski, “Sensor network for polar research aircraft,” in *Proceedings of the 3rd international symposium on the Arctic research and the 7th Ny-Alesund scientific seminar*, in print.
- [70] I. S. Stachlewska and R. Neuber, *The Airborne Mobile Aerosol Lidar activities during ASTAR 2004 - Internal Report*, Alfred-Wegener-Institute, Library Potsdam, Potsdam, 2004.
- [71] A. A. Kokhanovsky, W. von Hoyningen-Huene, V. V. Rozanov, E. P. Zege, H. Bovensmann, and J. P. Burrows, “A cloud retrieval algorithm for sciamachy,” *Proc. SPIE* **5059**, pp. 116–127, 2003.
- [72] R. R. Draxler and G. D. Rolph, *HYSPLIT (HYbrid Single-Particle Lagrangian Integrated Trajectory HYSPLIT) model*. <http://www.arl.noaa.gov/ready/hysplit4.html>, NOAA Air Resources Laboratory, Silver Spring, MD, 2003.

- [73] A. Stohl, M. Hittenberger, and G. Wotawa, “Validation of the lagrangian particle dispersion model FLEXPART against large scale tracer experiments,” *Atmos. Environ.* **24**, pp. 4245–4264, 1998.
- [74] J. M. Prusa and P. K. Smolarkiewicz, “An all-scale anelastic model for geophysical flows: dynamic grid deformation,” *J. Comp.Phys.* **190**, pp. 601–622, 2003.
- [75] P. K. Smolarkiewicz and J. M. Prusa, “Towards mesh adaptivity for geophysical turbulence: continuous mapping approach,” *Int. J. Numer. Meth. Fluids* **47**, pp. 459–480, 2005.
- [76] K. Dethloff, A. Abegg, A. Rinke, I. Hebestadt, and V. Romanov, “Sensitivity of Arctic simulations to different boundary-layer parametrizations in regional climate model,” *Tellus* **53A**, pp. 1–26, 2001.
- [77] A. Rinke and K. Dethloff, “On the sensitivity of a regional Arctic climate model to initial and boundary conditions,” *Climate Research* **14 (2)**, pp. 101–113, 2000.
- [78] T. Garbrecht, C. Lüpkes, J. Hartmann, and M. Wolff, “Atmospheric drag coefficients over sea ice - validation of a parameterisation concept,” *Tellus A* **54/2**, pp. 205–219, 2002.
- [79] I. S. Stachlewska, *The Airborne Mobile Aerosol Lidar activities during SVALEX 2005 - Internal Report*, Alfred-Wegener-Institute, Library Potsdam, Potsdam, 2005.
- [80] C. Ritter, A. Kirsche, and R. Neuber, “Tropospheric aerosol characterized by a Raman lidar over Spitsbergen,” in *Proceedings of 22nd International Laser Radar Conference (ILRC 2004)*, G. Pappalardo and A. Amodeo, eds., *ESA SP-561 1*, pp. 459–462, 2004.
- [81] C. Ritter and R. Neuber, “Investigation of Arctic haze by tropospheric Raman lidar in Spitsbergen,” *to be submitted in Applied Optics*.
- [82] K. Shimoda, *Introduction to Laser Physics*, Springer-Verlag, Berlin-Heidelberg, 1986.
- [83] G. Wehrle, I. S. Stachlewska, and R. Neuber, *Nachweis zur Augensicherheit des Airborne Mobile Aerosol Lidar AMALi*, Alfred-Wegener-Institute, Library Potsdam, Potsdam, 2003.
- [84] R. K. Luneburg, *Mathematical Theory of Optics*, University of California Press, Berkley and Los Angeles, 1964.
- [85] J. W. Goodman, *Statistical Optics*, Wiley & Sons, New York, 1985.
- [86] D. Müller, U. Wandinger, and A. Ansmann, “Microphysical particle parameters from extinction and backscatter data by inversion with regularization,” *App. Opt.* **38**, pp. 2346–2357, 1999.
- [87] C. Böckmann, “Hybrid regularization method for ill-posed inversion of multiwavelength lidar data in the retrieval of aerosol size distribution,” *App. Opt.* **40**, pp. 1329–1341, 2001.
- [88] I. Veselovskii, A. Kologotin, V. Griazanow, D. Müller, U. Wandinger, and D. White-mann, “Inversion with regularization for the retrieval of tropospheric aerosol parameters from multiwavelength lidar sounding,” *App. Opt.* **38**, pp. 2346–2357, 1999.

- [89] A. E. H. Love, “The scattering of electric waves by dielectric sphere,” *Proc. London Math. Soc.* **30**, pp. 308–321, 1899.
- [90] G. Mie, “Beiträge zur Optik trüber Medien, speziell kolloidaler Metallösungen,” *Ann. Physik* **25**, pp. 377–445, 1908.
- [91] P. Debye, “Der Lichtdruck auf Kugeln von beliebigem Material,” *Ann. Physik* **30**, pp. 57–136, 1909.
- [92] G. Gouesbet and G. Grehan, “Generalized Lorenz-Mie theory for assemblies of spheres and aggregates,” *J. Opt. A: Pure Appl. Opt.* **1**, pp. 706–712 doi:10.1088/1464-4258/1/6/309, 1999.
- [93] M. I. Mishchenko, L. D. Travis, and A. A. Lacis, *Scattering, absorption, and emission of light by small particles*, Cambridge University Press, Cambridge, 2002.
- [94] I. N. Bronsztejn and K. A. Siemiendiajew, *Matematyka. Poradnik Encyklopedyczny*, Panstwowe Wydawnictwo Naukowe, Warszawa, 1990.
- [95] J. Ackermann, “The extinction to backscatter ratio of tropospheric aerosol: A numerical study,” *J. Atmos. Oceanic Technol.* **15**, pp. 1043–1050, 1998.
- [96] A. Ansmann, U. Wandinger, M. Riebesel, C. Weitkamp, and W. Michaelis, “Independent measurements of extinction and backscatter profiles in cirrus clouds by using a combined Raman elastic-backscatter lidar,” *App. Opt.* **26**, pp. 7113–7131, 1992.
- [97] W. Demtröder, *Spektroskopie Laserowa*, Wydawnictwo Naukowe PWN, Warszawa, 1993.
- [98] L. Rayleigh, “On the incidence of aerial and electric waves upon small obstacles in the form of ellipsoids or elliptic cylinders, and on the passage of electric waves through a circular aperture in a conducting screen,” *Phil. Mag.* **44**, pp. 28–52, 1897.
- [99] A. T. Young, “Rayleigh scattering,” *App. Opt.* **20**, pp. 533–535, 1981.
- [100] H. E. Jørgensen, T. Mikkelsen, J. Streicher, H. Herrmann, C. Werner, and E. Lyck, “Lidar calibration experiments,” *App. Phys. B Lasers and Optics* **64/3**, pp. 355–361, 1997.
- [101] D. G. Andrews, *Introduction to Atmospheric Physics*, Cambridge University Press, Cambridge, 2000.
- [102] V. Matthias, C. Böckmann, V. Freudenthaler, G. Pappalardo, and J. Bösenberg, et al. (42 aut.), *Lidar Intercomparisons on algorithm and system level in the frame of EARLINET*, vol. Report no. 337, ISSN 0937 1060, Hamburg, 2002.
- [103] J. E. M. Goldsmith, F. H. Blair, S. E. Bisson, and D. D. Turner, “Turn-key Raman lidar for profiling atmospheric water vapour, clouds, and aerosols,” *App. Opt.* **37**, pp. 4979–4990, 1998.
- [104] K. Rajeev and K. Parameswaran, “Iterative method for the inversion of multiwavelength lidar signals to determine aerosol size distribution,” *App. Opt.* **37 No.21**, p. 4690, 1998.
- [105] F. G. Fernald, “Analysis of atmospheric lidar observations: some comments,” *App. Opt.* **23**, pp. 652–653, 1984.

- [106] D. Kaiser, “Aufbau eines portablen Aerosol-Lidars für Messungen in der unteren Troposphäre,” *Diplomarbeit, Alfred-Wegener-Institute Library, Potsdam*, 2002.
- [107] C. Böckmann, U. Wandinger, A. Ansmann, J. Bösenberg, A. Amiridis, A. Boselli, A. Delaval, F. De Tomasi, M. Frioud, I. V. Grigorov, A. Hågård, M. Horvat, M. Iarlori, L. Komguem, S. Kreipl, G. G. Larchevêque, V. Matthias, A. Papayannis, G. Pappalardo, F. Rocadenbosch, J. A. Rodriguez, J. Schneider, V. Shcherbakov, and M. Wiegner, “Aerosol lidar intercomparison in the framework of the EARLINET project. 2. aerosol backscatter algorithms,” *App. Opt.* **43**, pp. 977–989, 2004.
- [108] W. Weischet, *Einführung in die Allgemeine Klimatologie*, B. G. Teubner, Stuttgart, 1991.
- [109] A. Stohl and D. J. Thomson, “A density correction for lagrangian particle dispersion models,” *Bound.-Layer Met.* **90**, pp. 155–167, 1999.
- [110] P. Seibert and A. Frank, “Source-receptor matrix calculation with a Lagrangian particle dispersion model in backward mode,” *Atmos. Chem. Phys.* **4**, pp. 51–63, 2004.
- [111] A. Stohl, S. Eckhardt, C. Forster, P. James, N. Spichtinger, and P. Seibert, “A replacement for simple back trajectory calculations in the interpretation of atmospheric trace substance measurements,” *Atmos. Environ.* **36**, pp. 4635–4648, 2002.
- [112] P. Skeie and S. Grønås, “Strongly stratified easterly flows across Spitsbergen,” *Tellus* **52A**, pp. 473–486, 2000.
- [113] A. D. Sandvik and B. R. Furevik, “Case study of a coastal jet at Spitsbergen. comparison of SAR and model estimated wind,” *Mon. Wea. Rev.* **130**, pp. 1040–1051, 2002.
- [114] J. D. Doyle and M. A. Shapiro, “Flow response to largescale topography: The greenland tip jet,” *Tellus* **51A**, pp. 728–748, 1999.
- [115] G. W. K. Moore and I. A. Renfrew, “Tip jets and barrier winds: A QuikSCAT climatology of high wind speed events around Greenland,” *J. of Climate* **18**, pp. 3713–3725, 2005.
- [116] Y. Sasano, E. V. Browell, and S. Ismail, “Error caused by using a constant extinction/backscattering ratio in the lidar solution,” *App. Opt.* **24**, pp. 3929–3932, 1985.
- [117] D. N. Whiteman, “Examination of the traditional Raman lidar technique. II. Evaluating the ratios for water vapour and aerosols,” *App. Opt.* **42(15)**, pp. 2571–2592, 2003.
- [118] F. Rocadenbosch, M. Sicard, A. Ansmann, U. Wandinger, V. Matthias, G. Pappalardo, C. Böckmann, A. Comerón, A. Rodríguez, C. Muñoz, and D. G.-V. M. A. López, “Statistical considerations on the raman inversion algorithm: data inversion and error assessment,” in *Laser Radar Technology for Remote Sensing. SPIE-The International Society of Optical Engineering, SPIE - The International Society of Optical Engineering, Bellingham, WA, USA* **14 (2)**, pp. 116–126, 2004.
- [119] D. N. Whiteman, “Examination of the traditional Raman lidar technique. I. Evaluating the temperature dependent lidar equations,” *App. Opt.* **42(15)**, pp. 2593–2608, 2003.

- [120] E. V. Browell, “Airborne Lidar Measurements,” *Review on Laser Eng.* **23**, pp. 133–141, 1995.
- [121] R. Matthey, G. Martucci, V. Mitev, and V. Makarov, “Lidar detection of thin clouds from high altitude aircraft M55 GEOPHYSICA,” in *Proceedings of 22nd International Laser Radar Conference (ILRC 2004)*, G. Pappalardo and A. Amodeo, eds., *ESA SP-561 1*, pp. 95–98, 2004.
- [122] M. Masumoto and N. Takeuchi, “Effects of misestimated far boundary values on two common lidar inversion solutions,” *App. Opt.* **33**, pp. 6451–6456, 1994.
- [123] A. Matsuki, K. Hara, S. Yamagata, T. Yamanouchi, A. Herber, Y. Iwasaka, M. Wada, M. Nagatani, H. Nakata, and D. Trochkin, “Mixing state and spatial distribution of tropospheric aerosols derived from in situ aircraft measurements during Astar 2004,” in *Proceedings of the 3rd international symposium on the Arctic research and the 7th Ny-Alesund scientific seminar*, Book of Abstracts.
- [124] K. Sassen and W. P. Arnott, “Light color in the open air: introduction to the feature issue,” *App. Opt.* **37**, pp. 1425–1426, 1998.
- [125] L. Morawska, S. Thomas, M. Jamriska, and G. Johnson, “The modality of particle size distributions of environmental aerosols,” *Atmos. Environ.* **33**, pp. 4401–4411, 1999.
- [126] G. A. d’Almeida, P. Koepke, and E. P. Shettle, *Atmospheric aerosols: Global climatology and radiative characteristics*, A. Deepak Publishing, Hampton, Virginia, 1991.
- [127] D. S. Covert, A. Wiedensohler, P. Aalto, J. Heinzenberg, P. H. McMurry, and C. Leck, “Aerosol number size distributions from 3 to 500 nm diameter in the arctic marine boundary layer during summer and autumn,” *Tellus*. **48B**, pp. 197–212, 1996.
- [128] J. Cuesta, *private communication*, cuesta@lmd.polytechnique.fr.
- [129] U. Gebhardt, O. Löffel, H. Nies, and S. Knedlik, “Bistatic airborne/satellite hybrid experiment: basic considerations,” in *Proceedings of SPIE. Sensors, Systems, and Next-Generations Satellites IX*, R. Meynart, S. P. Neeck, and H. Shimoda, eds., *The SPIE - The Europe International Symposium of Remote Sensing, Bruges, Belgium* **5978-57**, in print.
- [130] F. Kasten, “Visibility forecast in the phase of precondensation,” *Tellus* **21**, pp. 631–635, 1969.
- [131] W. Carnuth, U. Kempfer, and T. Trickl, “Highlights of the tropospheric lidar studies at IFU within the TOR project,” *Tellus BA* **54 No.2**, pp. 163–185(23), 2002.
- [132] J. G. Mayr, L. Armi, S. Arnold, R. M. Banta, L. S. Darby, D. R. Durran, C. Flamant, S. Gabersek, A. Ghom, R. Mayr, S. Mobbs, L. B. Nance, I. Vergeiner, J. Vergeiner, and C. D. Whiteman, “Gap flow measurements during the Mesoscale Alpine Programme,” *Meteorol. Atmos. Phys.* **86**, pp. 99–119, 2004.
- [133] J. O. Pinto, J. A. Curry, and J. M. Intrieri, “Cloud-aerosol interactions during autumn over Beaufort Sea,” *J. Geo. Res.* **106 D14**, pp. 15077–15097, 2001.
- [134] K. Stokke and other inhabitants of Longyearbyen, Svalbard, *private communication*, stokkari@start.no.

- [135] P. K. Smolarkiewicz and L. G. Margolin, “On forward-in-time differencing for fluids: An Eulerian/semi-Lagrangian nonhydrostatic model for stratified flows,” *Atmos. OceanSpecial* **35**, pp. 127–152, 1997.
- [136] A. Dörnbrack, J. D. Doyle, T. P. Lane, R. D. Sharman, and P. K. Smolarkiewicz, “On physical realizability and uncertainty of numerical solutions,” *Atm. Sci. Lett.* **6**, pp. 118–122, 2005.
- [137] S. Ničković and S. Dobričić, “A model for the long-range transport of desert dust,” *Mon. Wea. Rev.* **124**, pp. 2537–2544, 1996.
- [138] J.-F. Gayet, O. Crépel, J. F. Fournol, and S. Oshchepkov, “A new airborne Polar Nephelometer for the measurements of optical and microphysical cloud properties. Part I : Theoretical design,” *Ann. Geophys.* **15**, pp. 451–459, 1997.
- [139] O. Jourdan, S. Oshchepkov, J.-F. Gayet, V. Shcherbakov, and H. Isaka, “Statistical analysis of cloud light scattering and microphysical properties obtained from airborne measurements,” *J. Geophys. Res.* **108**, pp. No. D5 , DOI 10.1029/2002JD002723 (AGU), 2003.
- [140] A. Reuter and S. Bakan, “Improvements of cloud particle sizing with a 2D-Grey probe,” *J. Atmos. Oceanic Technol.* **15 (5)**, pp. 1196–1203, 1998.
- [141] R. P. Lawson, B. Baker, and C. Schmitt, “An overview of microphysical properties of Arctic clouds observed in May and July 1998 during FIRE ACE,” *J. Geophys. Res.* **106**, pp. 14,989–15,014, 2001.
- [142] A. V. Korolev, J. W. Strapp, G. A. Isaac, and A. N. Nevzorov, “The Nevzorov airborne hot-wire LWC-TWC probe: Principle of operation and performance characteristics,” *J. Atmos. Oceanic Technol.* **15 (6)**, pp. 1495–1510, 1998.
- [143] J. A. Weinman, “Effects of multiple-scattering on lidar pulses reflected by turbid atmosphere,” *J. Atmos. Sci.* **33**, p. 1764, 1976.
- [144] W. Carnuth and R. Reiter, “Cloud extinction profile measurement by lidar using Klett’s inversion method,” *App. Opt.* **25**, p. 2899, 1986.
- [145] S. A. Young, “Analysis of lidar backscatter profiles in optical thin clouds,” *App. Opt.* **30**, p. 7019, 1995.
- [146] J.-F. Gayet, G. Febvre, G. Brogniez, and P. Moerl, “Microphysical characteristics of a marine stratiform cloud obtained from lidar and in situ measurements,” *Atm. Res.* **34**, pp. 99–115, 1994.

Erklärung

Hiermit bestätige ich, dass ich diese Doktorarbeit selbstständig verfasst und keine anderen als die angegebenen Quellen und Hilfsmittel verwendet habe.

Ich versichere, dass diese Arbeit noch nicht an anderer Stelle zur Erlangung eines Doktorgrades eingereicht worden ist.

Potsdam, November 2005

(Iwona Sylwia Stachlewska)